

MODELING AND MEASUREMENT OF THE ROLE OF MACROMOLECULAR
BINDING IN THE ATTACHMENT OF A BROWNIAN PARTICLE TO A
SURFACE

By

HUILIAN MA

A DISSERTATION PRESENTED TO THE GRADUATE SCHOOL
OF THE UNIVERSITY OF FLORIDA IN PARTIAL FULFILLMENT
OF THE REQUIREMENTS FOR THE DEGREE OF
DOCTOR OF PHILOSOPHY

UNIVERSITY OF FLORIDA

2004

Copyright 2004

by

Huilian Ma

To my dearest daughter, Siyu

ACKNOWLEDGEMENTS

First and foremost I would like to thank my advisor, Dr. Richard Dickinson, for his consistent guidance, encouragement and support throughout the whole project. His motivation, dedication and passion towards research as well as his integrity and optimism constantly inspired me all these years!

I also give my thanks to Dr. Anthony Ladd, Dr. Ranganathan Narayanan, Dr. Timothy Anderson, Dr. Oscar Crisalle, Dr. Fan Ren, Dr. Chang-Won Park and Dr. Ben Koopman for their understanding and encouragement for my continuation of my doctoral research here. Without their help, my success in conducting this research work would not have been possible.

I am very grateful for the support of graduated and current research group members. Special thanks go to Dr. Aaron Clapp, Dr. Jonah Klein, Jamaica Prince, Jeffrey Sharp, and Murali Rangarajan for their inspiring and helpful discussions, as well as their patience in teaching me the optical trapping and evanescent wave light scattering techniques. In addition, I have enjoyed so much the joyful laboratory environments created by my fellow students mentioned above as well the most recent lab members including Luzelena Caro, Colin Sturm, and Kimberly Interliggi. This work could not have been progressed smoothly without their encouragement and help.

My stay in this department all these years would be the most eventful time period of my life. And I myself have gone through an unexpected and difficult transition during this time period. I would like to express my heartfelt thanks to

all the faculty, staff, and graduates in this department for their support and help during the difficult times. In particular, many thanks go to Shirley Kelly, Nancy Krell, Peggy-Jo Daugherty, Deborah Sanoval, Nora Infante, Andrea Weatherby, and all other caring staff too numerous to name here.

I gratefully acknowledge the financial assistance and support received from several funding sources, including the National Science Foundation, the NSF Particle Engineering Research Center, the Department of Chemical Engineering at University of Florida, and especially the support of my advisor who has always assured adequate resources in the form of experimental materials and funding.

Finally and most importantly, I am so grateful to my family for their unconditional and unfailing love, care and encouragement throughout my whole life and especially during my overseas study period. I could not find adequate words to express my feelings towards them. I just want to tell my dearest mom and dad, brother and sister that I love them all!

TABLE OF CONTENTS

ACKNOWLEDGEMENTS	iv
ABSTRACT	viii
CHAPTER	
1 INTRODUCTION	1
2 ADHESION OF BIOLOGICAL PARTICLES TO SURFACES	4
2.1 Particle Surface Properties	4
2.2 Interaction Forces Involved During Adhesion and Adhesion Mechanisms	5
2.2.1 Non-Specific Interactions and Attachment Mechanisms	6
2.2.2 Specific Receptor-Ligand Interactions and Attachment Mechanisms	10
2.3 Techniques for Measuring Particle Attachment	17
2.3.1 Adhesion Kinetics	18
2.3.2 Adhesion Strength	19
3 ATTACHMENT KINETICS OF BIOLOGICAL PARTICLES TO SURFACES	21
3.1 Particle-Surface Interaction Energy	22
3.2 Probability Flux	25
3.3 Mean First Passage Time Approach	29
3.3.1 Numerical Method	31
3.3.2 Analytical Approximations	32
3.4 Results and Discussions	42
4 APPLICATION IN ATTACHMENT OF <i>S. AUREUS</i> TO FIBRINOGEN COATED SURFACES	62
4.1 <i>Staphylococcus aureus</i> : Structure and Characteristics	62
4.2 Fibrinogen-Clumping Factor Interaction	63
4.3 Model Parameter Estimations	64
4.4 Model Predictions and Comparison with Experimental Data	74
5 EFFECT OF PARTICLE CURVATURE ON ATTACHMENT	85
5.1 Effect of Curvature on Particle-Surface Interaction Energy	85
5.2 Effect of Curvature on Dynamic Process	88

5.2.1	van Kampen's System Size Expansion	89
5.2.2	Mean First-Passage Time Method	90
5.2.3	Discussions and Suggestions	93
5.2.4	Extension to Other Irregular Surfaces	98
6	EXPERIMENTAL VALIDATIONS USING OPTICAL TRAPPING TECHNIQUE	99
6.1	Materials and Methods	99
6.2	Experimental Setup	101
6.3	Data Analysis and Measurement	103
6.3.1	Evanescence Wave Light Scattering	104
6.3.2	Brownian Motions of a Particle in a Potential Well	104
6.3.3	Calibration of Optical Trap	106
6.3.4	Measurement of Equilibrium and Viscous Forces	107
6.3.5	Experimental Measurements and Discussions	108
7	CONCLUSIONS AND RECOMMENDATIONS FOR FUTURE WORK .	117
APPENDIX		
MATLAB CODES		121
REFERENCES		135
BIOGRAPHICAL SKETCH		141

Abstract of Dissertation Presented to the Graduate School
of the University of Florida in Partial Fulfillment of the
Requirements for the Degree of Doctor of Philosophy

MODELING AND MEASUREMENT OF THE ROLE OF MACROMOLECULAR
BINDING IN THE ATTACHMENT OF A BROWNIAN PARTICLE TO A
SURFACE

By

Huilian Ma

August 2004

Chairman: Richard B. Dickinson
Major Department: Chemical Engineering

Attachment of cells or biological particles to surfaces through the formation of receptor-ligand bonds or other macromolecular bridges is important in many physiological, biomedical, biotechnological, and environmental processes. Along with the well-characterized colloidal forces, the binding kinetics, which is often not taken into account in colloidal theories (*e.g.*, in DLVO theory), also plays a significant role in determining the rate of particle attachment. A probabilistic model is presented here for studying the attachment of a rigid biological particle to a surface when both Brownian motions and binding kinetics are important. From this model, we compute the mean time required for the particle moving from an unattached state (*e.g.*, the second energy minimum) over an energy barrier at a saddle-transition point to an attached state from an energy landscape determined by both colloidal and binding interactions. Based upon the physical and molecular properties of the binding species, the approach advocated here provides an analytical approximation for the mean transition time from the second energy minimum as well as the deposition rate

constant for the general case where neither binding nor particle diffusion is necessarily rate limiting. Application of this model in the adhesion of *Staphylococcus aureus* to fibrinogen-coated surfaces is also described and model prediction results are compared with experimental measurements from our research group. In addition, experiments for a direct testing of model predictions are described using three-dimensional optical trapping along with evanescent wave light scattering techniques to measure the attachment dynamics of streptavidin-coated beads to biotinylated PEG (polyethylene glycol) surfaces.

CHAPTER 1 INTRODUCTION

Attachment of biological particles to surfaces (or other particles) is often mediated by both colloidal forces and receptor-ligand (or other macromolecular) binding interactions. This attachment process is relevant to many fields such as physiological, biomedical, biotechnological, and environmental fields. Examples include recognition and adhesion of cells in the body to extracellular matrix proteins for proper functions [1], infections caused by bacterial adhesion to implanted device surfaces [2], affinity-based separation of cell populations [3], and particle removal by filtration. Along with the well-characterized colloidal forces such as van der Waals attraction, electrical double-layer interactions, and steric stabilization, the discrete bonds formed between a particle and a surface through surface-bound macromolecules also play very significant roles in determining the rate of particle attachment to a surface.

While models have been developed to predict the deposition rate of particles to a surface under the influence of equilibrium colloidal forces, as accounted for in DLVO theory [4, 5, 6, 7], models that account for the role of macromolecular bridging in attachment have been limited. One challenge is that macromolecular bridge formation and dissociation may occur on a time-scale comparable to the time-scale of particle diffusion (which is more important for smaller sized particles, *e.g.*, particle size of micron or submicron here) near a surface, such that the forces involved in bridging may not be assumed to be at equilibrium. Attachment of bacteria to a surface is often considered to be a two-step process [8, 9, 10, 11]: (i) attraction to a weak secondary energy minimum created by non-specific colloidal interactions, followed by

(ii) strong adhesion by the formation of specific binding interaction between cell-surface macromolecules (“adhesins”) and complimentary ligands on the substratum to form an “irreversible” attachment (*i.e.*, the probability of spontaneous detachment is negligibly small. In this view, the affinity and kinetics of the binding interactions as well as the lengths of binding molecules are important parameters in determining whether or not attachment will be achieved during the time the bacterium is reversibly associated with the surface. For example, Hartford *et al.* [12] showed that attachment of *Staphylococcus aureus* (*S. aureus*) to fibrinogen-coated surfaces depended strongly on the length of a putative stalk region on an adhesin expressed on bacterial surface. Mascari and Ross [13] observed that the attachment rate of *S. aureus* to collagen depended upon the density of bacterial adhesins, which suggested that the deposition was rate-limited by the formation of specific bonds with collagen. They also showed that about 10pN shear force on a bacterium was sufficient to begin to diminish the attachment rate. Since 10 pN is typically required to accelerate dissociation of a single receptor-ligand bond, it can be surmised that attachment required formation of only a few adhesin-collagen bonds while the bacterium was close enough to the surface for bonds to form. Thus, predictions of deposition rate by diffusion over an energy barrier [14] only cannot account for such observations.

The goal of the work described in this thesis is to have a fundamental understanding of the attachment of biological particles to surfaces when both particle diffusion and macromolecular binding kinetics are important. This understanding may aid in enhancing or reducing particle attachment according to actual practical applications by modifying particle surface or corresponding substrate properties, for example, in designing infection-resistant biomaterials to prevent bacterial infection of implanted intravascular and biomedical devices.

This dissertation describes the development of a dynamic model for studying the attachment of biological particles to a surface that accounts for both colloidal

forces and macromolecular binding interactions. In addition, application of this model in the adhesion of bacterium *S. aureus* to fibrinogen-coated surfaces and the direct experimental testing of this model using three-dimensional optical trapping techniques are also described.

This dissertation is organized as follows. Chapter 2 gives an overview on the current stage of knowledge with respect to biological properties and physics underlying the adhesion mechanisms of particles to a surface and the common measurement techniques used to study adhesion. In Chapter 3, a dynamic model is developed to predict the mean transition time for a particle from the unattached state (e.g., the secondary energy minimum) to the attached state as well as the deposition rate constant when both Brownian motions and macromolecular binding interactions are important. The application of the model developed in Chapter 3 in the adhesion of *S. aureus* to fibrinogen-coated surfaces is described in Chapter 4 and results obtained from the model are compared with experimental measurements by other research group members. Chapter 5 attempts to examine how the surface curvature of particles affect attachment rate. In Chapter 6, experiments to evaluate the model predictions in Chapter 3 are described using three-dimensional optical trapping along with evanescent wave light scattering techniques to measure the attachment dynamics of streptavidin-coated beads to biotinylated PEG (polyethylene glycol) surfaces. Chapter 7 concludes this thesis with the major accomplishments and results and also gives recommendations for future work.

CHAPTER 2 ADHESION OF BIOLOGICAL PARTICLES TO SURFACES

Adhesion of biological particles to a surface is often mediated by receptor-ligand or other macromolecular binding interactions. For example, the ability of cells to recognize and adhere specifically to other cells or to extracellular tissue matrix proteins is critical to many physiological processes. Cells flowing through the body's circulatory systems (blood and lymph) adhere to vessel endothelia in particular organs for proper functions [1]. Also, cell-surface adhesion can be exploited for biotechnological purposes, such as affinity-based separation of cell populations [3]. In addition, microbial adhesion to surfaces plays a very important role in a variety of fields covering different aspects of nature and human life, such as water treatment, food industry, marine science, and most importantly biomedical fields. For instance, adhesion of bacteria to human tissue surfaces or implanted biomedical device surfaces is an initial step in the pathogenesis of infection [2]. Therefore, having a better understanding of adhesion mechanism helps to either enhance or reduce adhesion according to practical needs by modifying molecular structures and properties of particle surfaces and corresponding substrata.

2.1 Particle Surface Properties

The basic surface structure for all living cells shows great similarities across all species and genera. This consensus structure, termed the fluid mosaic model, consists of a continuum bilayer membrane of lipids punctuated by proteins of varying penetration. The basic building blocks of all membranes are the phospholipids. Most of the lipids of the membrane show free lateral motions if they are not associated

with proteins. Proteins embedded in the lipid matrix carry out most of the specific processes associated with the membrane.

Gram positive prokaryotes have a relatively thick cell wall, consisting mainly of peptidoglycan layer (*i.e.*, a rigid polysaccharide layer cross-linked with lipoproteins and other polysaccharides) that surrounds the membrane. In gram negative bacteria, there is a second bilayer outside the peptidoglycan. Thus the long range interactions between bacterial cell surfaces and substrates or other bacteria may be also influenced by these cell wall effects. The cell wall is absent in animal cells, but a complex negatively charged layer, known as glycocalyx composed of polysaccharides often attached to the lipids and proteins of the membrane, extends up to about 150 nm away from the cell surface. Likewise, these high molecular weight molecules contained in glycocalyx are also important for cellular adhesion, and can induce great morphological changes in cell shape and motility.

The adhesion of cells (*e.g.*, bacteria) to a surface is a result of an interplay between specific interaction (which involves in the stereochemical participation of cell surface receptors and the complementary binding molecules such as ligands) and non-specific interactions (which are usually defined as the types of interactions that do not involve cell surface binding molecules), as discussed below. Therefore, from a physico-chemical viewpoint, the real functional surface of biological particles such as cells is a tangled mat of negatively charged polysaccharides and proteins dotted with specific recognition sites.

2.2 Interaction Forces Involved During Adhesion and Adhesion Mechanisms

To better understand the adhesion mechanism of biological particles to surfaces, it is essential that the interaction forces involved throughout the entire adhesion process can be identified and characterized.

The transition of a particle from a fluid suspension (“free” or “unattached” state hereinafter) to attachment usually involves the following steps, as illustrated in

Figure 2.1(a). The particle first must arrive at the vicinity of the surface via fluid convection or motility (for cells). Then it must cross the diffusion boundary layer near the surface through Brownian motions to reach the region where the long range interaction forces between the particle and the surface become significant enough to overcome the driving forces resulted from Brownian motions (~ 1 pN). Finally, the particle must be able to resist any dislodging forces (for example, fluid shear) and to stay attached to the surface through the formation of receptor-ligand bonds. Since the processes of transport and attachment take place in series, the slower of these steps limits the overall deposition rate of cells to a surface. Below, we shall discuss the major forces involved during the attachment process according to the classification of these forces into non-specific and specific interactions and then describe the adhesion mechanism within each category.

2.2.1 Non-Specific Interactions and Attachment Mechanisms

Non-specific interactions are defined as interactions between a particle and a surface (or another particle) that do not involve surface-bound macromolecules, namely, that are not biochemically specific but do act to increase or decrease the overall strength of the interactions. The common operating non-specific interactions include DLVO (*i.e.*, attractive van der Waals and repulsive electrostatic interactions), hydration, steric, and hydrophobic interactions. Among these, three major ones are important for the typical biological adhesion processes: electrostatic forces, steric stabilization, and van der Waals or electrodynamic forces. All of them are present in the adhesion process, but each is dominant at a different particle-substrate separation distance. The relationship between these forces and separation distance has been characterized in many papers [15, 16, 17].

As mentioned earlier, the surface of biological particles such as cells consists of a lipid bilayer containing ligands and/or other embedded surface-expressed macromolecules as well as glycocalyx that usually is negatively charged due to the present

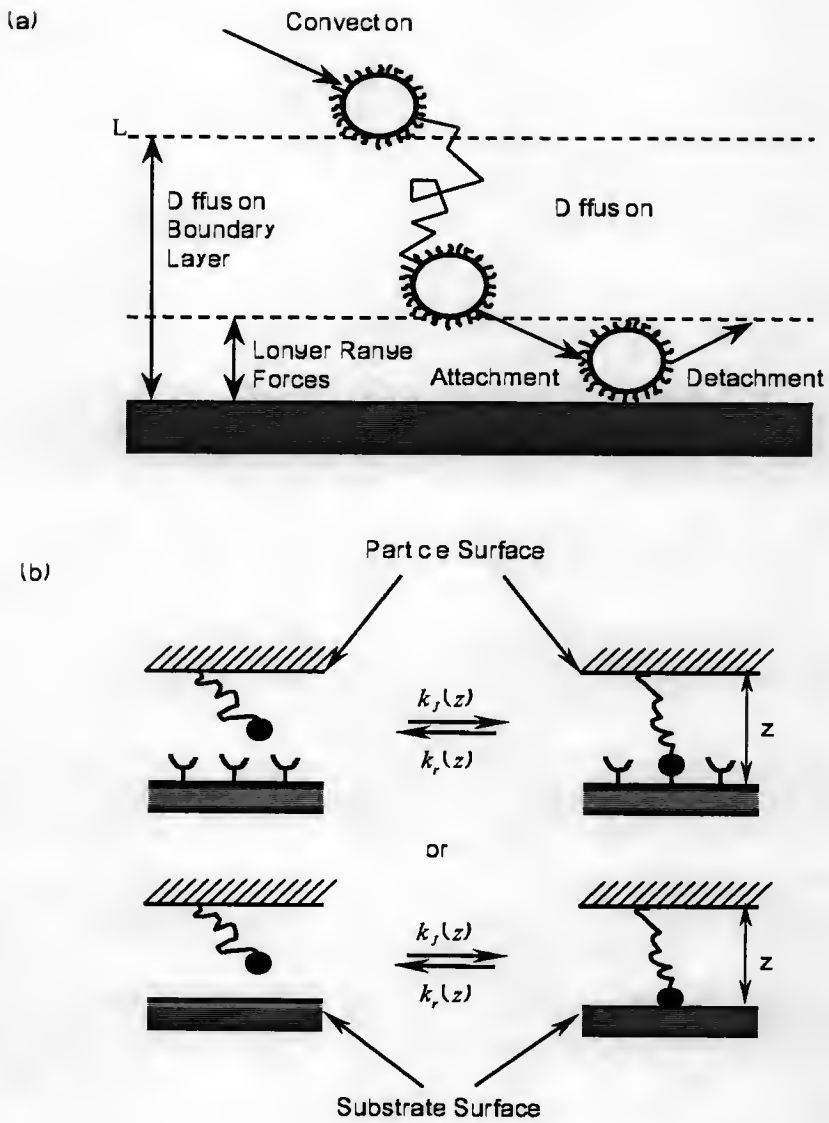


Figure 2.1: Critical steps involved in particle attachment and illustration of specific binding interactions. (a) Critical steps in particle attachment: convective transport, diffusion, attachment and resistance to detachment. Long-range interaction forces govern the rate of attachment and short-range interaction forces govern the strength of attachment that resists detachment from the surface [18]. (b) Illustration of the reversible processes of formation and dissociation for a single bond which could be a receptor-ligand pair or a macromolecule bound to a bare surface. $k_f(z)$ is the forward binding rate constant and $k_r(z)$ is the reverse dissociation rate constant. Here a uniform interaction region at the interface between the particle and the substrate is assumed. Also we assume that the bonds formed do not affect the availability of binding property and the activity of the binding sites on the substrate surface.

sialic acid residues. For cell-cell or cell-substratum (if negatively charged too) adhesion, the bringing together of two negatively charged surfaces leads to an overall repulsive electrostatic force between them as a result of the overlapping electric double layers surrounding the cell or the substrate. The glycocalyx consists of polymers in a hydrated environment. As this polymer coat approaches to a surface, this layer is compressed and some of the water molecules are pushed out. A repulsive force termed steric stabilization results because of the steric compression of the polymer chains and also because of the osmotic tendency of water molecules to return. The other non-specific forces, van der Waals forces, ubiquitous and usually attractive, arise from the charge interaction of polarizable molecules, including molecules with no net charges, on the cell surface as well as in the solvent.

Using a simplified physical model for cell membranes and mathematical descriptions of these three non-specific forces, Bongrand and Bell [16] calculated the magnitudes of these forces for the case of cell-cell adhesion. Their results are shown in Figure 2.2, where the interaction potential per unit area between the two like cells and also the force per unit area required to separate these two cells are plotted as a function of separation distance. Here, the interaction energy is obtained by integrating the force from a given distance to infinity. At small separation distances, repulsive potentials dominate the overall cell-cell interactions; as the separation distance increases, repulsive potentials fall off (at distance on the order of 200 Å) and the attractive van der Waals forces act to bring cell surfaces into proximity and thus to increase the likelihood of cellular adhesion.

For smaller (micron or submicron) sized particles, the effects of Brownian motions on them are more significant. So, the first predictive models for particle attachment were drawn from colloidal physics. The most cited theory used to quantify the non-specific long-range interactions between bacterial cells and surfaces is

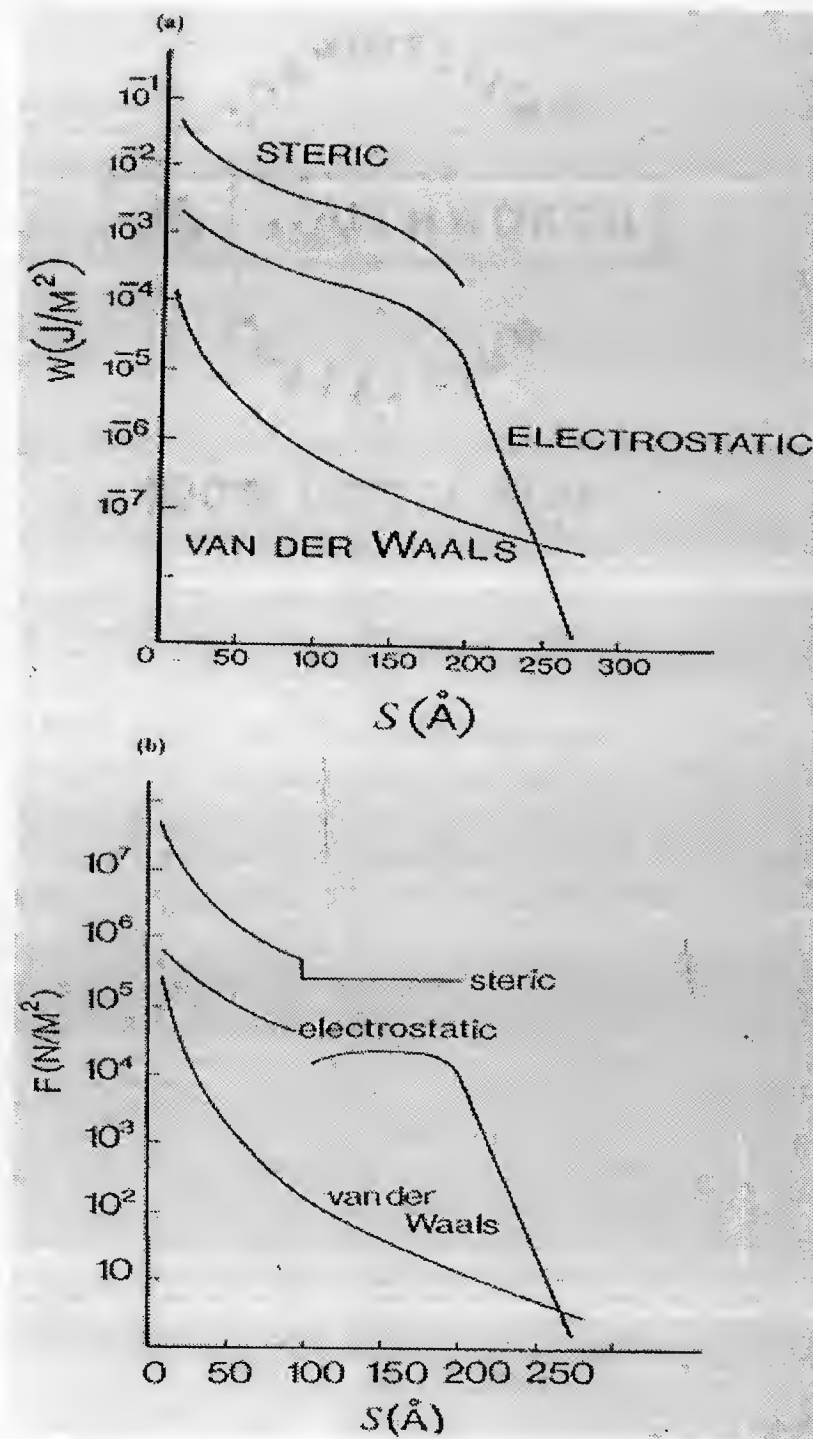


Figure 2.2: Three major non-specific forces present in cellular adhesion: electrostatic, steric and van der Waals forces. (a) Each interaction potential is plotted as a function of separation distance; (b) Interaction forces between two cells are plotted versus separation distance. Absolute values are shown in both plots. Source: [16]

DLVO (Derjaguin-Landau-Verwey-Overbeek, [4, 5]) theory [11]. Classic DLVO theory accounts for electrostatic repulsion and van der Waals attraction; later on, other factors such as hydrophobic interactions [7] and polymer-induced steric forces [19] have been introduced to the DLVO theory, which formed the so-called extended DLVO theories. Since it predicts a potential energy profile as a continuous function of separation distance by using various system-specific parameters (*e.g.*, the Hamaker constant, surface charge, solution ionic strength, particle size, *etc.*), the DLVO theory does provide a conceptual framework for interpreting particle attachment; that is, a particle must pass over an energy barrier to become attached to a surface, which shall be employed in the derivation of our model in Chapter 3. However, the DLVO theory fails to fully elucidate the mechanism of particle attachment because the specific receptor-ligand binding interactions are not taken into account at all, even though to some extent it is able to successfully explain non-specific mechanism of microbial adhesion.

2.2.2 Specific Receptor-Ligand Interactions and Attachment Mechanisms

Despite the repulsive constraints described above, specific receptor-ligand interactions, as illustrated in Figure 2.1(b), are the favored explanation for the ability of microbes or biological particles to adhere and recognize the corresponding binding components on other particles or surfaces. In what follows, the main characteristics of the receptor-ligand interactions are discussed and some specific adhesion mechanisms are described afterwards.

Characteristics of Specific Interactions

Specific Forces and Reaction Kinetics. The primary physical forces that are involved in receptor-ligand binding are Lifshitz-van der Waals (LW), electrostatic (EL) and Lewis acid-base (AB) (or, electron acceptor-electron donor) interactions

[17]. These are the same forces that give rise to the non-specific interactions described earlier. Although the physical nature of the forces underlying specific interactions is the same as that of non-specific interactions, receptor-ligand binding is often described in terms of chemical reaction kinetics. The rationale for applying this framework comes from physical characteristics of these weak, non-covalent specific binding interactions. First, the interaction range between receptor and ligand binding domains is very short (~ 1 nm) compared to non-specific interactions. Also, receptors and corresponding binding molecules must be properly oriented toward each other for bonding to occur. As a result, the interactions between them are often described by "lock-to-key" type, in other words, only when the receptor and ligand molecules are in proper stereochemical orientations, will binding reaction occur; otherwise, these two molecules behave like the other one does not exist even at very close distance. Therefore, unlike the non-specific interactions, which have been successfully described by force-distance relationship, for specific interactions, however, it is difficult to relate the separation distance between two particle surfaces to the binding molecular sites. The advantage of using the kinetic description is that the information contained in the force-distance relationship is lumped into the kinetic rate and equilibrium constants.

Two-Dimensional Kinetics. Contrasted to three dimensional (3-D) motions of free molecules in solutions, the surface-bound receptors and complementary ligands are limited to two dimensional (2-D) movements. Table 2.1 shows the typical units for each species as well as for the binding rate constants. In the current work, we shall deal primarily with 2-D/2-D case. To determine values for the affinity and kinetic rate constants, it is essential to know (or measure) the number of bonds formed between the two approaching surfaces. However, direct experimental measurements of receptor-ligand bonds have not yet been possible when two reacting molecules are linked to surfaces. A more common approach is to first measure the

3-D affinity (determined when both receptor and ligand molecules diffuse freely in free solutions) and then convert it to a 2-D affinity using a parameter, which, in general, is on the order of the size of the receptor-ligand complex molecules [20, 21]. A method to convert 3-D binding kinetic rate affinity constants to 2-D ones is also developed in Chapter 4. Recently, measurements of 2-D affinity [22, 23] and binding rate constants [24] have begun and solid biophysical measurements are required to fully elucidate this relationship.

Coupling of Kinetics and Mechanics. Since both receptors and ligands (or other binding macromolecules and the complementary binding sites) are anchored at particle surfaces, besides thermal agitations, the crosslinks formed between them are usually subjected to a dislodging force, such as fluid shear, that tends to alter binding kinetic rates, and thus alter the strength and the lifetime of these bonds as well. There are several models to account for the effect of external forces on binding kinetics. The most commonly used one was developed by Bell in 1978 [20]. Drawing from the kinetic theory of the strength of solids, it assumes that although the forward rate constant should not be affected by the applied force, the reverse rate constant, and thus the affinity, will vary exponentially with force f

$$k_r(f) = k_{r0} \exp\left(\frac{af}{N_b k_B T}\right), \quad (2.1)$$

Table 2.1: Units for measurement of receptor-ligand interactions

Dimensionality R/L	Receptor (R)	Ligand (L)	Complex (C)	Association rate (k_{f0})	Dissociation rate (k_{r0})	Affinity (K_{eq0})
3D/3D	$\text{mol}^{-1}\text{L} (\text{M})$	M	M	$\text{M}^{-1}\text{s}^{-1}$	s^{-1}	M^{-1}
2D/3D	μm^{-2}	M	μm^{-2}	$\text{M}^{-1}\text{s}^{-1}$	s^{-1}	M^{-1}
2D/2D	μm^{-2}	μm^{-2}	μm^{-2}	$\mu\text{m}^{-2}\text{s}^{-1}$	s^{-1}	μm^2

where k_{r0} (in s^{-1}) is the reverse rate constant in the absence of force, a is a length parameter defined as the bond interaction distance, f is the applied force and N_b is the number of receptor-ligand bonds formed. An alternative approach assumes the receptor-ligand bond behaves like a Hookean spring, as proposed by Dembo and coworkers [25, 26]. In this case, affinity will decrease as a receptor-ligand bond moves away from its equilibrium position according to a Boltzmann distribution shown below

$$K_{eq}(z) = K_{eq0} \exp\left(-\frac{\gamma_b(z - z_0)^2}{2k_B T}\right), \quad (2.2)$$

where γ_b is the mechanical spring constant of the bond and z_0 is the unstressed bond length. From the strain-dependence of the transition state theory between bound state and free state, Dembo *et al.* suggested two exponential laws for $k_r(z)$ and $k_f(z)$, but required their ratio to satisfy the above equation with the knowledge of $K_{eq}(z) = k_f(z) / k_r(z)$. Evans and Ritchie [27] placed the relationship between reverse rate constant and bond force on a more rigorous foundation by deriving it from Kramers' theory [28] for the escape of thermally agitated particles from a potential well tilted by an applied force. Under greatly simplified conditions, their results were found to be a combination of power law and exponential model between reverse rate and applied force, and also k_f is assumed to be constant.

Stochastic Characteristics and Probabilistic Kinetic Framework. Over the past decade, it has been recognized that cellular adhesions are often mediated via a surprisingly small number of receptor-ligand bonds. As a result of this low bond number, small-scale adhesion becomes stochastic in nature and many experimental observations have shown this property. For example, in the flow chamber assay, a moving cell interacting with a stationary surface is observed to undergo stop-and-go types of motions with highly fluctuated velocities [29, 30]. Even in the well-controlled micropipette experiment, when a pair of cells (or engineered biological particles) is brought together in any single test, adhesion events still occur randomly, despite all

the other experimental conditions are kept identical [23, 24]. In addition, any single measurement for adhesion lifetime or detachment force also lacks deterministic value. Regardless of this randomness, the occurrence of bond formation or dissociation events has a certain likelihood. Although any single measurement is of little use, a collection of many measurements can reveal a well-defined, although still highly scattered, distribution, which corresponds to the probability density for the occurrence of any particular value. Such randomness is not caused by measurement errors but is a manifestation of the stochastic nature inherent in the chemistry of receptor-ligand binding, which becomes more significant when the number of bonds per cell is small. This calls for a probabilistic description of the receptor-ligand binding kinetics.

Although the probabilistic theory for kinetics of small systems has been known for quite a long time [31], not until 1990 was it applied to cellular or microbial adhesions [32, 33]. The idea is that the number of bonds that an adherent cell may have is a discrete, time-dependent, random variable that fluctuates significantly. To describe the state of the system requires a probability vector because any positive number of bonds could associate with an adhesion. Each possible scenario has a defined likelihood, given by a component of the probability vector. This is in contrast to the deterministic description that uses only a single scalar for the averaged number of bonds. The law of conservation of mass is thus replaced with the conservation of probability density for the low number of bonds. The probability of the cell adhesion states evolves due to the probability influxes and effluxes to and from these states.

Specific Adhesion Mechanisms

As described earlier, cells express surface associated proteins (“adhesins”) that can bind specifically to complementary proteins expressed by the host, and the presence of these binding interactions can have a significant effect on the adhesion of cells to surfaces. Most bacterial pathogens produce MSCRAMMs (microbial surface

components recognizing adhesive matrix molecules), which are a sub-family of adhesins that react specifically with extracellular matrix molecules. For example, the specific binding interaction between the MSCRAMM “clumping factor”, expressed by bacterium *Staphylococcus aureus*, and the extracellular matrix protein fibrinogen is associated with hospital-acquired infections, and this pair interaction serves as the model experimental system in Chapter 4 by which the effect of MSCRAMM length on cell-surface interaction forces and particle deposition rate constants is evaluated and compared with the predictive results using our dynamic model from Chapter 3. Also, many biomimetic experimental systems are constructed to carry out the relevant experiments *in vitro* to avoid *in vivo* complexity. One of such exemplary systems is to utilize the high specificity and affinity between biotin and (strept)avidin molecules, which is investigated in Chapter 6 using the optical trapping technique for a direct testing of our dynamic model in Chapter 3.

Several theoretical models to account for such specific molecular interactions are briefly introduced below. Bell and coworkers pioneered thermodynamic equilibrium approaches to cell-cell (or cell-surface) adhesion. The models they developed are to study the adhesion between two freely deformable cells with surface-bound receptors (mobile or immobile) [25, 34, 35]. They formulated an equation for the change in Gibbs free energy of a closed system containing two such deformable cells which changes from a state of no interaction to a state of adhesion. This equation allows them to calculate the equilibrium state by minimizing the Gibbs free energy at constant temperature and pressure¹ to find the contact area, cell-cell separation distance and number of bonds as a function of both receptor properties and non-specific

¹Here, the pressure should use surface pressure, because binding reactions between two reacting species take place in a two-dimensional contact region. Minimization of the Gibbs free energy should be performed under constant surface pressure instead of external pressure of the fluid surrounding the cell membranes, which is not expected to have much effect on surface thermodynamics.

interactions. However, in their models, the cell membrane deformation energy is neglected in the minimization of free energy; and also the kinetic process involved in reaching adhesive equilibrium is not taken into account at all.

Developing dynamic models for cellular adhesion allows us to investigate the equilibrium state of the cell as well as the kinetics of the formation of that state. In many physiological environments, cells are flowing through the body's circulatory systems. Adhesion of cells to corresponding surfaces under such conditions may not reach the equilibrium state before the cells are able to form enough bonds to resist detachment forces. Therefore, kinetic analysis of cell adhesion may provide useful information on adhesion mechanism under these circumstances. Hammer and Lauffenburger [36] developed a dynamic model for the receptor-mediated cell adhesion to a ligand-coated surface to study the outcome of a cell transiently encountering the surface under fluid shear flow. The kinetic species balances were used to study the time-course of bond number density as well as surface density for free receptors. After a given time period (should be long enough for binding reactions to occur), if bond number density is zero, the cell will not adhere to the surface during the encounter; but if bond number density approaches to a non-zero steady state value, the cell must become stably attached. Although such a deterministic model is useful and successful in explaining many experimental observations, it predicts either no adhesion or all adhesion ("none or all") results, and thus fails to predict the intermediate cases. Cozens-Roberts and coworkers extended the deterministic dynamic model by Hammer and Lauffenburger to a probabilistic framework, in which they calculated the probability that a certain number of bonds between a cell and a surface exists at any given time [32, 33, 37]. As described earlier, the probabilistic nature of binding kinetics is inherent in the system involving relatively small number of reacting molecules, such as for the case of receptor molecules over the cell surface. The

key difference from the earlier model is that the binding kinetics is cast in probabilistic rather than deterministic form. Applications of these models in real living cells are still limited because of the complexity of *in-vivo* cell systems. In addition, a combination of mechanical and dynamic approaches was also used for studying cell attachment and detachment [26]. Dickinson developed a dynamic model to predict the attachment rate constant of a rigid Brownian particle to a surface mediated by both colloidal forces and macromolecular binding interactions [38]. Considering Brownian motions (for micron sized particles) and binding as two coupled stochastic processes, the model derived a time-dependent probability density equation to describe the probability for the particle of having a certain bond number at a certain separation distance from the surface. Then, the steady-state probability flux of particles to a surface was examined as a function of the binding parameters, such as the surface density of binding molecules, the rate constants of binding and dissociation, and the effective length of the bonds. Analytical solutions were obtained for the deposition rate constant for the limiting cases of slow or fast binding relative to the rate particle diffusion. However, the intermediate case where both processes are similarly fast required numerical solution. In Chapter 3, similar theoretical framework as Dickinson's model but a new approach is used to obtain the deposition rate constant of biological particles to a surface (please also see Ref. [39]).

2.3 Techniques for Measuring Particle Attachment

As described earlier, adhesive interaction between a biological particle (or a cell) and a surface is a result of net contributions from both non-specific forces, such as van der Waals, electrostatic, steric stabilization, and the biochemically specific receptor-ligand binding interactions. Thus, particle-surface reaction kinetics depends upon the particle and surface properties, the medium composition, and external forces, such as depositional and hydrodynamic forces. Due to complexity from

physiological conditions, *in vitro* assays are typically used for studying transient behaviors of particle or cell adhesion (although *in vivo* experiments have also been performed with implanted grafts [40, 41]). Experiments relevant to cellular adhesion can be roughly classified into two categories: adhesion kinetics and adhesion strength. Below we describe in brief the common techniques used in each category.

2.3.1 Adhesion Kinetics

Particle adhesion kinetics can be studied through kinetic analysis of attachment as well as detachment measurements. In general, attachment kinetic experiments are performed by incubating the biological particles (or cells) and surface for a variable amount of time (the attachment time) and then subjecting the particles to a constant external force for a given amount of time. These experiments provide data on the percentage of adherent particles before and after exposure to the force as a function of the attachment time. In general, detachment kinetic experiments are performed by incubating the particles and the surface for a given amount of time and then exposing the particles to a constant external force for a various amount of time. The common methods used to exert force on the cells are: micromanipulation, centrifugation, and hydrodynamic shear.

In micromanipulation, the particle is held in a micropipette and brought into contact with an affinity surface; the particle is then withdrawn from the receiving surface after a specified amount of time by increasing the suction pressure of the micropipette. In fact, this assay has also been used to generate useful information on the adhesive force between a biological particle and a surface and also on the mechanical properties of the cell membrane [42]. In centrifugation, particles are allowed to settle onto a receiving surface under the influence of gravity for a period of time and then centrifuged. Hydrodynamic shear assays can be divided into the following categories: flow between parallel plates, flow between a rotating disc and a stationary disc, flow between a rotating cone and a stationary disc, and axisymmetric

flow between parallel discs. If the hydrodynamic fluid shear is used as a means for external force application, accurate interpretation of experimental measurement data requires to quantify the influence of fluid flow, which includes transport and wall shear effects. Thus, flow cells for direct visualization and real-time measurement under well-defined flow conditions have been developed [2, 43].

To demonstrate how to extract adhesion kinetics information from these experimental measurements, an equation for obtaining particle attachment rate constants is given below using parallel flow chambers along with automated video microscopy systems, which measures the time course of the changes in the surface concentration of particles [43]. Within the diffusive boundary layer distance, the steady-state flux of particles over this boundary is proportional to the particle concentration at this boundary by applying first-order kinetics. This flux is equal to the rate of accumulation of particles on the surface, thus, one can obtain the deposition rate constant, k_+ , from the following relationship [2]

$$\frac{dc_s}{dt} = k_+ c, \quad (2.3)$$

where c_s is the attached particle density on the surface; and c is the concentration of particles at the boundary layer distance along the flow direction.

2.3.2 Adhesion Strength

The strength of particle adhesion is a critical determinant in many physiological processes, for example, in cell locomotion where bonds must be formed and broken in a tightly controlled manner. The measurement of adhesion strength is achieved by relating the mechanically applied tension strength on the cell membrane to adhesive energy, which shares similarity with the mechanics of peeling of an adhesive tape. Corresponding theoretical models to support this method were first developed by Evans [44, 45, 46], in which the forces due to “pulling” on cell membrane are assumed to be in balance with the resistance by receptor-ligand bonds. Then, Dembo *et al.* [26] combined cell deformation mechanics with receptor-ligand binding kinetics

to develop a dynamic and mechanical approach to cell attachment and detachment. This model is capable of describing the relationship between the transient behavior of contact zone spreading or shrinking and cell binding properties. Later, Kuo and Lauffenburger [47] used the radial flow chamber to measure the critical shear stress for detachment of receptor-coated beads from a ligand-coated substratum as a function of receptor density.

Over the past decade, more and more research groups have been focusing on studying the strength of a single receptor-ligand bond. Most direct measurements of single bond strength have been performed with four types of ultrasensitive probes: the atomic force microscope (AFM) [48, 49], where force is sensed by deflection of a thin silicon nitride cantilever; the biomembrane force probe (BFP) [42, 50], where force is sensed by axial displacement of a glass microsphere glued to the pole of a micropipet-pressurized membrane capsule; the laser optical tweezer (LOT) [51], where force is sensed by displacement of a microsphere trapped in a narrowly focused beam of laser light; and the dynamic force spectroscopy (DFS), which is similar to BFP while thermal fluctuations of probes are also accounted for in data analysis [52, 53, 54]. These probes are able to detect forces in the range of $< 1 \text{ pN/nm}$ to 1 nN/nm .

CHAPTER 3 ATTACHMENT KINETICS OF BIOLOGICAL PARTICLES TO SURFACES

As well known, real cells are of complex shapes and structures. To have a complete understanding of cellular adhesion requires that not only the whole cell be investigated in attempts to model the biological behavior of the cell surface, but also that the functions and behaviors of each individual component inside the cell be examined. Therefore, the combined knowledge from many different fields will be needed to depict a full picture of the cell adhesion, such as the biological, molecular, quantitative behaviors of the cell, and so on. In this chapter here, to make complex materials simple, we shall study the attachment mechanism of a rigid biological particle, instead of a real cell, to a surface through receptor-ligand or other macromolecular binding interactions. The chemistry of the system is ignored, in an analogy to the treatment of polymers as long chains by Professor de Gennes [55]¹. In this way, we are hoping that the underlying physics for this simple system will help shed some light into the complex adhesion mechanism of actual cellular systems.

From the description in Chapter 2, attachment of a free particle (or a cell) from a fluid suspension to a surface usually involves two major competing processes: (i) Brownian motions of a particle, which is more significant for smaller particles (e.g., on the order of micron or submicron size); and (ii) interaction forces between the particle and the surface. Which one of these two processes limits the overall attachment rate of particles to surface is of great interests for both fundamental researches and practical applications. In fact, in many cases, macromolecular bond

¹Perhaps Prof. de Gennes's greatest attribute is to make complex materials appear simple. In this treatment of polymers, the chemistry of the polymer is ignored so that one can look at the underlying physics for this polymer by treating it as a long chain.

formation and dissociation may occur on a time-scale comparable to the time-scale of particle diffusion near a surface, such that the forces involved in binding may not be assumed to be at equilibrium, as treated in DLVO theory. Therefore, in this chapter, we shall develop a dynamic model to predict particle attachment rate constant for a general case when the specific binding forces cannot be assumed at equilibrium.

3.1 Particle-Surface Interaction Energy

Let us first start with thermodynamic analysis of the interactions between a rigid biological particle and a surface in the presence of binding macromolecules. Figure 3.1 illustrates the particle-surface system under consideration, which is a simple case for receptor-mediated cell adhesion. The particle is covered uniformly with binding macromolecules (or receptors), and the substratum is coated with complementary binding sites (or ligands) in great excess, hence, the surface density for the binding sites can be treated as constant. Upon close approach to the surface, a flat and constant contact area for macromolecular binding at the interface between the particle and the surface is assumed throughout the whole attachment period. Here, we shall focus on the initial adhesion for this rigid particle to the surface (in other words, the spreading and deformation of real cells are not considered). Suppose there are N identical surface-bound molecules available for binding in the contact area to form n bonds between the particle and the surface. The total particle-surface interaction energy at the interface is the sum of the energy of n bonds and the non-specific interactions, $\phi(z)$, which is dependent on the separation distance, z , of the particle from the surface, as illustrated in Figure 3.1. Here $\phi(z)$ includes electrostatic repulsions, van der Waals attractions, steric stabilization, hydrophobic forces, and any other surface-independent body interactions such as gravitation. The energy of every single bond, $\epsilon(z)$, is also a function of z due to stretching and/or compression of the bond away from its equilibrium position. The Helmholtz free energy at the interface,

$A(n, z)$, is then given by

$$A(n, z) = \phi(z) + n\epsilon(z) - TS(n) \quad (3.1)$$

$$= \phi(z) + n\epsilon(z) - k_B T \ln \left(\frac{N!}{n!(N-n)!} \right), \quad (3.2)$$

where the entropy, S , is determined by the degeneracy of the system with n bonds at N binding macromolecules:

$$S = k_B \ln \left(\frac{N!}{n!(N-n)!} \right). \quad (3.3)$$

Upon using the Stirlings approximation for large N and n , the free energy in Eq. (3.2) becomes ²

$$A(n, z) = \phi(z) + n\epsilon(z) + (N-n)k_B T \ln \left(\frac{N-n}{N} \right) + nk_B T \ln \left(\frac{n}{N} \right). \quad (3.4)$$

In general, analysis here can be applied for any reasonable functions $\phi(z)$ and $\epsilon(z)$, provided that the energy maximum in $\phi(z)$ lies within the interaction domain of the bridging macromolecules. According to the study of cell-cell adhesion by Bongrand and Bell [16], the attractive van der Waals forces between cells are negligible and the repulsive energy barrier arises mainly from a combination of two effects: (i) electrostatic double layer repulsion due to the negatively charged cell surfaces [15], and (ii) the steric stabilization effect as a result of the presence of a hydrated polymer layer on cell membranes (e.g., glycocalyx) [56]. As a first approximation, $\phi(z)$ is assumed to consist of a phenomenological equation to account for both electrostatic repulsion and steric stabilization force and a superimposed parabolic potential around the center, z_p :

$$\phi(z) = \phi_0 e^{-bz} + \frac{1}{2} \gamma_p (z - z_p)^2, \quad (3.5)$$

where ϕ_0 represents the baseline repulsive potential, the parameter b is the inverse decay length for repulsion. As shown in the following sections, the functional form

²The unstressed bond energy, ϵ_0 , for typical reversible specific receptor-ligand binding interaction is usually about several $k_B T$, and bond number n is relatively small compared to N , so, the entropic contribution to the overall binding energy is dominant, as indicated in Eq. (3.4).

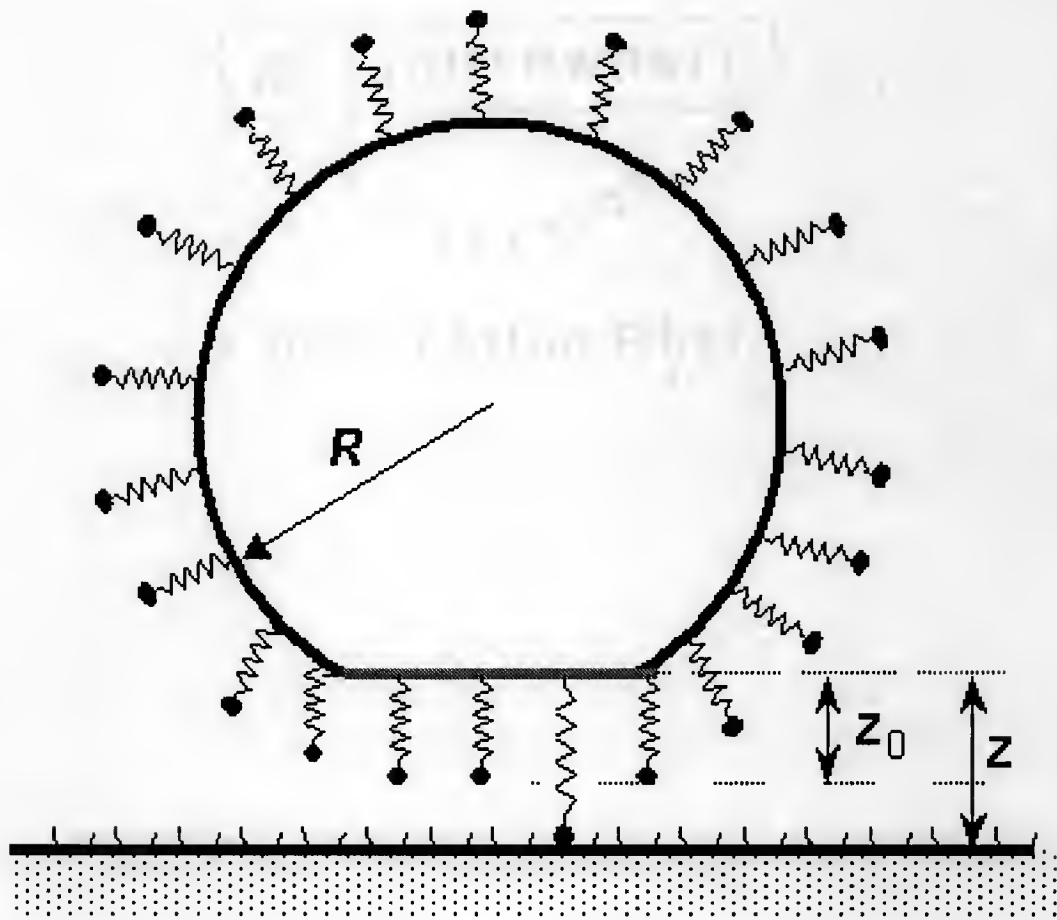


Figure 3.1: A schematic of particle-surface interaction through macromolecular binding. The bonds illustrated here are treated as ideal springs with bond energy increasing parabolically when being stretched or compressed away from their equilibrium position, z_0 .

of $\phi(z)$ is not essential to the analysis, as long as there are no net repulsive forces around the secondary energy minimum, see Figure 3.2. The energy of bonds and the kinetic rate constants are determined by the physical and chemical properties of the specific binding macromolecules. Here for simplicity, the bonds formed in the interface are treated as ideal springs with energy increasing quadratically when being strained or stressed away from their minimal energy bond length, z_0 . Thus,

$$\epsilon(z) = \epsilon_0 + \frac{1}{2}\gamma_b(z - z_0)^2, \quad (3.6)$$

where $\epsilon_0 = \epsilon(z_0)$ and γ_b is bond stiffness. As for the real receptor-ligand bonds, the ideal “spring model” used here might not be a good one, however, if any better models for these bonds are developed, they can simply replace Eq. (3.6).

Shown in Figure 3.2 is a theoretical contour plot of $A(n, z)$ as functions of bond number n and separation distance z based upon the above representative expressions for $\phi(z)$ and $\epsilon(z)$ using the parameter values listed in Table 3.1. Two minima exist in the plot: a primary minimum with $n > 0$ corresponding to an attached particle with multiple bonds, and a secondary minimum at larger separation distance with $n = 0$ where essentially only long range colloidal forces dominate. To attach to the surface, a particle has to move from the secondary (2°) minimum, over the transition saddle point, and into the primary (1°) energy minimum. In the following section, we derive a Fokker-Planck equation to predict the probability flux of the particle from the unattached state (2° energy minimum) to the attached state (1° energy minimum) using an energy landscape determined by both colloidal and binding interaction forces.

3.2 Probability Flux

Let us first analyze the forces acting on the particle. These forces include the deterministic force in z direction, $-\frac{\partial A(n, z)}{\partial z}$, a fluctuating force (namely, the thermal force that results in Brownian fluctuations of the particle), and the bridging force to

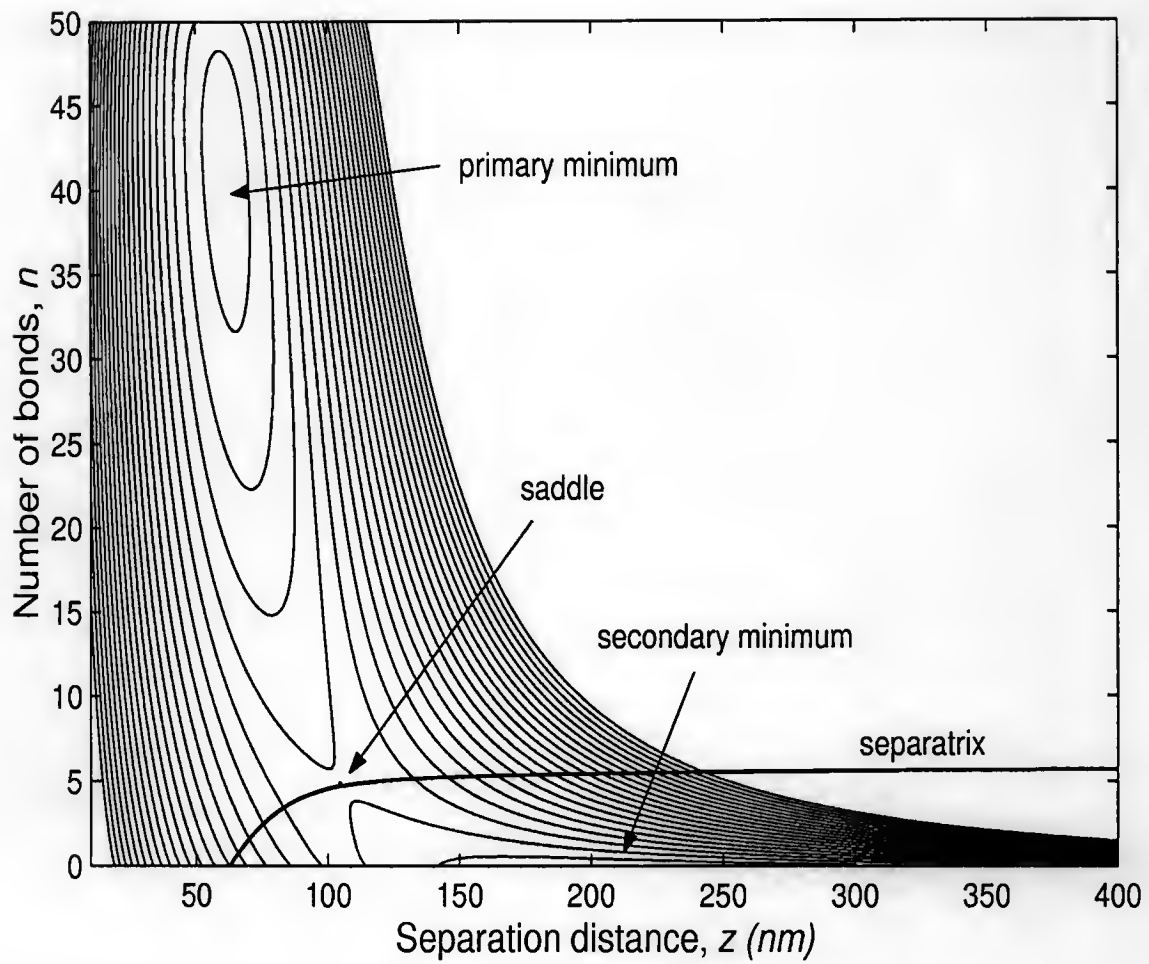


Figure 3.2: A hypothetical contour plot of the thermodynamic free energy, $A(n, z)$, as a function of bond number, n , and separation distance, z . To attach to a surface, a particle must move from the secondary energy minimum, over the transition saddle point and into the primary minimum. The separatrix boundary which passes through the saddle point and separates the two energy minima is shown by the solid line.

Table 3.1: Base parameter values

Symbol	Base value	Parameter
N	50	Number of binding molecules
ϕ_0	$90 k_B T$	Baseline repulsive potential
b	0.02 nm^{-1}	Repulsive decay length
ϵ_0	$-1 k_B T$	Unstrained bond energy
γ_b	$0.002 k_B T/\text{nm}^2$	Bond stiffness
z_0	40 nm	Unstrained bond length
γ_p	$8 \times 10^{-4} k_B T/\text{nm}^2$	Optical trap stiffness
z_p	200 nm	Optical trap center
k_{f0}	1000 s^{-1}	Forward binding rate constant
Δ	0.5 nm	Bond length at transition state
R	300 nm	Particle radius
L	1 μm	Boundary layer thickness
a_0	$0.5 k_B T$	Baseline polynomial potential
a_1	$0 k_B T/\text{nm}$	Potential coefficient
a_2	$10^{-3} k_B T/\text{nm}^2$	Potential coefficient
a_3	$-10^{-6} k_B T/\text{nm}^3$	Potential coefficient
a_4	$0 k_B T/\text{nm}^4$	Potential coefficient

form n bonds. The deterministic force consists of particle inertial forces and hydrodynamic drag forces. Assuming inertial forces are negligible compared to hydrodynamic drag forces at low Reynolds number, the drift velocity of the particle in z direction is the deterministic force divided by the hydrodynamic drag coefficient, $\delta(z)$, (for all the results shown later, the functional form of $\delta(z)$ for a sphere descending normally to a solid surface as solved by Brenner is used [57]); and $\delta(z)$ can then be determined using Stokes-Einstein equation by the diffusion coefficient of the particle, $D(z)$:

$$V(z; n) = -\frac{1}{\delta(z)} \frac{\partial A(n, z)}{\partial z} \quad (3.7)$$

$$= -\frac{D(z)}{k_B T} \frac{\partial A(n, z)}{\partial z}, \quad (3.8)$$

where $V(z; n)$ is the drift velocity of the particle in z direction.

Next we consider the dynamic process of particle attachment in terms of the probability flux into the primary energy minimum on the energy landscape shown in Figure 3.2. Assuming Markov processes in both variables z and n (*i.e.*, the future statistics depend only on the present, not their history), the balance equation for the particle is

$$\partial_t p(n, z, t) = -\partial_z J_z - (J_{n+1 \rightarrow n} - J_{n \rightarrow n-1}), \quad (3.9)$$

where $p(n, z, t)$ is the joint probability density of the particle being located at distance z with n bonds at time t . J_z , the probability flux J in the z direction, is given by

$$J_z = -\frac{D(z)}{k_B T} \frac{\partial A(n, z)}{\partial z} p(n, z, t) - D(z) \partial_z p(n, z, t). \quad (3.10)$$

The primary assumptions underlying Eq. (3.10) are the validity of Eq. (3.7) (viscous drag force proportional to velocity) and a fast relaxation of velocity fluctuations relative to the time scale of interest, which is usually true for the particle size within the colloidal domain. And the probability flux in the discrete n dimension, $J_{n \rightarrow n-1}$, is given by

$$J_{n \rightarrow n-1} = -k_r(z) n p(n, z, t) + k_f(z) [N - (n - 1)] p(n - 1, z, t), \quad (3.11)$$

where $k_r(z)$ and $k_f(z)$ are the rate constants of bond dissociation and formation, respectively.

The boundary conditions for Eq. (3.9) are determined by the physical limitations on n and z and on how an “attached” particle is defined. Because $z \geq 0$, the no flux boundary condition at $z = 0$ is $J_z(n, 0) = 0$. Similarly, since $0 \leq n \leq N$, the no-flux boundary conditions in the n -dimension are $J_{n \rightarrow n-1}(0, z) = 0$ and $J_{n \rightarrow n-1}(N, z) = 0$. Furthermore, the bonds are assumed not be able to exist at separation distances larger than the diffusive layer thickness L , such that $J_z(n > 0, L) = 0$.

In the following section, the mean first-passage time approach to solve Eq. (3.9) to get the attachment rate of the particle to a surface is described.

3.3 Mean First Passage Time Approach

As mentioned earlier, to attach to a surface, a particle must move from the unattached state (*i.e.*, the secondary minimum as shown in Figure 3.2), cross over the energy barrier on the transition state and fall into the primary potential well to become attached. Suppose the potential energy in the attached state is sufficiently lower than that at transition state, the relaxation time for the particle from the transition state to attachment is negligible, therefore, once the time required for the particle from the unattached to the transition state is calculated, the rate constant of particle attachment to the surface can then be deduced. In what follows, the mean first-passage time method is described in brief to obtain the mean transition time.

Consider a homogeneous Markov process within a system Ω which contains a single energy minimum (*e.g.*, the region of the secondary energy minimum as illustrated in Figure 3.2). The first-passage time formalism determines the mean time $T(n, z)$ required for a particle starting at $[n, z] \in \Omega$ to exit through a specified boundary $\partial\Omega$ (in our case here, the separatrix containing the saddle point between the two energy minima, also indicated in Figure 3.2). The probability that at time t the

particle is still in Ω is

$$\int_{\Omega} p(n', z', t | n, z, 0) dn' dz' \equiv G(n, z, t), \quad (3.12)$$

which essentially is the probability $\text{Prob}(T \geq t)$, where T is the time the particle leaves the system. The boundary conditions are

$$\begin{aligned} G(n, z, t) &= 1, & [n, z] \in \Omega - \partial\Omega \\ &= 0, & [n, z] \in \partial\Omega \end{aligned} \quad (3.13)$$

The mean first passage time, $T(n, z)$, is given by

$$\begin{aligned} T(n, z) &= \langle T \rangle = - \int_0^\infty t dG(n, z, t) \\ &= \int_0^\infty G(n, z, t) dt, \end{aligned} \quad (3.14)$$

where the last term is obtained using integration by parts. Since the system is time homogeneous, one can use the backward equation for Eq. (3.9), that is [58]

$$\begin{aligned} \partial_t p(n', z', t | n, z, 0) &= -\frac{D(z)}{k_B T} \frac{\partial A(n, z)}{\partial z} \partial_z p(n', z', t | n, z, 0) + D(z) \frac{\partial^2}{\partial z^2} p(n', z', t | n, z, 0) \\ &\quad + k_f(z) (N - n) [p(n + 1', z', t | n + 1, z, 0) - p(n', z', t | n, z, 0)] \\ &\quad + k_r(z) n [p(n - 1', z', t | n - 1, z, 0) - p(n', z', t | n, z, 0)]. \end{aligned} \quad (3.15)$$

In view of Eq. (3.12), one gets

$$\begin{aligned} \partial_t G(n, z, t) &= -\frac{D(z)}{k_B T} \frac{\partial A(n, z)}{\partial z} \partial_z G(n, z, t) + D(z) \frac{\partial^2}{\partial z^2} G(n, z, t) \\ &\quad + k_f(z) (N - n) [G(n + 1, z, t) - G(n, z, t)] \\ &\quad + k_r(z) n [G(n - 1, z, t) - G(n, z, t)]. \end{aligned} \quad (3.16)$$

Integrating Eq. (3.16) over $(0, \infty)$, one gets for the left-hand side of this equation

$$\int_0^\infty \partial_t G(n, z, t) dt = G(n, z, \infty) - G(n, z, 0) = -1, \quad (3.17)$$

where we have used the fact $G(n, z, \infty) = 0$, as $t \rightarrow \infty$; then one obtains the following expression by using Eq. (3.14) for the right-hand side

$$\begin{aligned} L^+T(n, z) &= -\frac{D(z)}{k_B T} \frac{\partial A(n, z)}{\partial z} \frac{\partial T(n, z)}{\partial z} + D(z) \frac{\partial^2 T(n, z)}{\partial z^2} \\ &\quad + k_f(z)(N - n)[T(n + 1, z) - T(n, z)] + k_r(z)n[T(n - 1, z) - T(n, z)] \\ &= -1, \end{aligned} \quad (3.18)$$

with the boundary condition

$$T(n, z) = 0, \quad [n, z] \in \partial\Omega \quad \text{separatrix.} \quad (3.19)$$

Because of the difficulty in analytically solving Eq. (3.18), next, we seek both numerical method and analytical approximations and then compare the results obtained from both methods.

3.3.1 Numerical Method

Finite difference method is used to numerically solve Eq. (3.18) subjected to the boundary conditions in Eq. (3.19) [59]. The code is written in MatLab and attached in Appendix. The separatrix boundary which separates the two energy minima and goes through the saddle point, as illustrated in Figure 3.2, is dynamically determined by simulating into which energy well the particle would go starting from point $(n, z) \in \Omega$ based on their deterministic equations:

$$\frac{dz}{dt} = -\frac{D(z)}{k_B T} \frac{\partial A(n, z)}{\partial z}, \quad (3.20)$$

$$\frac{dn}{dt} = k_f(z)(N - n) - k_r(z)n. \quad (3.21)$$

Clearly, the position of the separatrix is directly related to velocity, diffusion, kinetic rate constants of the particle as well as potential energy. Any factor that could influence these parameters, such as particle size, bond energy, forward binding rate constants, would change separatrix location. Therefore, the separatrix should be determined first for every data set prior to the run of the program to obtain the mean

first-passage time $T(n, z)$ in Eq. (3.18). The same boundary conditions as those for Eq. (3.9) apply here also, which are converted in terms of $T(n, z)$ as follows:

$$\begin{aligned}[T(n, z) - T(n-1, z)]|_{n=0} &= 0, \\ [T(n+1, z) - T(n, z)]|_{n=N} &= 0, \\ \partial_z T(n, z)|_{z=L} &= 0, \\ T(n, z) &= 0, \quad [n, z] \in \partial\Omega \quad \text{separatrix.} \end{aligned}\quad (3.22)$$

3.3.2 Analytical Approximations

In this section, an analytical approach is described to obtain the mean first-passage time as well as particle attachment rate constant from the dynamic model in Eq. (3.9). First a Fokker-Planck equation is derived for the probability density of a particle with respect to bond number and separation distance from a surface, using an appropriate free energy landscape determined by the colloidal and binding energies. This equation is then used in the MFPT approximation to predict the probability flux over the saddle transition state from the secondary energy minimum corresponding to the unattached state.

Derivation of a Fokker-Plank Equation

Usually the receptor number over the cell surface is on the order of $10^3 \sim 10^7$ [16]. Thus, it is reasonable to assume that there will be plenty of binding molecules (or receptors) available in the contact region between the particle and the surface. So below we shall examine Eq. (3.9) under this condition. In the large N limit, the number of bonds formed between the particle and the surface fluctuates around its equilibrium value with a width of order $N^{1/2}$ [60]. As previously mentioned, in order to attach to a surface, a particle must cross over an energy barrier at a saddle point. Thus, the number of bonds formed at the saddle point gives us a good reference regarding to the fluctuations in bond number. Therefore, a new variable ξ

is introduced so that

$$n = n_{eq}(z_s) + N^{1/2}\xi, \quad (3.23)$$

where z_s is the separation distance for the saddle point from the surface, and $n_{eq}(z_s)$ is the equilibrium bond number at saddle. Then an operator \mathbf{E} is defined by its effect on an arbitrary function $f(n)$:

$$\begin{aligned} \mathbf{E}f(n) &= f(n+1), \\ \mathbf{E}^{-1}f(n) &= f(n-1). \end{aligned} \quad (3.24)$$

By so doing, the probability conservation equation for the particle, Eq. (3.9), can be rewritten as

$$\partial_t p(n, z, t) = -\partial_z J_z + k_f(z) (\mathbf{E}^{-1} - 1) (N - n) p(n, z, t) + k_r(z) (\mathbf{E} - 1) n p(n, z, t). \quad (3.25)$$

The operator \mathbf{E} changes n to $n + 1$ and therefore ξ to $\xi + N^{-1/2}$, such that

$$\begin{aligned} \mathbf{E} &= 1 + N^{-1/2} \frac{\partial}{\partial \xi} + \frac{1}{2} N^{-1} \frac{\partial^2}{\partial \xi^2} + \dots \\ &= \sum_{m=0}^{\infty} \frac{(N^{-1/2})^m}{m!} \frac{\partial^m}{\partial \xi^m}. \end{aligned} \quad (3.26)$$

Therefore, the discrete variable n is now approximated as a continuous fluctuating variable ξ , and the change for ξ can be written in powers of small parameter $N^{-1/2}$. Substitution of Eq. (3.26) into Eq. (3.25) to change the variable n to ξ yields [58, 60]:

$$\begin{aligned} \partial_t p(\xi, z, t) &= -\partial_z J_z + k_f(z) \sum_{m=1}^{\infty} \frac{(-N^{-1/2})^m}{m!} \frac{\partial^m}{\partial \xi^m} [N - n_{eq}(z_s) - N^{1/2}\xi] p(\xi, z, t) \\ &\quad + k_r(z) \sum_{m=1}^{\infty} \frac{(N^{-1/2})^m}{m!} \frac{\partial^m}{\partial \xi^m} [n_{eq}(z_s) + N^{1/2}\xi] p(\xi, z, t). \end{aligned} \quad (3.27)$$

Rearranging Eq. (3.27) yields

$$\partial_t p(\xi, z, t) = -\partial_z J_z + \sum_{m=1}^{\infty} \frac{(-1)^m N^{1-m/2}}{m!} \frac{\partial^m}{\partial \xi^m} \left[\alpha_m(z) - \frac{\beta_m(\xi, z)}{N^{1/2}} \right] p(\xi, z, t), \quad (3.28)$$

with

$$\alpha_m(z) = k_f(z) \left[1 - \frac{n_{eq}(z_s)}{N} \right] + (-1)^m k_r(z) \left[\frac{n_{eq}(z_s)}{N} \right], \quad (3.29)$$

$$\beta_m(\xi, z) = [k_f(z) - (-1)^m k_r(z)] \xi. \quad (3.30)$$

For the large N limit, only the terms of order $O(1)$ or higher order of $N^{1/2}$ will survive and all the other terms with higher powers of $N^{-1/2}$ vanish. Therefore, by truncating Eq. (3.28) at $m = 2$ and collecting the terms of $O(1)$ and $O(N^{1/2})$, we get a Fokker-Planck equation for the probability density in terms of z and ξ

$$\begin{aligned} \partial_t p(\xi, z, t) = & -\partial_z J_z \\ & + \frac{\partial}{\partial \xi} \left\{ N^{1/2} \left[(k_f(z) + k_r(z)) \frac{n_{eq}(z_s)}{N} - k_f(z) \right] + [k_f(z) + k_r(z)] \xi \right\} p(\xi, z, t) \\ & + \frac{1}{2} \left\{ k_f(z) + [k_r(z) - k_f(z)] \frac{n_{eq}(z_s)}{N} \right\} \frac{\partial^2}{\partial \xi^2} p(\xi, z, t). \end{aligned} \quad (3.31)$$

Since each binding macromolecule will be in either free or bound state with binding energy either 0 or $\epsilon(z)$, respectively, the probability of such binding molecules being in bound state is $\frac{e^{-\epsilon(z)/k_B T}}{1 + e^{-\epsilon(z)/k_B T}}$. Thus, the number of bonds at equilibrium is

$$n_{eq}(z) = N \frac{e^{-\epsilon(z)/k_B T}}{1 + e^{-\epsilon(z)/k_B T}}, \quad (3.32)$$

and the equilibrium constant is then given by

$$K_{eq}(z) = \frac{n_{eq}(z)}{N - n_{eq}(z)} = e^{-\epsilon(z)/k_B T}. \quad (3.33)$$

In view of Eqs. (3.32) and (3.33), Eq. (3.31) now becomes

$$\begin{aligned} \partial_t p(\xi, z, t) = & -\partial_z J_z \\ & + \frac{\partial}{\partial \xi} \left\{ N^{1/2} k_r(z) \frac{K_{eq}(z_s) - K_{eq}(z)}{1 + K_{eq}(z_s)} + k_r(z) [1 + K_{eq}(z)] \xi \right\} p(\xi, z, t) \\ & + \frac{1}{2} k_r(z) \frac{K_{eq}(z) + K_{eq}(z_s)}{1 + K_{eq}(z_s)} \frac{\partial^2}{\partial \xi^2} p(\xi, z, t). \end{aligned} \quad (3.34)$$

(Here, again we have used $K_{eq}(z) = \frac{k_f(z)}{k_r(z)}$.) The stationary probability is known as

$$p_s(\xi, z) = N^{-1} e^{-A(\xi, z)/k_B T}, \quad (3.35)$$

with \mathbb{N} being the normalization constant and $A(\xi, z)$ is obtained by replacement of n with ξ in Eq. (3.4) as

$$\begin{aligned} A(\xi, z) = & \phi(z) + [n_{eq}(z_s) + N^{1/2}\xi] \epsilon(z) \\ & + [N - n_{eq}(z_s) - N^{1/2}\xi] k_B T \ln \left[\frac{N - n_{eq}(z_s) - N^{1/2}\xi}{N} \right] \\ & + [n_{eq}(z_s) + N^{1/2}\xi] k_B T \ln \left[\frac{n_{eq}(z_s) + N^{1/2}\xi}{N} \right]. \end{aligned} \quad (3.36)$$

Therefore, for the Fokker-Planck dynamics in Eq. (3.34), the drift term in ξ dimension is not derivable from the potential $A(\xi, z)$ (“potential conditions” are not satisfied here [61, 62]), but rather from another potential which is expressible as the line integral of the drift and diffusion terms in ξ dimension:

$$B(\xi, z) = 2N^{1/2}k_B T \frac{K_{eq}(z_s) - K_{eq}(z)}{K_{eq}(z_s) + K_{eq}(z)} \xi + k_B T \frac{[1 + K_{eq}(z_s)][1 + K_{eq}(z)]}{K_{eq}(z_s) + K_{eq}(z)} \xi^2 + C(z), \quad (3.37)$$

where $C(z)$ is only a function of z . Combination of Eqs. (3.10), (3.34), (3.36) and (3.37) leads to

$$\begin{aligned} \partial_t p(\xi, z, t) = & \frac{\partial}{\partial z} \left[\frac{D(z)}{k_B T} \frac{\partial A(\xi, z)}{\partial z} p(\xi, z, t) + D(z) \frac{\partial}{\partial z} p(\xi, z, t) \right] \\ & + \frac{\partial}{\partial \xi} \left[\frac{\eta(z)}{k_B T} \frac{\partial B(\xi, z)}{\partial \xi} p(\xi, z, t) + \eta(z) \frac{\partial}{\partial \xi} p(\xi, z, t) \right], \end{aligned} \quad (3.38)$$

with

$$\eta(z) = \frac{1}{2} k_r(z) \frac{K_{eq}(z) + K_{eq}(z_s)}{1 + K_{eq}(z_s)}, \quad (3.39)$$

defining the effective diffusion coefficient in the ξ dimension.

Dimensionless Fokker-Planck Equation

Since a particle must pass over an energy barrier at a saddle point to attach to a surface, the properties of the saddle point which separates the two energy minima are very critical for determining the rate of particle attachment. Below, we scale the above Fokker-Planck equation, *i.e.*, Eq. (3.38), using the values of its key parameters at the saddle point. We first define parameter

$$\varepsilon = \frac{k_B T}{\Delta A}, \quad (3.40)$$

where $\Delta A = A(\xi_s = 0, z_s) - A(\xi_m, z_m)$ is the barrier height determined by the free energy at the saddle, $[\xi_s = 0, z_s]$, with respect to a reference energy minimum, $[\xi_m, z_m]$ (e.g., the secondary energy minimum of Eq. (3.36)); and ε represents the relative noise strength. Then we introduce a length scale $l = |z_s - z_m|$, which is the distance between the saddle and the reference minimum, and define

$$y = \frac{z}{l}. \quad (3.41)$$

Using the newly defined parameters in Eqs. (3.40) and (3.41), now Eq. (3.38) becomes

$$\begin{aligned} \partial_\tau p(\xi, y, \tau) = & \frac{\partial}{\partial y} \left[\chi(y) \frac{\partial \alpha(\xi, y)}{\partial y} p(\xi, y, \tau) + \varepsilon \chi(y) \frac{\partial}{\partial y} p(\xi, y, \tau) \right] \\ & + \gamma \frac{\partial}{\partial \xi} \left[\zeta(y) \frac{\partial \beta(\xi, y)}{\partial \xi} p(\xi, y, \tau) + \varepsilon \zeta(y) \frac{\partial}{\partial \xi} p(\xi, y, \tau) \right], \end{aligned} \quad (3.42)$$

where

$$\alpha(\xi, y) = \frac{A(\xi, z)}{\Delta A}, \quad (3.43)$$

$$\beta(\xi, y) = \frac{B(\xi, z)}{\Delta A}, \quad (3.44)$$

$$\chi(y) = \frac{D(z)}{D(z_s)}, \quad (3.45)$$

$$\zeta(y) = \frac{\eta(z)}{\eta(z_s)}, \quad (3.46)$$

$$\tau = \frac{t D(z_s) \Delta A}{l^2 k_B T}, \quad (3.47)$$

and

$$\gamma = l^2 \frac{\eta(z_s)}{D(z_s)}. \quad (3.48)$$

In a brief summary for the previous several sections, by approximating the discontinuity of the bonds formed between the particle and the surface as a continuously fluctuating variable ξ in the limit of large number of available binding macromolecules, a two-dimensional Fokker-Planck equation can be derived to describe the

probability flux of the particle to the surface based upon a proper free energy landscape determined by the colloidal and binding interactions. Next we shall solve the Fokker-Planck equation using MFPT approach to evaluate the particle attachment rate at low-noise, higher-energy-barrier limit.

MFPT at High-Energy Barrier and Low-Noise Limit

Similar to the derivation for Eq. (3.18), it is straightforward to show that [58, 61]

$$L^+ \tau(\xi, y) = -1, \quad [\xi, y] \in \Omega - \partial\Omega, \quad (3.49)$$

where L^+ is the backward Fokker-Planck operator

$$\begin{aligned} L^+ = & -\chi(y) \frac{\partial \alpha(\xi, y)}{\partial y} \frac{\partial}{\partial y} + \varepsilon \chi(y) \frac{\partial^2}{\partial y^2} \\ & -\gamma \zeta(y) \frac{\partial \beta(\xi, y)}{\partial \xi} \frac{\partial}{\partial \xi} + \varepsilon \gamma \zeta(y) \frac{\partial^2}{\partial \xi^2}, \end{aligned} \quad (3.50)$$

and the corresponding boundary condition is

$$\tau(\xi, y) = 0, \quad [\xi, y] \in \partial\Omega. \quad (3.51)$$

In the limit of weak noise (*i.e.*, ε is small) and relatively high energy barrier, a realization of the process $[\xi(\tau), y(\tau)]$ will reside in Ω for a long enough time to assume a pseudo-stationary distribution before the thermal noise drives it over the boundary $\partial\Omega$. Hence, $\tau(\xi, y)$ becomes independent of $[\xi, y]$ ($\tau(\xi, y) \sim \tau_p$) practically everywhere within Ω , except for very thin boundary near $\partial\Omega$. Therefore, one may write

$$\tau(\xi, y) = \tau_p f(\xi, y), \quad (3.52)$$

where the so-called “form function” $f(\xi, y)$ satisfies the following conditions

$$f(\xi, y) = 1 \quad [\xi, y] \in \Omega - \partial\Omega \quad (3.53)$$

$$f(\xi, y) \approx 0 \quad [\xi, y] \in \partial\Omega.$$

Multiplying Eq. (3.49) with the stationary probability in Eq. (3.35) and integrating over $\Omega - \partial\Omega$, one obtains by use of the Gaussian theorem and Eq. (3.52) [63, 64])

$$\tau_p = - \frac{\int_{\Omega - \partial\Omega} p_s(\xi, y) d\xi dy}{\varepsilon \int_{\partial\Omega} p_s(\xi, y) \left[\chi(y) \frac{\partial f(\xi, y)}{\partial y} + \gamma \zeta(y) \frac{\partial f(\xi, y)}{\partial \xi} \right] \cdot d\mathbf{n}}, \quad (3.54)$$

where $d\mathbf{n}$ denotes the outward normal to the boundary $\partial\Omega$. So now the asymptotic mean first-passage time is expressed in terms of the stationary distribution $p_s(\xi, y)$ and of the gradient of form function $f(\xi, y)$ on $\partial\Omega$. As of the form function, plugging Eq. (3.52) into Eq. (3.49) and since $\tau_p \sim e^{1/\varepsilon}$ [58, 65] for the weak-noise limit neglect the inhomogeneity and write

$$L^+ f(\xi, y) = 0, \quad (3.55)$$

with the matching conditions as stated in Eq. (3.53). Indeed, Eq. (3.54) is a valid expression for the mean first-passage time irrespective of whether Ω is an attractive domain and whether the noise is weak. However, only in these latter cases will the mean first-passage time be essentially independent of the starting point, and the precise location of the source will not matter. Thus, solving Eq. (3.54) only requires evaluation of the volume and the line integrals in the equation and solving Eq. (3.55) for the form function $f(\xi, y)$.

For weak noise, the sharply-peaked stationary probability density at the stable stationary points of the drift field allows one to evaluate both integrals in Eq. (3.54) in Gaussian approximations. The volume integral in the numerator in Eq. (3.54) is dominated by the linear neighborhood of the energy minimum $[\xi_A, y_A]$, and yields in leading order in noise strength ε

$$P_A = \int_{\Omega - \partial\Omega} p_s(\xi, y) d\xi dy \quad (3.56)$$

$$\simeq \mathbb{N}^{-1} \exp(-\alpha_A/\varepsilon) \left[\det \frac{\alpha_{ij}^A}{2\pi\varepsilon} \right]^{-1/2}, \quad (3.57)$$

where P_A is the probability of the particle being in the linear neighborhood of the secondary energy minimum; the quantities α_A and the matrix α_{ij}^A are determined by

local quadratic expansion of $\alpha(\xi, y)$ in the vicinity of $[\xi_A, y_A]$, namely

$$\alpha(\xi_A + \delta\xi, y_A + \delta y) = \alpha_A + \frac{1}{2}\alpha_{ij}^A \delta\xi \delta y + O((\xi, y)^3), \quad (3.58)$$

with

$$\alpha_A = \frac{\phi(y_A)}{\Delta A} - \varepsilon N \ln [1 + K_{eq}(y_A)], \quad (3.59)$$

$$\alpha_{ij}^A = \begin{bmatrix} \frac{\partial^2 \alpha(\xi, y)}{\partial \xi^2} \bigg|_{\xi_A, y_A} & \frac{\partial^2 \alpha(\xi, y)}{\partial \xi \partial y} \bigg|_{\xi_A, y_A} \\ \frac{\partial^2 \alpha(\xi, y)}{\partial \xi \partial y} \bigg|_{\xi_A, y_A} & \frac{\partial^2 \alpha(\xi, y)}{\partial y^2} \bigg|_{\xi_A, y_A} \end{bmatrix}. \quad (3.60)$$

Clearly, if the 2^o potential well dynamics of the particle can not be assumed as parabolic, the population within domain Ω differs from the Gaussian approximation in Eq. (3.57). For instance, for many cases of the attachment of a particle to a surface from colloidal suspensions, the particle experiences the conventional colloidal interactions, which cannot be assumed quadratic, even at low noise limit. However, the actual population within domain Ω can be corrected by a prefactor for P_A which now assumes a temperature dependence. For example, suppose we approximate the colloidal potential with a polynomial around the secondary minimum:

$$\phi(z) = \alpha_A + a_1(z - z_m) + a_2(z - z_m)^2 + a_3(z - z_m)^3 + a_4(z - z_m)^4. \quad (3.61)$$

If we denote the integral in the numerator of Eq. (3.54) for such suspension cases as P_A^{CS} , we find the correction

$$P_A^{CS} \simeq \sqrt{\frac{\det \alpha_{ij}^A}{2\varepsilon}} \frac{\Gamma(\frac{1}{3}) \Gamma(\frac{1}{4})}{12l^4 a_1 \sqrt{a_2} \sqrt[3]{a_3} \sqrt[4]{a_4}} \varepsilon^{25/12} (e^{-a_1 z_m/\varepsilon} - e^{-a_1 z_s/\varepsilon}) P_A. \quad (3.62)$$

Essentially, the treatment of the saddle point is the same as that of the potential well except that at the saddle there is only one unstable direction whose corresponding eigenvalue of matrix α_{ij}^S is negative. Hence, the stationary probability in the denominator of Eq. (3.54) is given by making quadratic approximation of $\alpha(\xi, y)$ in the linear neighborhood of the saddle point $[\xi_S = 0, y_S]$:

$$P_S \simeq N^{-1} \exp(-\alpha_S/\varepsilon) \left| \det \frac{\alpha_{ij}^S}{2\pi\varepsilon} \right|^{-1/2}, \quad (3.63)$$

where

$$\alpha(\xi_s + \delta\xi, y_s + \delta y) = \alpha_s + \frac{1}{2} \alpha_{ij}^s \delta\xi \delta y + O((\xi, y)^3), \quad (3.64)$$

$$\alpha_s = \frac{\phi(y_s)}{\Delta A} - \varepsilon N \ln [1 + K_{eq}(y_s)], \quad (3.65)$$

and

$$\alpha_{ij}^s = \begin{bmatrix} \frac{\partial^2 \alpha(\xi, y)}{\partial \xi^2} \Big|_{\xi_s, y_s} & \frac{\partial^2 \alpha(\xi, y)}{\partial \xi \partial y} \Big|_{\xi_s, y_s} \\ \frac{\partial^2 \alpha(\xi, y)}{\partial \xi \partial y} \Big|_{\xi_s, y_s} & \frac{\partial^2 \alpha(\xi, y)}{\partial y^2} \Big|_{\xi_s, y_s} \end{bmatrix}. \quad (3.66)$$

In order to determine the gradient of the form function $f(\xi, y)$, one chooses the following ansatz which already satisfies the conditions in Eq. (3.53) [66, 67, 68]

$$f(\xi, y) = \sqrt{2/\pi\varepsilon} \int_0^{\rho(\xi, y)} e^{-u^2/\varepsilon} du. \quad (3.67)$$

From Eqs. (3.50) and (3.55) one obtains in leading order in noise strength ε a first-order partial differential equation for $\rho(\xi, y)$:

$$\chi(y) \frac{\partial \alpha(\xi, y)}{\partial y} \frac{\partial \rho}{\partial y} + \gamma \zeta(y) \frac{\partial \beta(\xi, y)}{\partial \xi} \frac{\partial \rho}{\partial \xi} - \left[\varepsilon \chi(y) \left(\frac{\partial \rho}{\partial y} \right)^2 + \varepsilon \gamma \zeta(y) \left(\frac{\partial \rho}{\partial \xi} \right)^2 \right] \rho = 0. \quad (3.68)$$

In the vicinity of the saddle that contributes significantly to the integral in the denominator in Eq. (3.54), one finds that the solution of Eq. (3.68) is

$$\rho = (D_{rr}/\lambda_+)^{-1/2} r, \quad (3.69)$$

where r is the unstable direction of the drift field at the saddle point, D_{rr} is the diffusion matrix in this unstable direction, and λ_+ is the positive eigenvalue of

$$\begin{bmatrix} -\frac{\partial^2 \alpha(\xi, y)}{\partial y^2} \Big|_{\xi_s, y_s} & -\frac{\partial^2 \alpha(\xi, y)}{\partial \xi \partial y} \Big|_{\xi_s, y_s} \\ -\gamma \frac{\partial^2 \beta(\xi, y)}{\partial \xi \partial y} \Big|_{\xi_s, y_s} & -\gamma \frac{\partial^2 \beta(\xi, y)}{\partial \xi^2} \Big|_{\xi_s, y_s} \end{bmatrix} \begin{bmatrix} y \\ \xi \end{bmatrix} = \lambda \pm \begin{bmatrix} y \\ \xi \end{bmatrix}. \quad (3.70)$$

Combining Eqs. (3.67) and (3.69) one gets for the line integral in Eq. (3.54) [63]

$$\int_{\partial\Omega} p_s(\xi, y) \left[\chi(y) \frac{\partial f(\xi, y)}{\partial y} + \gamma \zeta(y) \frac{\partial f(\xi, y)}{\partial \xi} \right] \cdot d\mathbf{n} \simeq -\lambda_+ P_s / (\pi\varepsilon). \quad (3.71)$$

Hence, from Eqs. (3.54), (3.57), (3.63) and (3.71), the final result for the dimensionless MFPT is

$$\tau_p = \frac{\pi}{\lambda_+} (P_A/P_S) \quad (3.72)$$

$$= \frac{\pi}{\lambda_+} \left[\frac{|\det \alpha_{ij}^S|}{\det \alpha_{ij}^A} \right]^{1/2} e^{(\alpha_S - \alpha_A)/\varepsilon}, \quad (3.73)$$

where

$$\lambda_+ = \frac{-(\gamma d + a) + \sqrt{(\gamma d - a)^2 + 4\gamma bc}}{2}, \quad (3.74)$$

with

$$a = \frac{\partial^2 \alpha(\xi, y)}{\partial y^2} \Big|_{\xi_s, y_s}, \quad (3.75)$$

$$b = \frac{\partial^2 \alpha(\xi, y)}{\partial \xi \partial y} \Big|_{\xi_s, y_s}, \quad (3.76)$$

$$c = \frac{\partial^2 \beta(\xi, y)}{\partial \xi \partial y} \Big|_{\xi_s, y_s}, \quad (3.77)$$

and

$$d = \frac{\partial^2 \beta(\xi, y)}{\partial \xi^2} \Big|_{\xi_s, y_s}. \quad (3.78)$$

Switching back to the time scale using Eq. (3.47), one obtains for the actual mean first-passage time

$$T_p = \frac{l^2 k_B T}{D(z_s) \Delta A} \tau_p. \quad (3.79)$$

Since at the top of the saddle point the particle has equal probability of going to either side [69], the attachment rate constant, k , of the particle to a surface will be given by

$$k = \frac{1}{2T_p} = \frac{D(z_s) \Delta A}{l^2 k_B T} \frac{\lambda_+ P_S}{2\pi P_A}. \quad (3.80)$$

Therefore, the rate obtained here is governed by the deterministic dynamics of the particle at the saddle, stretched by the relative frequency of finding the particle at the saddle compared to at the potential well.

Derivation of Deposition Rate Constant

In this section, we shall relate the particle attachment rate constant, k , with the deposition rate constant of the particle, k_+ , which shares much broader applications. Suppose the probability of a particle being at the onset of the diffusion boundary layer, as shown in Figure 3.1 (a), is $P(L) \propto e^{-A(\xi_L, y_L)/k_B T}$, the deposition rate constant of the particle is defined as the probability flux over the saddle barrier, j , divided by $P(L)$ in the steady state:

$$k_+ = \frac{j}{P(L)}. \quad (3.81)$$

When examining Eqs. (3.54) and (3.80) for k , one finds out that k is actually the ratio of the flux crossing over the energy barrier to the probability of the particle being within the potential well region, namely

$$k = \frac{j}{P_A}. \quad (3.82)$$

Combination of Eqs. (3.81) and (3.82) together yields

$$k_+ = k \frac{P_A}{P(L)} = \frac{D(z_s) \Delta A}{l^2 k_B T} \frac{\lambda_+ P_S}{2\pi P(L)}. \quad (3.83)$$

From this equation, one sees that the deposition rate constant is governed by the deterministic dynamics of the particle at the saddle, stretched by the relative frequency of finding the particle at the saddle compared to at the source which is located at the startpoint of the diffusive boundary layer, and that k_+ is independent of the actual shape and location of the secondary energy minimum.

3.4 Results and Discussions

Quantitative predictions require the functional forms for the forward and reverse rate constants, $k_f(z)$ and $k_r(z)$ respectively. Here, we adopt the dynamic models proposed by Dembo *et al.* [26] for the strain dependence of the transition state energy between the bound and free states. The functional forms of the rate

constants with respect to z are

$$k_r(z) = k_{r0} \exp \left[\frac{\Delta \gamma_b}{k_B T} (z - z_0) \right], \quad (3.84)$$

$$k_f(z) = k_{f0} \exp \left[\frac{\Delta \gamma_b}{k_B T} (z - z_0) \right] \exp \left[-\frac{\gamma_b}{2k_B T} (z - z_0)^2 \right], \quad (3.85)$$

where $k_{r0} = k_{f0} \exp(\epsilon_0/k_B T)$ and Δ is the bond length at the transition state. As one can see, combination of these two equations yields back to Eq. (2.2).

Using the parameter values assumed in Table 3.1, we show some general prediction results, and also compare the mean first-passage times obtained using the MFPT formalism (*i.e.*, Eq. (3.79)) with those by the numerical method, Eq. (3.18), and demonstrate their dependency on the binding parameters as well. In Figure 3.3, T is plotted as a function of k_{f0} at fixed $K_{eq}(z_0) \equiv k_{f0}/k_{r0}$. One can see that the mean first-passage time, T , decreases linearly with the forward binding rate constant, k_{f0} , for slower binding, but becomes independent of k_{f0} for faster binding compared to the rate of the particle diffusion near the surface. Two rate-limiting regimes are observed from this plot. One is binding-rate-limited. In this regime, a particle may approach to a distance very close to the surface where binding is energetically favored, but the binding reaction is too slow to allow attachment. The particle actually feels repulsive surface forces and fluctuates away from the surface by Brownian motions. The other one is diffusion-rate-limited. In this regime, binding is fast such that binding reaction can be assumed always near equilibrium. Thus, the attachment really depends on how fast a particle can diffuse over the energy barrier to become attached, which is similar to the case of particle deposition without macromolecular binding in Ref. [14]. Therefore, not only the affinity but also the kinetic rate constants play an important role in determining particle attachment. For the intermediate case where both Brownian motions and binding processes are similarly fast, our analytical approximations given by Eq. (3.79) predict smooth transition between these two limiting regimes. Also, the results from the two methods are consistent with each other.

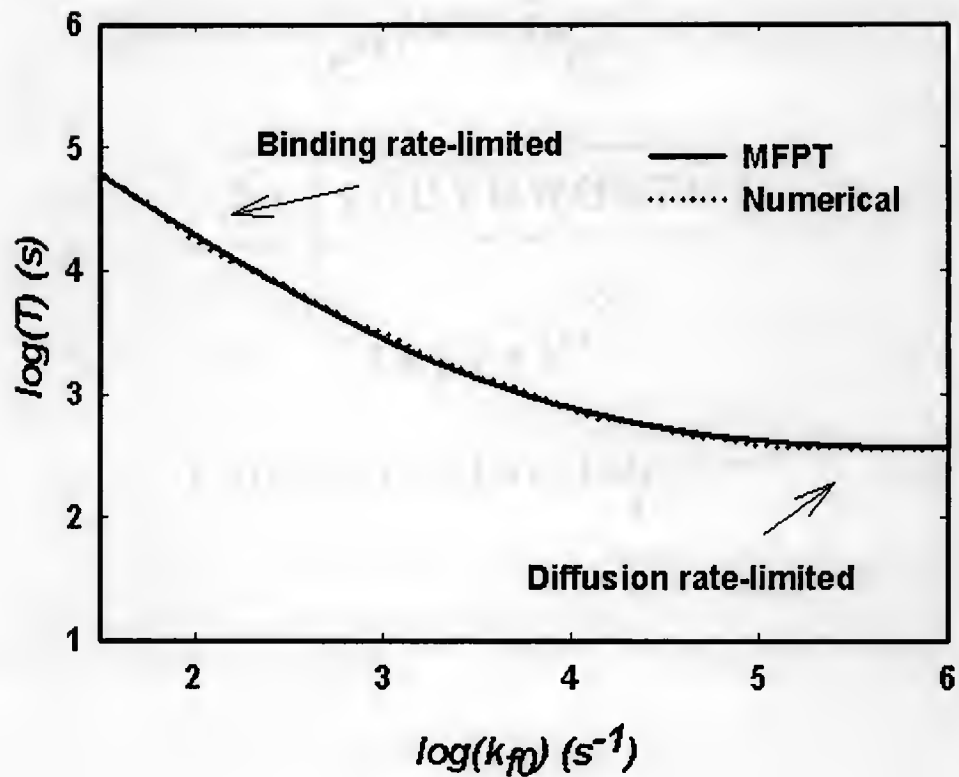


Figure 3.3: A plot of the mean first-passage time, T , vs. the forward binding rate constant, k_{f0} , at fixed $K_{eq}(z_0)$. As the plot shows, T decreases linearly with k_{f0} for slower binding, but becomes independent of k_{f0} for faster binding. The solid line is from MFPT approach and the dotted line from numerical method. The MFPT approach is a good analytical approximation for the corresponding numerical approach.

In Figures 3.4-3.7, the mean first-passage time, T , is plotted versus the energy barrier height, ΔA , which is varied by altering the baseline repulsive potential, ϕ_0 , for the case of the imposed trapping potential in Figure 3.4, and by adjusting the coefficient, a_3 , in the case of particle attachment from the colloidal suspensions in Eq. (3.61) in Figure 3.6. In both MFPT and numerical methods, $\ln(T)$ increases linearly with ΔA with slope of 1, indicating the mean first-passage time is exponentially dependent on the height of a sufficiently sharply peaked energy barrier. In both plots, the results from two methods match very well except that at lower ΔA some discrepancies occur. These discrepancies are partly due to the fact that the free energies at the saddle as well as in the secondary minimum spread out and become less sharply distributed with declining energy barrier, as demonstrated in Figures 3.5 and 3.7, respectively; hence, the Gaussian approximations as treated in the MFPT approach in the neighborhoods of these spots start to show their drawbacks. Furthermore, the number of bonds that could be formed near the saddle region becomes less and less with decreasing ΔA , so the discrete nature of bonds grows more and more significant and should be considered rather than the continuous approximation in the MFPT treatment. From here, one can also see that the mean first-passage time approach can be essentially applied for any reasonable function $\phi(z)$.

Next, we shall examine the dependence of T on the properties of binding macromolecules. For illustration purpose, Eq. (3.5) is used for $\phi(z)$. In Figures 3.8-3.13, T is plotted versus various binding parameters such as unstrained bond length z_0 in Figure 3.8, bond stiffness γ_b in Figure 3.10 and the number of macromolecules available for binding, N , in Figure 3.12. As the plots show, T decreases greatly with bond length, increases dramatically with bond stiffness, while the availability of binding molecules at the interface tends to decrease T . From the equilibrium energy distance profiles shown in Figure 3.9, one can see that increasing bond lengths lead to the decrease in the height of energy barrier, which, as a result, decreases T as

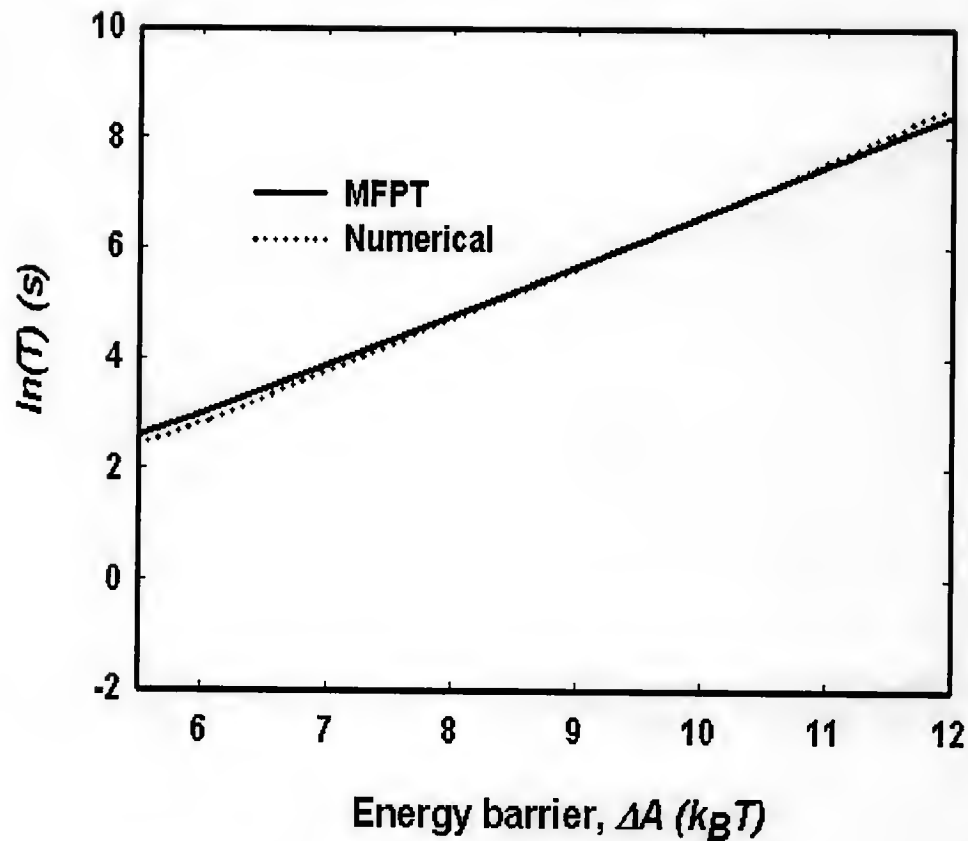


Figure 3.4: The mean first-passage time, T , is plotted against the energy barrier at the saddle point, ΔA , which is varied by varying the baseline repulsive potential, ϕ_0 . The solid lines are from the MFPT approach, Eq. (3.79) and the dotted lines from numerical solutions, Eq. (3.18).

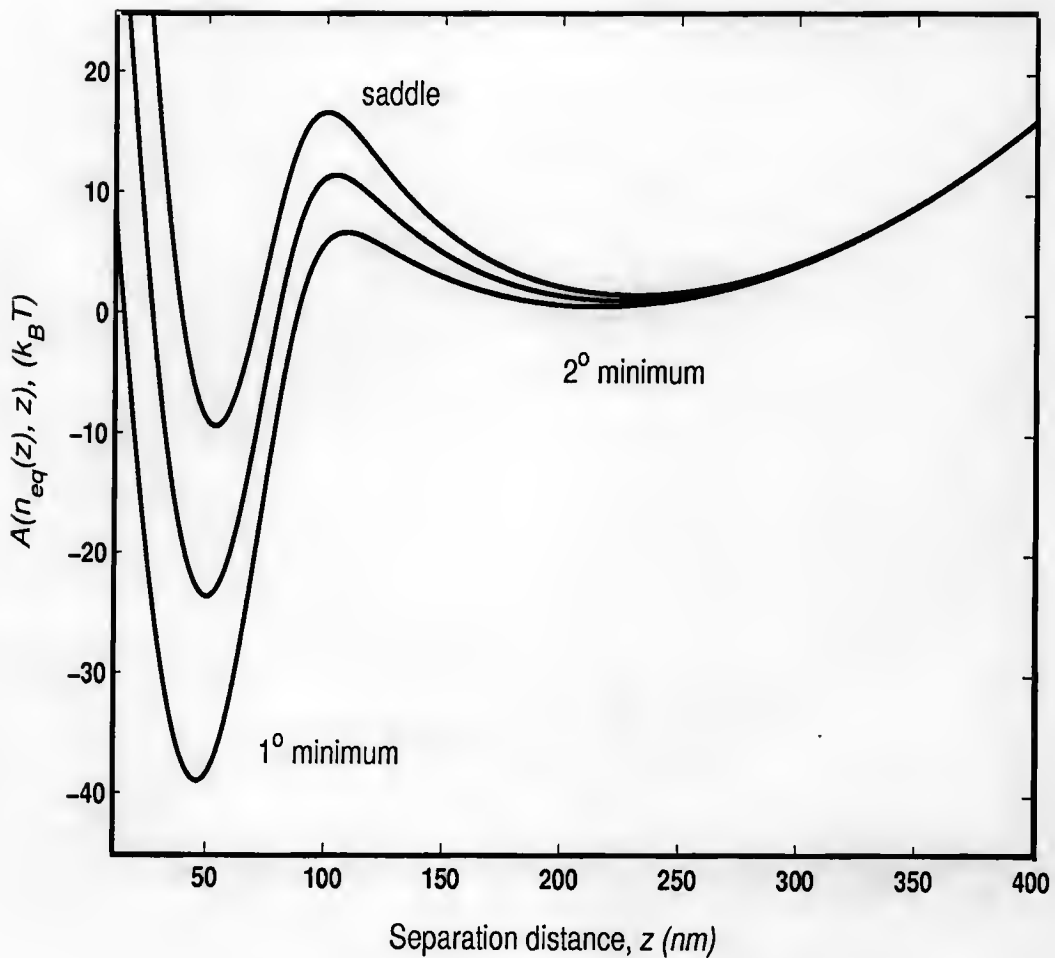


Figure 3.5: This plot shows the minimal energy paths, $A(n_{eq}(z), z)$, for different ϕ_0 in Figure 3.4. The lesser Gaussian distributions of the free energies at the saddle and/or the secondary minimum for lower ΔA account for the discrepancies in MFPT and numerical methods.

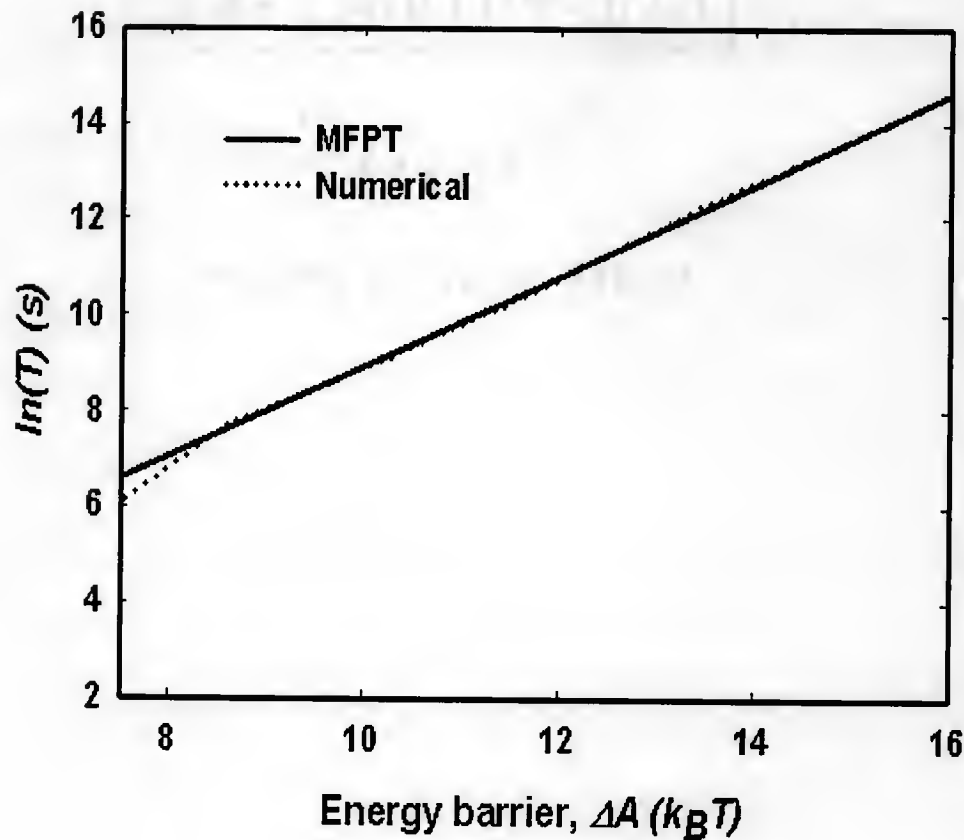


Figure 3.6: The mean first-passage time, T , is plotted against the energy barrier at the saddle point, ΔA , which is varied by adjusting the coefficient a_3 for the particle attachment from colloidal suspensions. The solid lines are from the MFPT approach, Eq. (3.79) and the dotted lines from numerical solutions, Eq. (3.18).

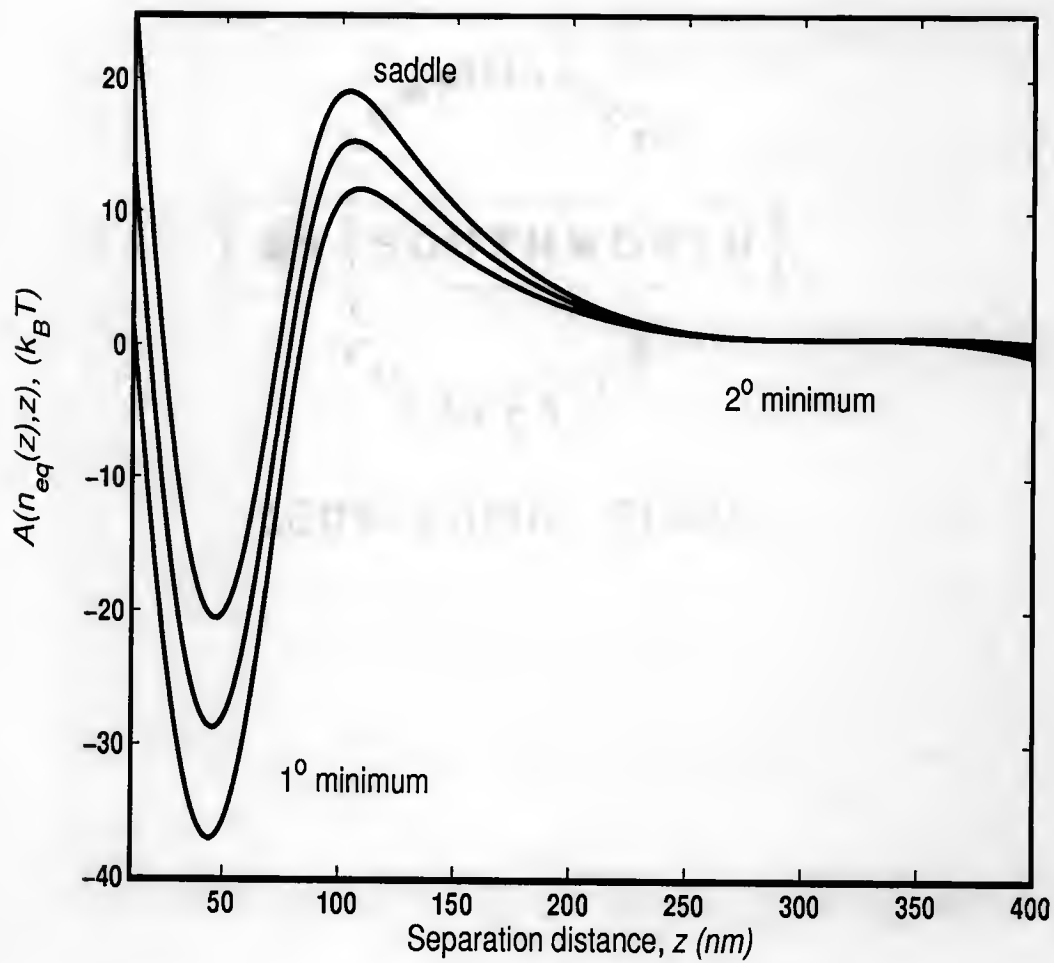


Figure 3.7: This plot shows the minimal energy paths, $A(n_{eq}(z), z)$, for different a_3 in Figure 3.6. The lesser Gaussian distributions of the free energies at the saddle and/or the secondary minimum for lower ΔA account for the discrepancies in MFPT and numerical methods.

displayed in Figures 3.4 and 3.6; also, larger bond lengths shift the primary energy wells away from the surface, which helps for the binding molecules to extend over the energy barrier to become attached. Similarly, if the stiffness of bond increases, the energy barrier increases too, as shown in Figure 3.11; thus, stiffer or less flexible binding molecules are less easier to climb over the energy barrier to attach. When the number of binding molecules in the contact area is increased, the height of energy barrier is only slightly decreased, so T decreases slightly too, though the depth of primary energy minimum drops considerably, see Figure 3.13. From here, one can clearly conclude that it is the height of the energy barrier at the saddle transition state that governs the overall attachment rate of particles to a surface. In all the plots shown here, the MFPT method is in excellent agreement with the numerical solutions. Only when N becomes much smaller, does the continuous treatment of the discrete bonds in MFPT approach start to break up, thus deviations between the two methods begin showing up.

The mean first passage time, T , is also plotted as a function of unstressed bond energy, ϵ_0 , in Figure 3.14. T increases monotonically with ϵ_0 . This can also be explained by the increasing energy barrier with the increasing bond energy, shown in Figure 3.15. ϵ_0 is directly related to the affinity of bonds through $K_{eq}^0 = \exp(-\epsilon_0/k_B T)$. As this plot shows, if the bond energy is very high, corresponding to low affinity, then attachment is not thermodynamically favorable. So, lower bond energy serves to lower the effective energy barrier to attachment.

The effect of particle size on attachment is examined as well. Since we have assumed a uniform contact area between the particle and the surface, and this contact region remains unchanged during attachment, the change in particle radius would not alter the overall particle-surface interaction energy, as long as all the other binding parameters including number of binding molecules within the contact area are fixed. When T is plotted versus particle radius, R , one finds out that T increases slightly

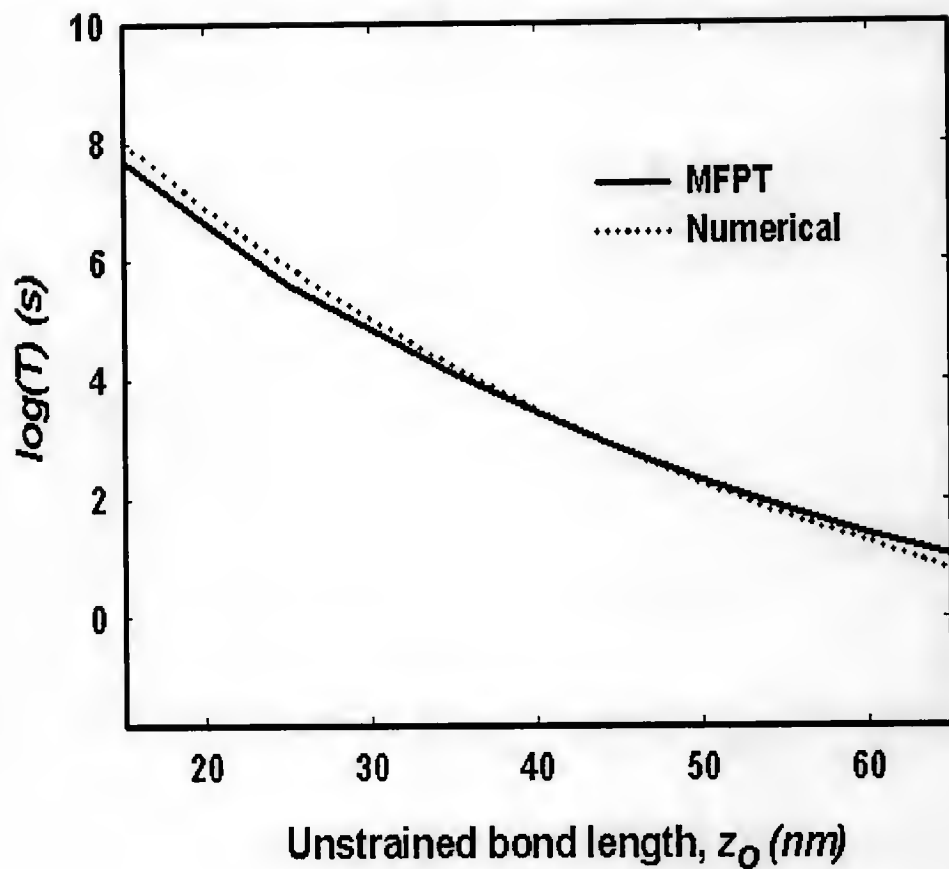


Figure 3.8: The mean first-passage time, T , is plotted against unstrained bond length, z_0 . In the plot, the solid line is from MFPT approach and the dotted line from numerical method. As the plot shows, longer bond length allows the molecules to cross the energy barrier to attach the surface, thus to decrease T .

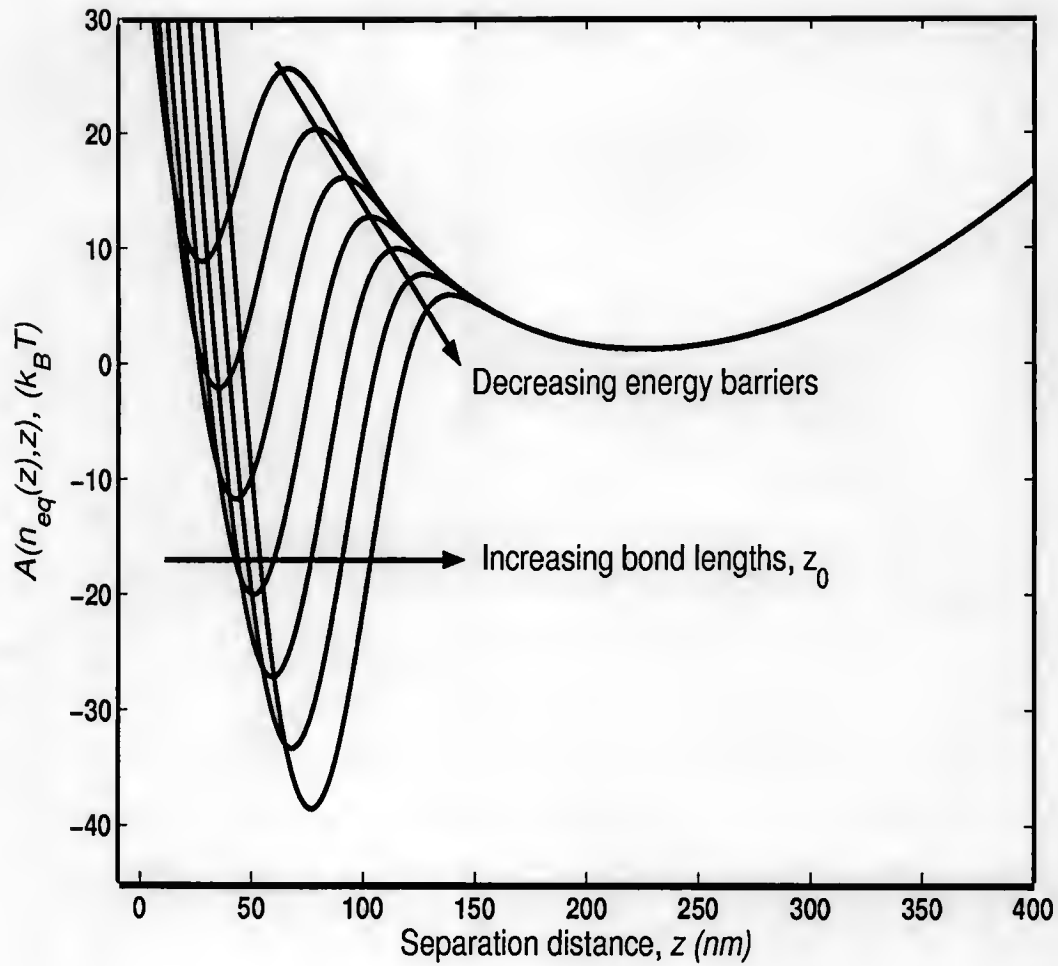


Figure 3.9: This plot shows the minimal energy paths, $A(n_{eq}(z), z)$, for different unstrained bond length, z_0 , in Figure 3.8. The energy barrier at the saddle point decreases as the unstrained bond length increases.

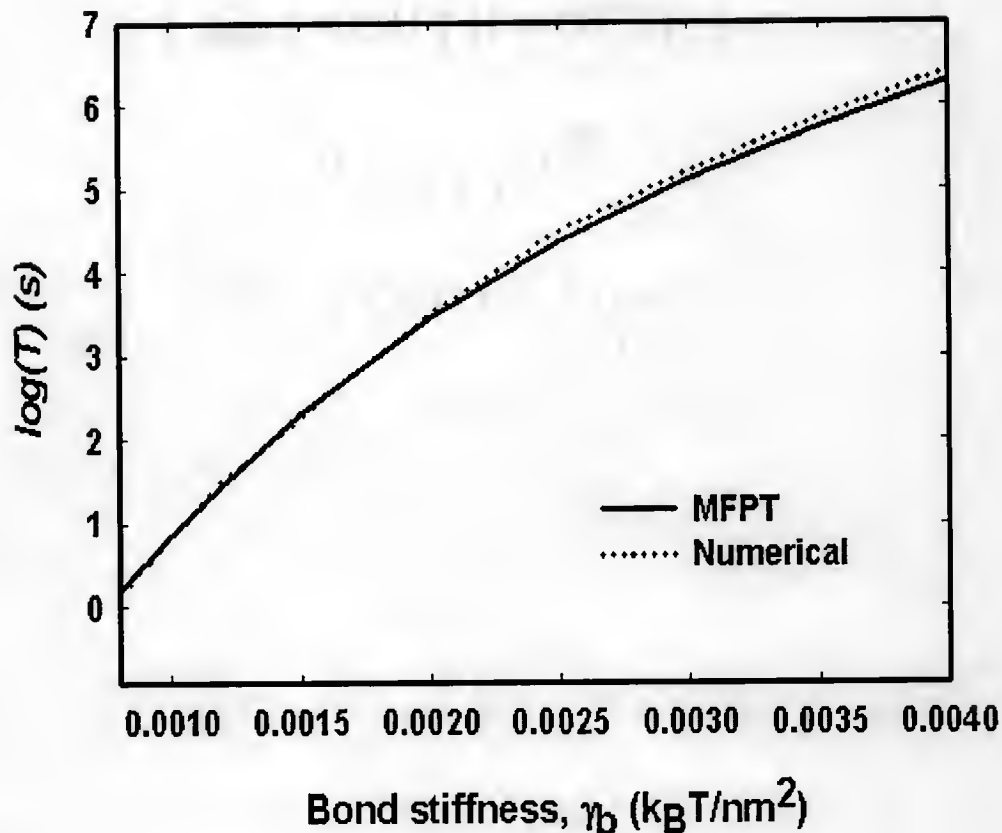


Figure 3.10: The mean first-passage time, T , is plotted as a function of bond stiffness, γ_b . In the plot, the solid line is from MFPT approach and the dotted line from numerical method. As the plot shows, lower bond stiffness allows the binding molecules to cross the energy barrier to attach the surface, thus to decrease T .

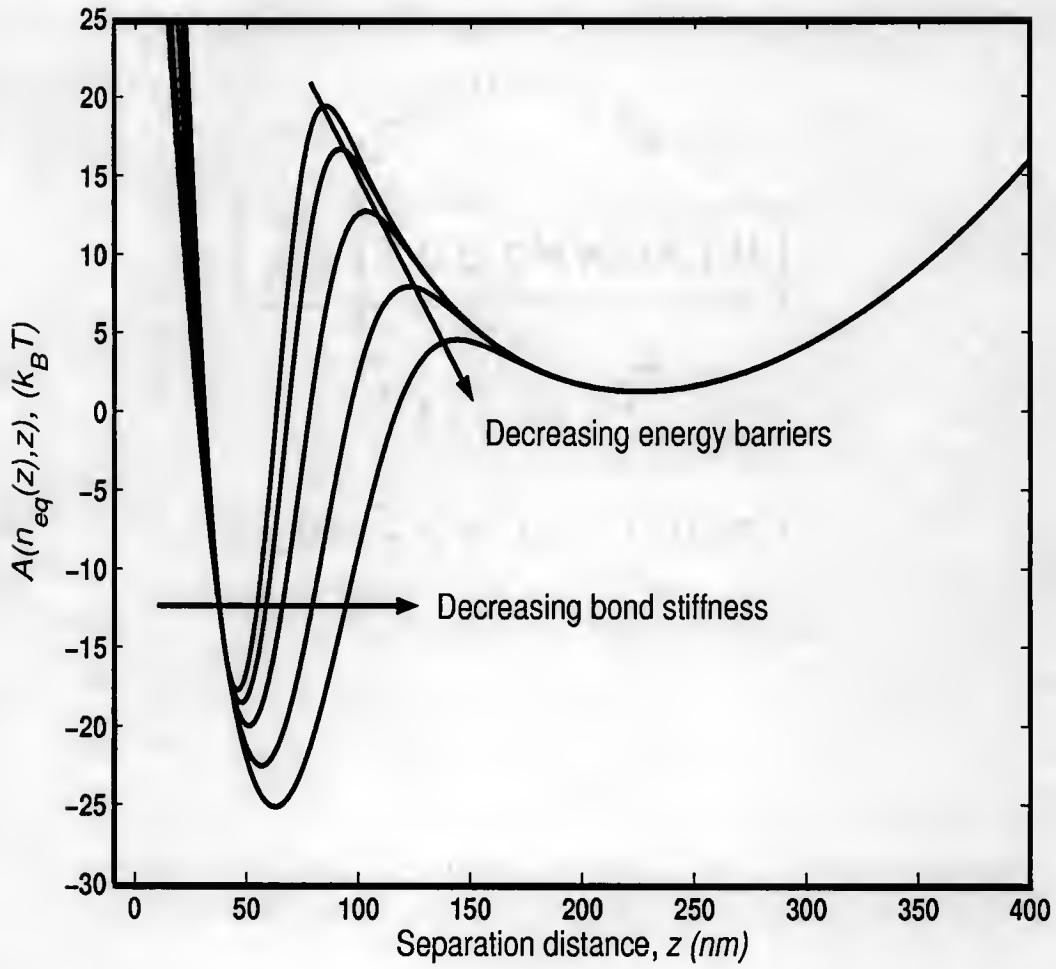


Figure 3.11: This plot shows the minimal energy paths, $A(n_{eq}(z), z)$, for different bond stiffness γ_b in Figure 3.10. The energy barrier at the saddle point decreases with decreasing bond stiffness.

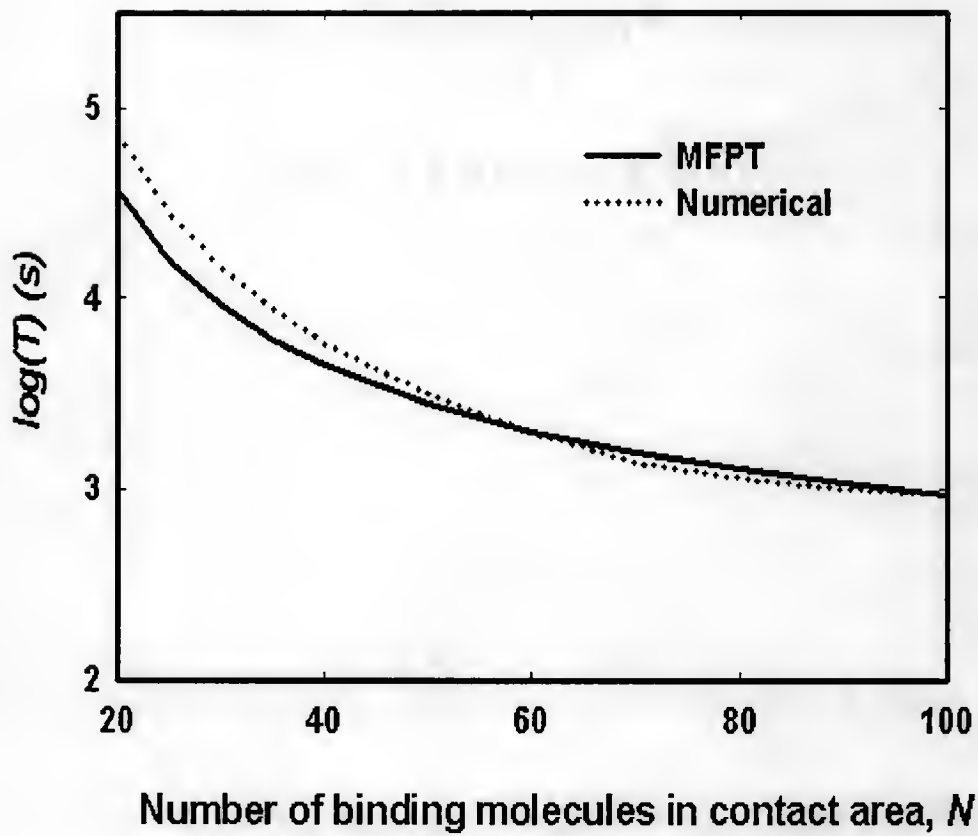


Figure 3.12: The mean first-passage time, T , is plotted vs. the number of binding molecules available in the contact area, N . In the plot, the solid line is from MFPT approach and the dotted line from numerical method. As the plot shows, larger number of binding macromolecules tends to increase probability of particle attachment to the surface, thus to decrease T .

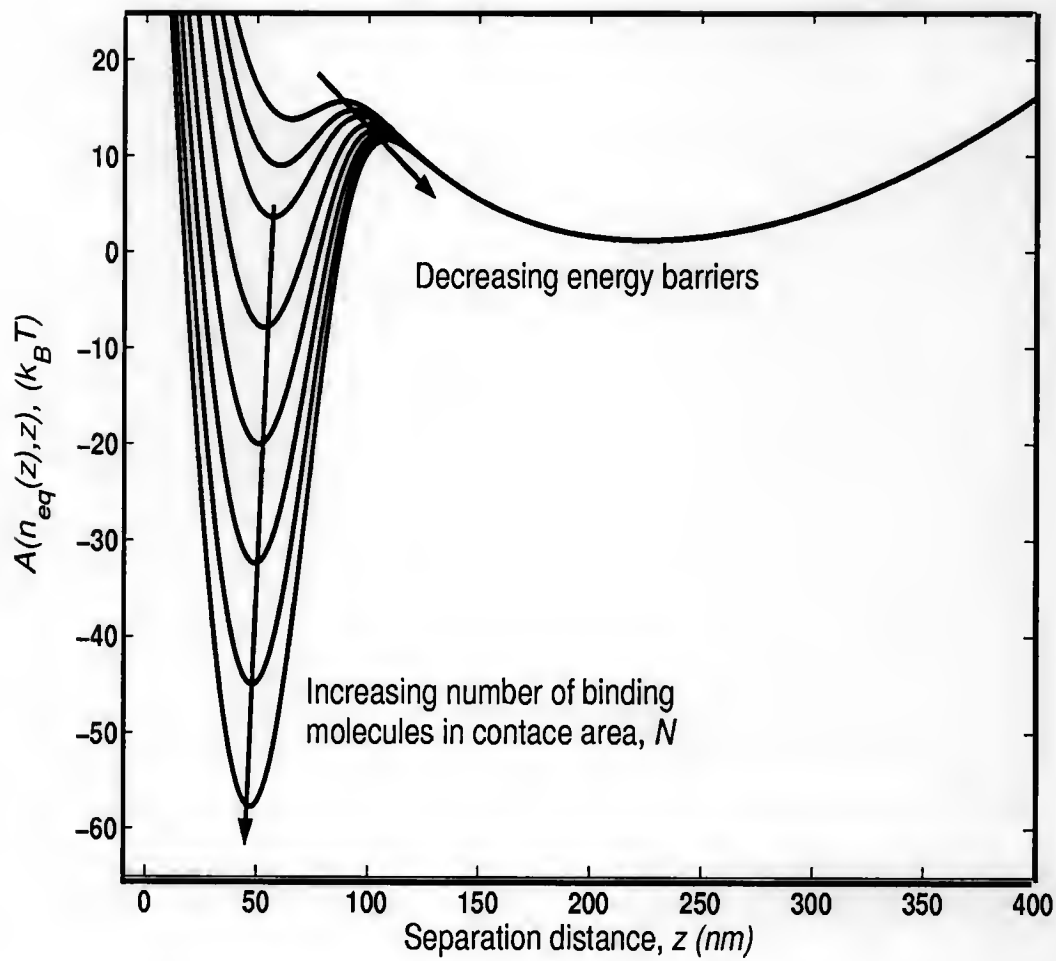


Figure 3.13: This plot shows the minimal energy paths, $A(n_{eq}(z), z)$, for different number of binding molecules in the contact area as shown in Figure 3.13. The energy barrier at the saddle point decreases with increasing N .

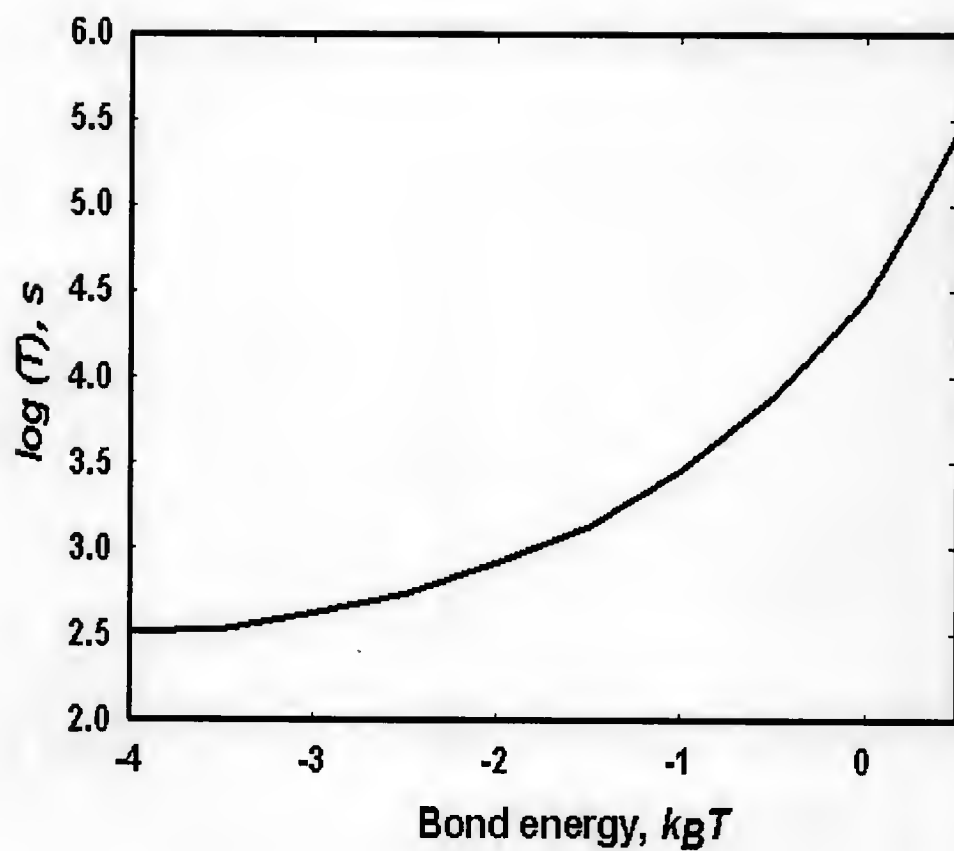


Figure 3.14: The mean first-passage time is plotted as a function of unstressed bond energy.

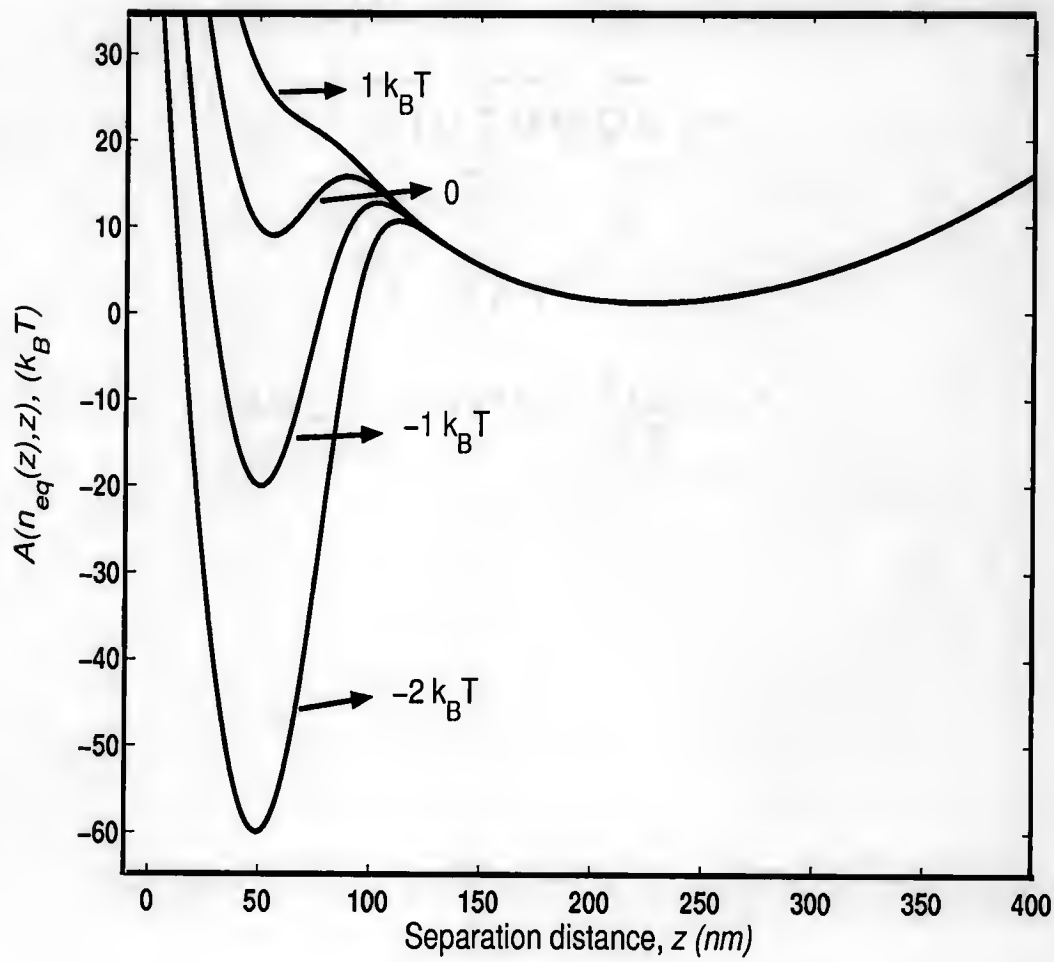


Figure 3.15: The minimal energy path, $A(n_{eq}(z), z)$, is plotted for different values of the unstressed bond energy, e_0 as shown in Figure 3.14. Lower bond energy tends to lower the effective energy barrier to attachment.

with R in Figure 3.16. This could be due to the slower Brownian motions for larger size of particles. The diffusion process for larger particles slows down, which would increase the time needed for attachment. In fact, the assumption of a flat and uniform contact area between the particle and the surface is an oversimplification of the actual reacting system, especially for a rigid particle where surface deformation is not easy. From our intuition, the distribution of binding molecules over the curved particle surface would have an effect on the interaction energy, and thus the attachment rate. This aspect will be further described in Chapter 5.

The deposition rate constant, k_+ , is plotted as a function of the forward binding rate constant, k_{f0} in Figure 3.17 at varied energy barriers at the saddle point using the mean first-passage time approach. The energy barrier ΔA is varied by altering the value of the coefficient a_3 in Eq. (3.61). In all the plots shown here, k_+ increases linearly with k_{f0} at slower binding (*i.e.*, the binding rate-limiting regime), but becomes independent of k_{f0} at faster binding (*i.e.*, the diffusion rate-limiting regime). The intermediate region where both binding and diffusion are similarly fast can be also approximated analytically from MFPT approach. Once again, the plots show that k_+ increases with decreasing ΔA .

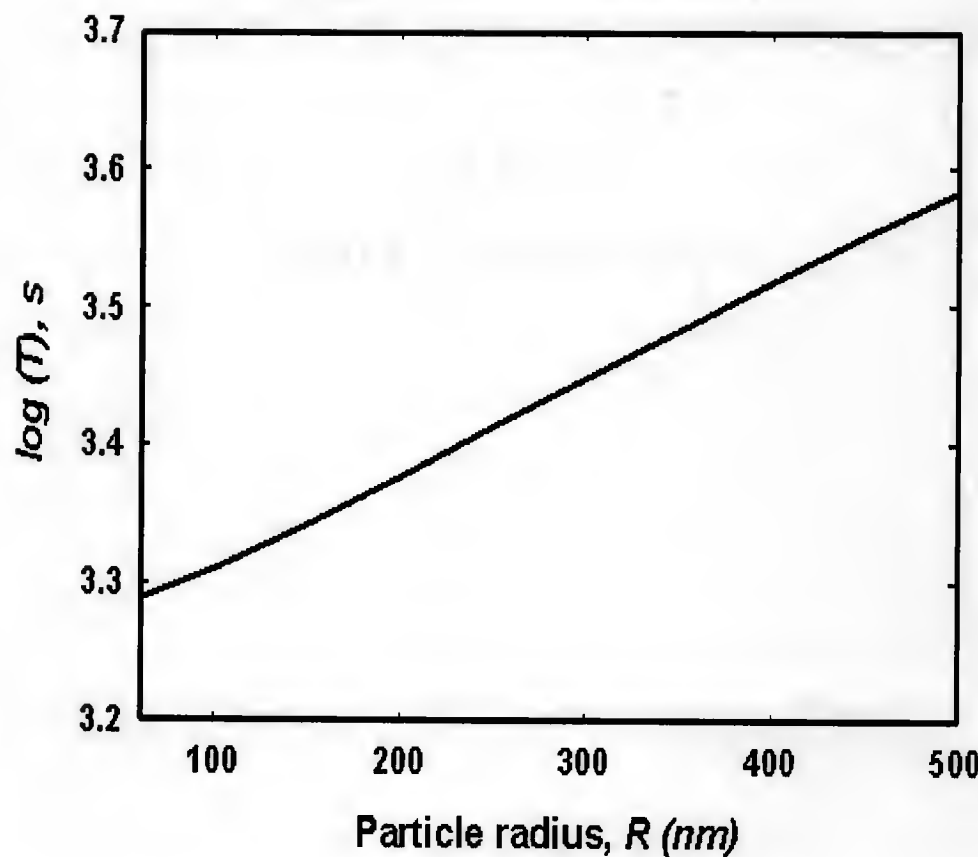


Figure 3.16: The mean first-passage time, T , is plotted as a function of particle radius, R . As the plot shows, T increases with particle size, though the equilibrium energy barrier at the saddle transition state remains unchanged based on the uniform contact area assumption. Longer time is needed to attachment for larger particle as a result of slowing down of particle diffusion over the energy barrier.

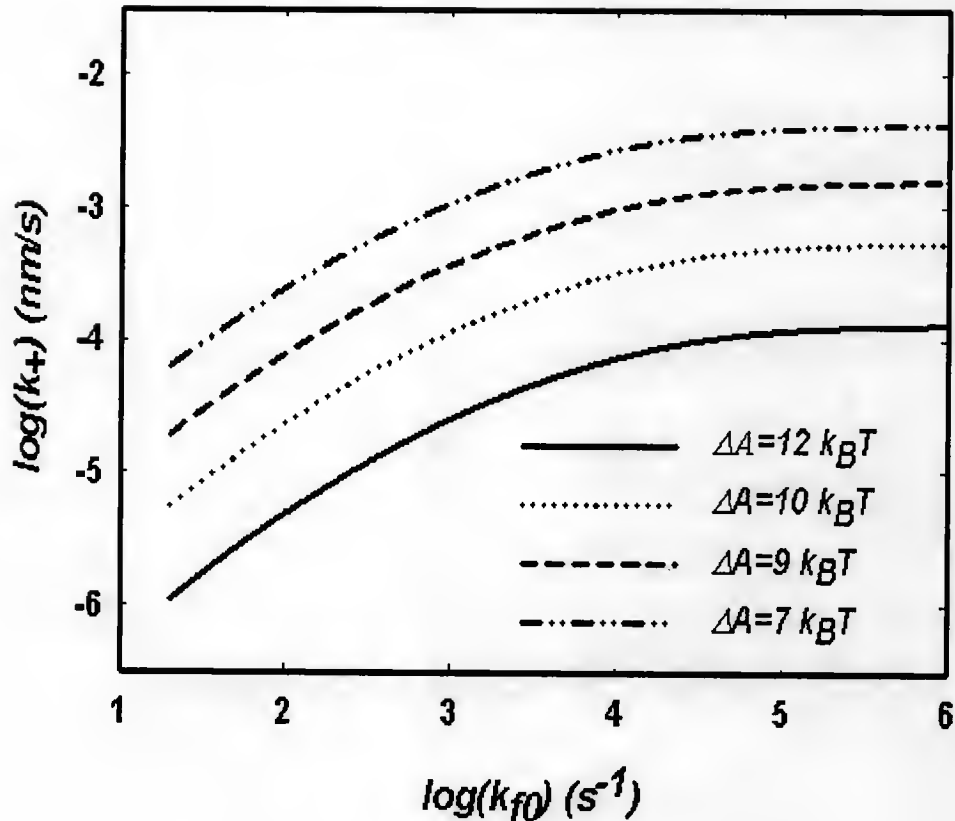


Figure 3.17: The deposition rate constant, k_+ , is plotted as a function of the forward binding rate constant, k_{f0} , at different energy barrier height which is varied by varying the coefficient a_3 in Eq. (3.61). The results shown here are from the mean first-passage time method. In all the plots, k_+ increases linearly with k_{f0} at binding rate-limiting regime, but reaches a plateau and becomes independent of k_{f0} at diffusion rate-limiting regime. One can also see that the higher the energy barrier, the lower the deposition rate constant becomes. The following symbols were used: solid line – $\Delta A = 12k_B T$; dotted line – $\Delta A = 10k_B T$; broken line – $\Delta A = 9k_B T$; dash-dotted line – $\Delta A = 7k_B T$.

CHAPTER 4

APPLICATION IN ATTACHMENT OF *S. AUREUS* TO FIBRINOGEN COATED SURFACES

In previous chapter, we have developed a dynamical model to estimate the attachment rate constant of particles to a surface analytically as well as numerically. Also in that chapter, we used the parameter values assumed in Table 3.1 to illustrate how to predict the attachment rate constant (or, time to attachment). The model prediction results from both analytical approximations and numerical computations are consistent with each other, and also agree qualitatively with the findings in Ref. [38]. Further evaluations of this model require modeling real biological adhesion systems. In this chapter, we shall use parameter values (either measured experimentally or estimated from other reasonable models) to predict the deposition rate constants of *Staphylococcus aureus* to fibrinogen-coated surfaces from our dynamic model, then compare model prediction results with experimental measurement data obtained from our research group.

4.1 *Staphylococcus aureus*: Structure and Characteristics

Staphylococcus aureus (*S. aureus*) is a highly pathogenic bacterial strain that causes nearly half of hospital-acquired infections and is involved in many device-centered infections. In addition, it becomes more resistant to many types of antibiotic treatments, so prevention of infection from it becomes even more crucial.

S. aureus is a nearly spherical, gram-positive bacterium with diameter ranging from $0.7 \sim 1.2 \mu\text{m}$, with its SEM images shown in Figure 4.1(a). On its surface, *S. aureus* expresses a family of specific protein adhesins (termed MSCRAMMs, microbial

surface components recognizing adhesive matrix molecules) that mediates its adherence to plasma or extracellular matrix proteins, such as collagen [13], fibronectin, Protein A and fibrinogen [70, 71, 72]. Each of these cellular MSCRAMMs interacts uniquely with their corresponding matrix proteins. But, these molecules share certain common genetic and structural features. For instance, hydrophobic amino acid residues near the C-termini prefer to attach to the cell membrane, while hydrophilic N-termini can extend the binding regions of these MSCRAMMs over cell membrane to a distance for interacting with the complementary proteins from plasma or extracellular region.

4.2 Fibrinogen-Clumping Factor Interaction

One type of adhesins that *S. aureus* expresses is called clumping factor A (ClfA), which is the cell surface protein responsible for binding to fibrinogen. Clumping factor derives its name from the fact that visible clumps of bacteria are observed in concentrated bacterial suspensions containing fibrinogen. It is a 92 kDa protein (*i.e.*, 933 amino acid residues) that consists of three different domains: a membrane and cell wall spanning domain, a serine-aspartic acid dipeptide repeat domain (“the R region”) and the fibrinogen binding domain at the end of the molecule, as shown in Figure 4.1 (b). The dipeptide (Ser-Asp) repeat region is of 308 amino acid residues in length for wild type [71]. It has been postulated that this hydrophilic dipeptide repeat region is able to extend the fibrinogen-binding domain to promote its ability to interact with its environments, even appreciably far from the cell wall. Hartford *et al.* [12] have shown that adhesion of *S. aureus* depends upon the length of this R-region by genetically engineering mutants with R-region of reduced length. Also, under the well-defined flow conditions, our research group have demonstrated that the length of this R-region promotes adhesion of *S. aureus* to fibrinogen-coated surfaces; in other

words, the relatively larger length of R-region corresponds to an enhanced rate of attachment [73, 74, 75]. The relative detailed descriptions of their experimental results are given in the last section of this chapter.

Fibrinogen is a large protein (340 kDa, ~ 40 nm) that is made up of six dimeric polypeptide chains, two of each alpha, beta and gamma chains. The affinity of fibrinogen to *S. aureus* is very strong. It is reported that the binding dissociation constant for fibrinogen-clumping factor interactions is around 9.9×10^{-9} M using radiolabeled fibrinogen method [76]¹. Also, using radiolabeled fibrinogen fragments and corresponding monoclonal antibodies, the investigators have identified that the specific region of interaction on the fibrinogen molecule to be the last twelve amino acid residues of the gamma chain [77]. A more detailed description of properties and preparation for this interacting 12-residue polypeptide is given in Ref. [74].

4.3 Model Parameter Estimations

In order to model the attachment of *S. aureus* to a surface through binding interaction between clumping factor and fibrinogen, we need to find out reasonable values for all the relevant parameters that are listed in Table 4.1. Below, a number of important parameters regarding to this specific clumping factor-fibrinogen interaction are described.

For a basic model of receptor-ligand binding, consider the case in which a monovalent receptor **R** binds reversibly to a monovalent ligand **L** in one step to form a receptor/ligand complex **C**, without any other processes modifying this interaction:



¹The value for K_D of 9.9 nM was determined for the binding of soluble fibrinogen to *S. aureus* Newman cells. Newman cells could express several fibrinogen-binding proteins that bind fibrinogen simultaneously and also each fibrinogen molecule is a dimer and has the potential to bind two copies of each bacterial fibrinogen-binding molecule. Thus, this reported value for dissociation rate constant will not be used in current study.

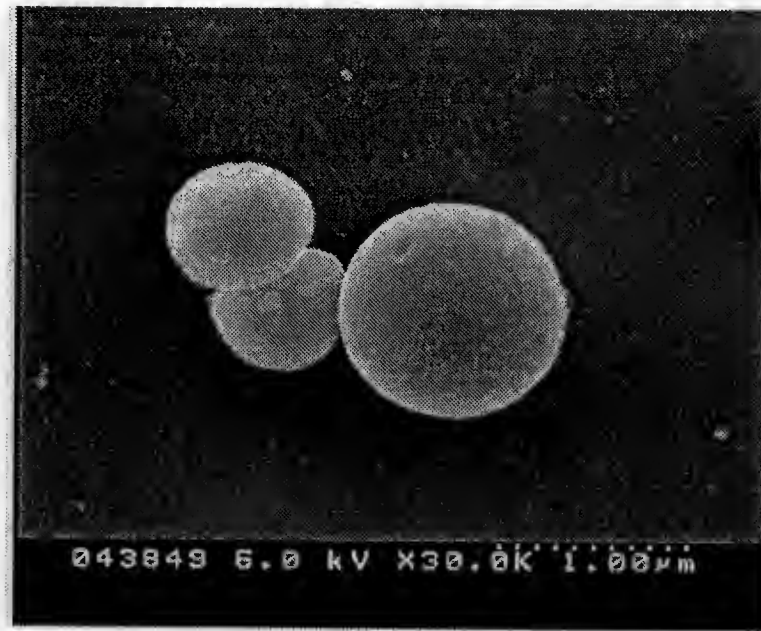


Figure 4.1: Illustration of *S. aureus* and cell surface-expressed clumping factor protein. (a) Electron micrograph of 1 μ m silica particle and *S. aureus* bacteria with diameter of about 730 nm. Source: [74] (b) A schematic of clumping factor that consists of three distinctive domains: a membrane and cell wall spanning domain, a dipeptide repeating domain and a fibrinogen-binding domain.

Table 4.1: Parameters used in the adhesion of *S. aureus* to fibrinogen-coated surface

Symbol	Parameter	Estimated value	Unit	Reference
k_f^{3D}	3-D unstressed forward binding rate constant	7563.6	$\mu\text{M}^{-1}\text{s}^{-1}$	[21]
		1.256×10^{10}	$\text{nm}^3/(\#\cdot\text{s})$	
k_{r0}^{3D}	3-D unstressed reverse rate constant	3857.6	s^{-1}	$= k_{f0}^{3D} K_{D0}^{3D}$
K_{D0}^{3D}	3-D unstressed dissociation rate constant	0.51	μM	[72]
		3.07×10^{-7}	$\#/ \text{nm}^3$	
k_{f0}^{2D}	2-D unstressed forward binding rate constant	377.3	$\mu\text{M}^{-1}\text{nm}^{-1}\text{s}^{-1}$	Eq. (4.16)
		6.265×10^8	$\text{nm}^2/(\#\cdot\text{s})$	
k_{r0}^{2D}	2-D unstressed reverse rate constant	3857.6	s^{-1}	$= k_{f0}^{2D} K_{D0}^{2D}$
K_{D0}^{2D}	2-D unstressed dissociation rate constant	10.2	$\mu\text{M}\cdot\text{nm}$	Eq. (4.18)
		6.155×10^{-6}	$\#/ \text{nm}^2$	
γ_b	bond stiffness	0.06	pN/nm	Eq. (4.11)
		0.015	$\text{k}_B\text{T}/\text{nm}^2$	
z_0	unstressed bond length	40	nm	[75, 74]
σ^2	variance of bond fluctuations	64	nm^2	
ϵ_0	unstressed bond energy	-4.4	k_BT	Eq. (4.20)
$[L]_{2D}$	number density for ligands	0.0005	$\#/ \text{nm}^2$	[20]
N	number of receptors in contact area	50	—	

again, where k_f is the forward binding rate constant and k_r is the reverse rate constant. The equation describing the time rate of change of the receptor/ligand complex is

$$\frac{d[C]}{dt} = k_f [R][L] - k_r [C], \quad (4.2)$$

where $[R]$, $[L]$ and $[C]$ are the concentrations for receptor, ligand and their binding complex molecules, respectively.

As well known, however, the binding of two molecules in chemical reaction kinetics is really a two-step process, requiring first molecular transport of each individual molecular species with transport rate constant k_t before intrinsic chemical reactions or binding interactions can occur, as shown in Figure 4.2. Usually at cellular and subcellular length scales, diffusive transport dominates convective transport, so that we can consider the transport mechanism to be molecular diffusion. The chemical or binding reaction itself is then characterized by the intrinsic association rate constant k_{on} and intrinsic dissociation rate constant k_{off} . Thus, the measured values for k_f and k_r in kinetic experiments are really the combination rate constant including both the transport and reaction effects. Below, we shall estimate the contributions of each individual rate constant to the overall rate constants for the clumping factor-fibrinogen interaction.

Usually, experimental measurements of binding kinetic rate constants are conducted when both reacting components are in soluble forms (denoted as 3-D binding kinetics hereinafter). Attempts to measure two dimensional binding kinetics have just begun recently. As of now, there are very limited measurement data reported in literature regarding to adhesion kinetics of *S. aureus* to fibrinogen-coated surfaces, where both reacting molecules are attached to the surfaces (*i.e.*, 2-D binding kinetics). So in what follows, we shall derive a relationship between 3-D and 2-D kinetics.

Let's first study 3-D binding kinetics. If both receptor and ligand molecules are in extracellular medium, that is, they are freely to move in three-dimensional

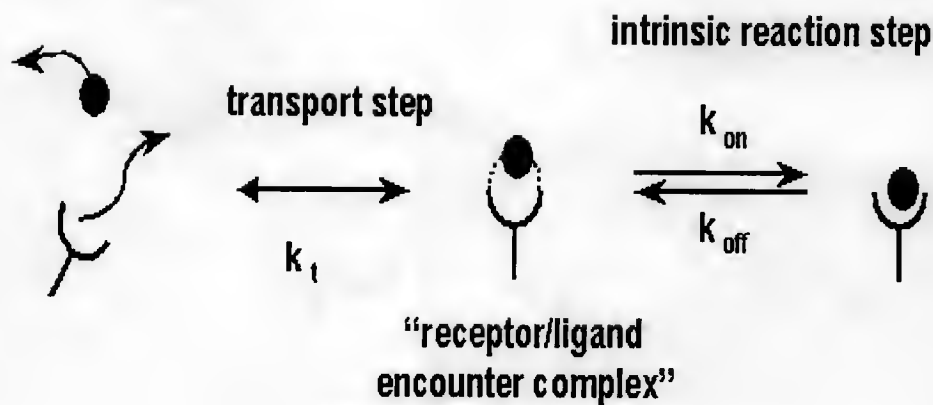


Figure 4.2: Separation of the overall binding or dissociation event into two steps. The intrinsic binding step is characterized by rate constants k_{on} and k_{off} that are determined by the molecular properties of receptor and ligand molecules. The transport step is characterized by rate constant k_t which is influenced by diffusion and geometric considerations. The intermediate step where receptor and ligand are close enough but have yet formed the bond is termed as receptor/ligand “encounter complex”. Source: [21]

directions, it has been shown that [78]

$$k_f = \frac{k_t k_{on}}{k_t + k_{on}} = \left(\frac{1}{k_t} + \frac{1}{k_{on}} \right)^{-1}, \quad (4.3)$$

with

$$k_t = 4\pi D s, \quad (4.4)$$

where the diffusion coefficient D is sum of the receptor and ligand diffusivities, *i.e.*, $D = D_R + D_L$; and s is the encounter radius assuming the origin of a spherical coordinate system is placed at the center of the receptor molecule. Generally, for receptors and ligands in free solutions, the experimentally measured value for k_f is more close to reaction-limited binding regime, so that $k_f \sim k_{on}$, under the condition of $k_{on} \ll k_t$. Here, however, for a very crude estimation, we would use $k_t = 4\pi D s$ to approximate k_{on} . Assuming $D = 10^{-6} \text{ cm}^2/\text{s}$ (which is usually in the range of $10^{-5} \sim 10^{-7} \text{ cm}^2/\text{s}$ for species of cellular or subcellular length scales) and $s = 10$

nm (which is generally $1 \sim 10$ nm), then $k_f = k_{on} \simeq 1.256 \times 10^{-11} \text{ cm}^3/\text{s} \simeq 7563.6 \mu\text{M}^{-1}\text{s}^{-1}$. (Note, here we have used Avogadro's number to convert the units for k_f to $\mu\text{M}^{-1}\text{s}^{-1}$.) Therefore, $k_{off} = K_D^{3D} k_{on} = 0.51 \mu\text{M} \times 7563.6 \mu\text{M}^{-1}\text{s}^{-1} = 3857.6 \text{ s}^{-1}$. Here, $K_D^{3D} = 0.51 \pm 0.19 \mu\text{M}$ is obtained from Ref. [72] through measurement of binding of soluble clumping factor to immobilized fibrinogen using a surface plasmon resonance sensor.

The above analysis is applicable for cases when both receptor and ligand molecules are in free solutions. In fact, however, when both of them are anchored to surfaces as for the adhesion of *S. aureus* to fibrinogen-coated surface, movements for receptor and ligand molecules along the direction perpendicular to the surfaces are not allowed except Brownian motions for the non-grafted ends. Clearly, 2-D binding kinetics differ greatly from 3-D case. In what follows, symbols 3D and 2D are used as superscripts or subscripts to distinguish between these two scenarios.

Suppose ligand molecules (or complementary binding sites) on the substrate surface greatly outnumber receptor molecules over the particle surface, then the number density for ligand molecules, $[L]_{2D}$, could be assumed as a constant, and thus, the receptor-ligand binding reaction reduces to the simplest case of macromolecular binding reaction that has been examined in Chapter 3. In other words, the occurrence of binding between receptor and ligand molecules can be interpreted as that a receptor molecule changes from its free state to bound state. Let the total number of receptor molecules available for binding within the contact region be N , and the number of receptor-ligand complex formed be n , then the balance equation for species n can now be written as

$$\frac{dn}{dt} = k_f(z)(N - n)[L]_{2D} - k_r(z)n. \quad (4.5)$$

At equilibrium, one has

$$\frac{k_r(z)}{k_f(z)} = \frac{[N - n_{eq}(z)][L]_{2D}}{n_{eq}(z)} = K_D^{2D}(z). \quad (4.6)$$

Rearranging the above equation leads to

$$\frac{n_{eq}(z)}{N - n_{eq}(z)} = \frac{[L]_{2D}}{K_D^{2D}(z)}. \quad (4.7)$$

Combination of the above equation with Eq. (3.33) in Chapter 3 yields

$$\frac{n_{eq}(z)}{N - n_{eq}(z)} = e^{-\epsilon(z)/k_B T} = \frac{[L]_{2D}}{K_D^{2D}(z)}. \quad (4.8)$$

The bond energy, $\epsilon(z)$, is then given by

$$\epsilon(z) = -k_B T \ln \left(\frac{[L]_{2D}}{K_D^{2D}(z)} \right). \quad (4.9)$$

We shall return to this equation for evaluation of the unstressed bond energy ϵ_0 shortly after we derive a relationship between 2-D kinetic rate constants and experimentally measured 3-D values.

Assuming each ligand molecule on the substrate surface is capable of sampling laterally all the corresponding receptors on the particle surface without restrictions, and the free end of ligand molecule (where the binding domain is located at) can undergo unhindered Brownian motions, although the other end of the molecule is clamped at the surface, as illustrated in Figure 4.3. Based on this assumption, 2-D binding kinetics differs from 3-D binding kinetics only in the vertical movements (*i.e.*, z direction) of ligand molecules. For the case of receptor-ligand binding interactions confined within the contact region, the effective concentration of the free ends of ligand molecules, which is now distance-dependent, exhibits a Gaussian distribution with positions centered at z_0 . Again, z_0 here is the unstressed receptor-ligand bond length, or z_0 can also be interpreted to represent the equilibrium “stalk” length of clumping factor molecules expressed on *S. aureus* surface. In other words, the probability of finding the binding ends of ligand molecules at distance z can be described by a normal distribution as follows:

$$p(z) = \frac{1}{\sigma\sqrt{2\pi}} \exp \left[-\frac{\gamma_b}{2k_B T} (z - z_0)^2 \right], \quad (4.10)$$

where σ is the width of Gaussian distribution and is related to bond stiffness γ_b through

$$\sigma^2 = \frac{k_B T}{\gamma_b}. \quad (4.11)$$

Let the surface density of ligand molecules on the particle surface be $[L]_{2D}$, the effective concentration of the free ends of ligand molecules in the contact region, which now depends upon the distance, is given by

$$[L]_{3D}(z) = [L]_{2D} p(z). \quad (4.12)$$

Therefore, 2-D forward binding rate constant is related to 3-D one through the use of Eq. (4.12) as follows

$$k_f^{2D}(z) [L]_{2D} = k_f^{3D} [L]_{3D}(z), \quad (4.13)$$

$$= k_f^{3D} [L]_{2D} p(z), \quad (4.14)$$

$$= \frac{k_f^{3D}}{\sigma \sqrt{2\pi}} [L]_{2D} \exp \left[-\frac{\gamma_b}{2k_B T} (z - z_0)^2 \right]. \quad (4.15)$$

Assuming the strain dependence of the transition state between a bound state and a free state for receptor-ligand bonds, like the dynamic model developed by Dembo *et al.* [26], one sees that

$$k_f^{2D}(z) = \frac{k_f^{3D}}{\sigma \sqrt{2\pi}} \exp \left[-\frac{\gamma_b}{2k_B T} (z - z_0)^2 \right] \implies k_{f0}^{2D} = \frac{k_f^{3D}}{\sigma \sqrt{2\pi}}, \quad (4.16)$$

where k_{f0}^{2D} is the unstressed forward binding rate constant for 2-D binding kinetics. So, this relationship provides a way to estimate 2-D forward binding rate constants from measured 3-D values, provided that we know σ , which is directly related to the properties of the bonds formed between the bacterium and the substrate and will be addressed shortly.

Usually, detachment kinetics is much more complicated than attachment kinetics. Recently, numerous studies involved in probing single molecular bond kinetics under applied forces [27, 54] suggest that the dissociation rate constant be influenced

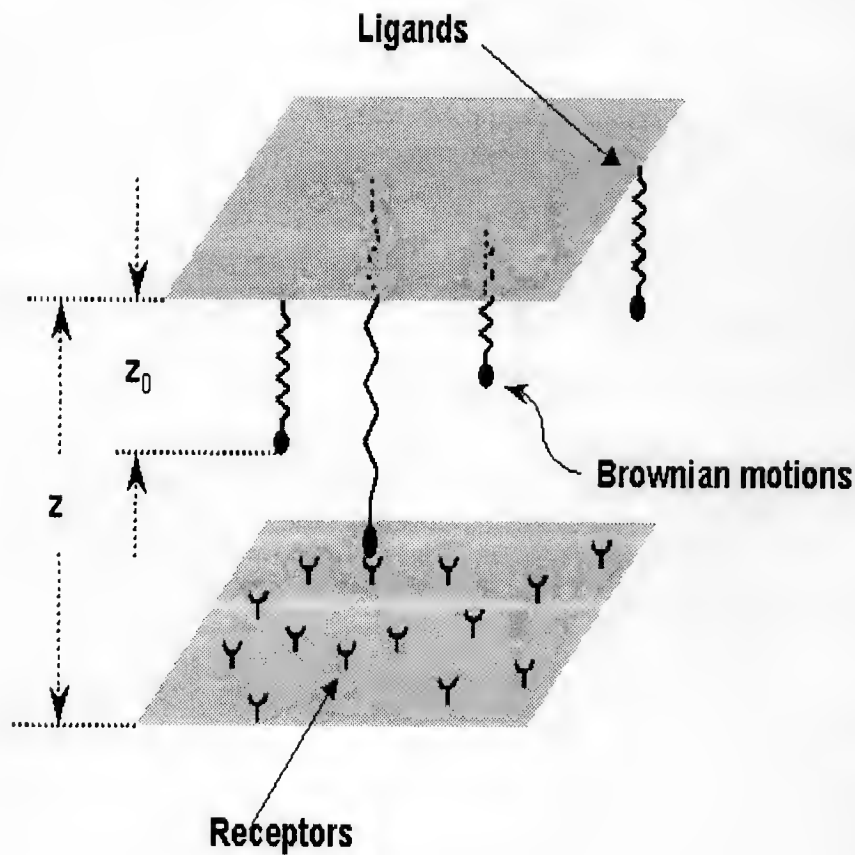


Figure 4.3: Illustration of receptor-ligand binding interaction confined between the particle and substrate surfaces (which are assumed to be flat, uniform with constant areas). Receptor-ligand bonds formed are treated as springs with binding energy increasing parabolically when being pulled/compressed away from their equilibrium position z_0 . The free end of ligand molecules undergoes unhindered Brownian motions, which indicates that the effective concentration of ligand molecules within the contact region exhibits a Gaussian distribution.

by many factors, such as the energy landscape that the bonds are subjected to, the magnitude and direction of the external forces applied, the loading rate of external forces, and the like. The whole dissociation process is a dynamic process, given the fact that the bond can dissociate spontaneously under zero force. Bell [20] estimated that the strength of a single bond, denoted as F here, is approximately

$$F \approx 1.7 (6\pi) R^2 \tau_s, \quad (4.17)$$

where τ_s is the shear stress applied and R is the radius of the bacterium. Under physiological conditions, the receptor-ligand binding complexes (or other macromolecular bonds) are subjected to fluid shear stress with corresponding shear rate ranging from 40 to 2000 s^{-1} . Thus, the force that a single bond experiences is roughly within the range of $0.1 \sim 6 \text{ pN}$, which is relatively weak. In addition, since we are focusing on the attachment of *S. aureus* to fibrinogen-coated surface, for simplicity, the reverse binding rate constant is assumed not to be affected by external stress; in other words, k_r is treated as a constant here. Therefore, in view of Eq. (4.16) 2-D dissociation rate constant is related to 3-D one through the following equation

$$K_{D0}^{2D} = \frac{k_r}{k_{f0}^{2D}} = \frac{k_r}{k_{f0}^{3D}} \sigma \sqrt{2\pi} = K_D^{3D} \sigma \sqrt{2\pi}. \quad (4.18)$$

Now, we switch back to discussions on estimation of receptor-ligand bond energy from binding kinetics. In view of Eqs. (4.9), (4.12) and (4.18), one sees that

$$\epsilon_0 = -k_B T \ln \left(\frac{[L]_{2D}}{K_D^{2D}(z_0)} \right), \quad (4.19)$$

$$= -k_B T \ln \left(\frac{[L]_{2D}}{\sigma \sqrt{2\pi} K_D^{3D}} \right). \quad (4.20)$$

Next, we are going to evaluate the stiffness of clumping factor-fibrinogen bridges. As described earlier, the R-region in the clumping factor molecule consists of only alternating serine and aspartic acid amino acid residues. Assuming this dipeptide repeat region is α -helical [73], one can estimate the length of the R-region

in nanometers based upon the number of residues contained in this region. Then, we need to make a reasonable approximation about the stiffness of the fibrinogen-clumping factor bond, which is assumed to contain mainly the R-region (“stalk” region) of varied lengths from the clumping factor molecule. Statistical mechanical theory for semiflexible chains in semidilute solutions is used here to estimate the stiffness of these bonds. Suppose that a semiflexible R-region “stalk” of length L can be treated as a Hookean spring, then its stiffness, γ_b , is given by [79]

$$\gamma_b = \frac{k_B T \lambda_p^2}{L^4}, \quad (4.21)$$

where λ_p is the “stalk” persistence length, which could not be found in literature even though the dipeptide “stalk” repeat region is assumed to be α -helix. As a first attempt, the persistence length for actin filament² would be used here for a very coarse approximation. So, λ_p is assumed to be around 200 nm. Then the variance of “stalk” bond fluctuations is obtained from Eq. (4.11), and thus, $\sigma \simeq 8$ nm. In turn, $k_{f0}^{2D} = 377.3 \mu\text{M}^{-1}\text{nm}^{-1}\text{s}^{-1}$ from Eq. (4.16) and $K_{D0}^{2D} = 10.2 \mu\text{M}\cdot\text{nm}$ from Eq. (4.18). Suppose that the number density of ligand molecules on the particle surface, $[L]_{2D}$, is about 0.0005 #/nm² (which corresponds to about 45 nm of spacing between the grafted ends of ligand molecules [20]), then the unstrained receptor-ligand bond energy is given as $\epsilon_0 = -4.4 k_B T$ by using Eq. (4.20). The estimated values for these parameters are listed in Table 4.1.

4.4 Model Predictions and Comparison with Experimental Data

In order to use the dynamic model developed in Chapter 3 (or the corresponding MatLab codes attached in Appendix) to calculate the deposition rate constant of *S. aureus* to a surface covered with fibrinogen, a few more parameters are needed and discussed here. The size of the contact area on the bacterial surface, which is assumed to be flat and uniform, is estimated to be about 10 percent of the whole

²Actin filaments belong to another major research area in our research group.

surface area of *S. aureus* with diameter of about 730 ± 10 nm as shown in Figure 4.1(a). The number of receptors on the substrate available in binding in this contact region is taken as $N = 50$, which corresponds to a smaller surface density than that of ligand molecules on *S. aureus* surface. To convert the bi-molecular reaction between receptor and ligand into mono-molecular one under the assumption of excess ligand molecules, the forward binding rate constant is actually the product of k_{f0}^{2D} and $[L]_{2D}$, which gives us a value of 3.13×10^5 s⁻¹.

A series of equilibrium force measurements between a *S. aureus* bacterium and various substrates have been conducted in our research group using the optical trapping technique, which is described in details in Chapter 6. Figure 4.4 shows two force-distance profiles for a *S. aureus* cell with deleted “stalk” region compared to that with genetically engineered “stalk” length of about 46 nm from Ref. [74]. For a bacterium with longer “stalk” region, attraction occurs at a distance far away from the surface and allows the bacterium to overcome repulsions for attachment. The interactions present here include van der Waals attractions, electrostatic and steric repulsions as well as receptor-ligand binding interactions. Since there is always a strong attraction occurring between fibrinogen and clumping factor molecules with sufficient long “stalk” region expressed on the surface of *S. aureus*, which is indicated by the “jump” of the bacterium to the surface to adherence in Figure 4.4, direct fitting to such measured equilibrium force-distance curves to extract parameters turns out to be not easy. In retrospect, it would have been good to have also measured certain isolated repulsive as well as attractive force-distance profiles so as to fit them separately to obtain better fitting parameters. Since such force measurements are not currently available, as an approximation, the measured equilibrium force-distance curve between *S. aureus* and β -casein coated surface from Ref. [74] (where specific binding interactions are absent) is used here and severed as a target fit curve to get reasonable values for repulsive forces. For the purpose of simplicity, the repulsive

potential is assumed to consist of only electrostatic and steric repulsions that are characteristic of having an exponential decay with decay length of about 27.5 nm, which is obtained by extracting the experimental data from Ref. [74] and by fitting them with a phenomenological expression for repulsive potential as shown in Figure 4.5. And the baseline repulsive potential is found to be about $9.2 \text{ k}_B\text{T}$.

Using the parameter values shown in Table 4.1, the total interaction energy at equilibrium, along with the decomposed surface repulsive potential and attractive binding interaction, is plotted as a function of separation distance in Figure 4.6 for a *S. aureus* cell with “stalk” length of 40 nm. From the plot, one can see that the attraction resulted from clumping factor-fibrinogen binding reaction dominates over repulsions over the entire characteristic interaction domain of *S. aureus* to the surface, assuming here that such binding interactions are allowed to reach equilibrium. The energy barrier at the saddle transition region that prevents bacterial cells from attachment is much less evident, which is akin to the equilibrium force measurement results shown in Figure 4.4. Thus, one would speculate that the deposition rate constant (or time to attachment) for a *S. aureus* to a fibrinogen-coated surface is governed by particle diffusion when far away from the surface; and then when the bacterium is near the surface, the strong attraction between clumping factor and fibrinogen molecules will pull the particle into the primary energy minimum and lead to attachment. The mean first-passage time approach developed in Chapter 3 might not be applicable for this particular case, because particle attachment rate is not determined mainly by the energy barrier (less than $3 \text{ k}_B\text{T}$ as shown in Figure 4.5) and the dynamic properties of bacterial particle at the saddle transition region. To demonstrate the validity of the above speculation, the effect of “stalk” length on the deposition rate constants of *S. aureus* cells to fibrinogen-coated surface is illustrated in Table 4.2. From this table, one can see that k_+ first slightly increases and then decreases greatly as z_0 increases, which is quite contrary to what would be expected

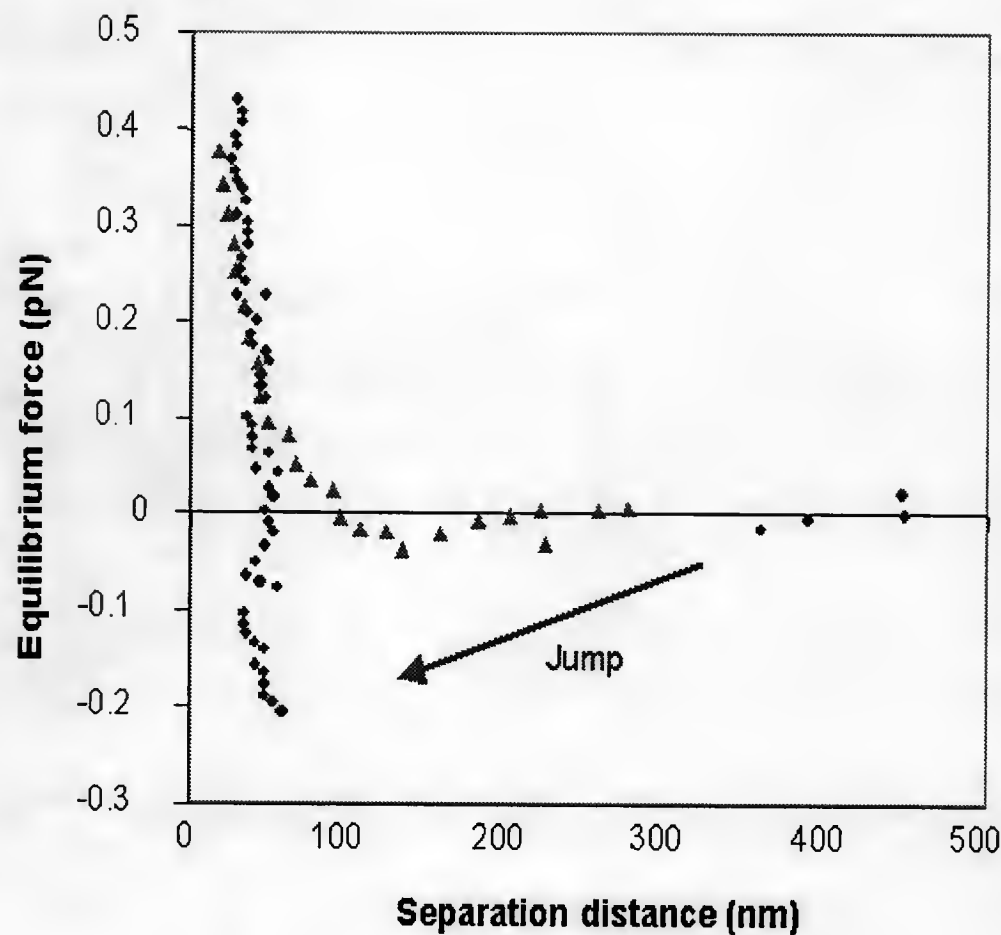


Figure 4.4: Equilibrium force-distance profiles measured by optical trapping technique for interaction between *S. aureus* and fibrinogen-coated surface. Triangles: bacterial cells with deleted stalk; Circles: bacterial cells with stalk length of about 46 nm. For a bacterium with longer stalk length, the bacterium will jump to the surface and become attached at a distance much larger than its actual stalk length. Source: [74]

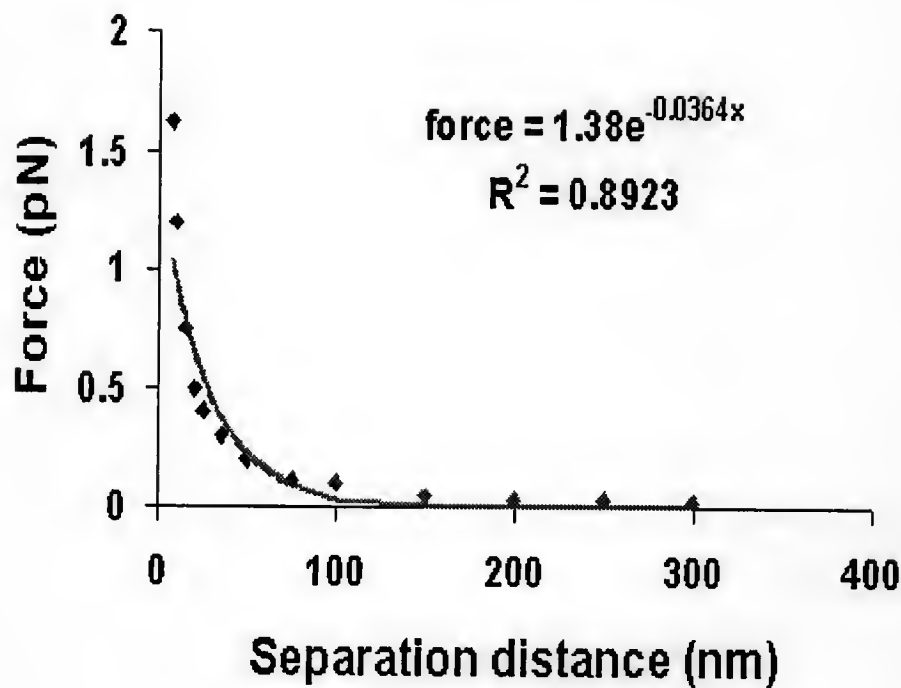


Figure 4.5: Fitting of the measured equilibrium force-distance profile between *S. aureus* and β -casein coated surface from Ref. [74] with a phenomenological expression for repulsion that is assumed to consist of electrostatic repulsion and steric stabilization, namely, $\phi(z) = \phi_0 \exp(-bz)$, which leads to $d\phi/dz = \phi_0(-b)\exp(-bz)$, and the latter is used to fit the the measured force-distance curve to extract values for fitting parameters.

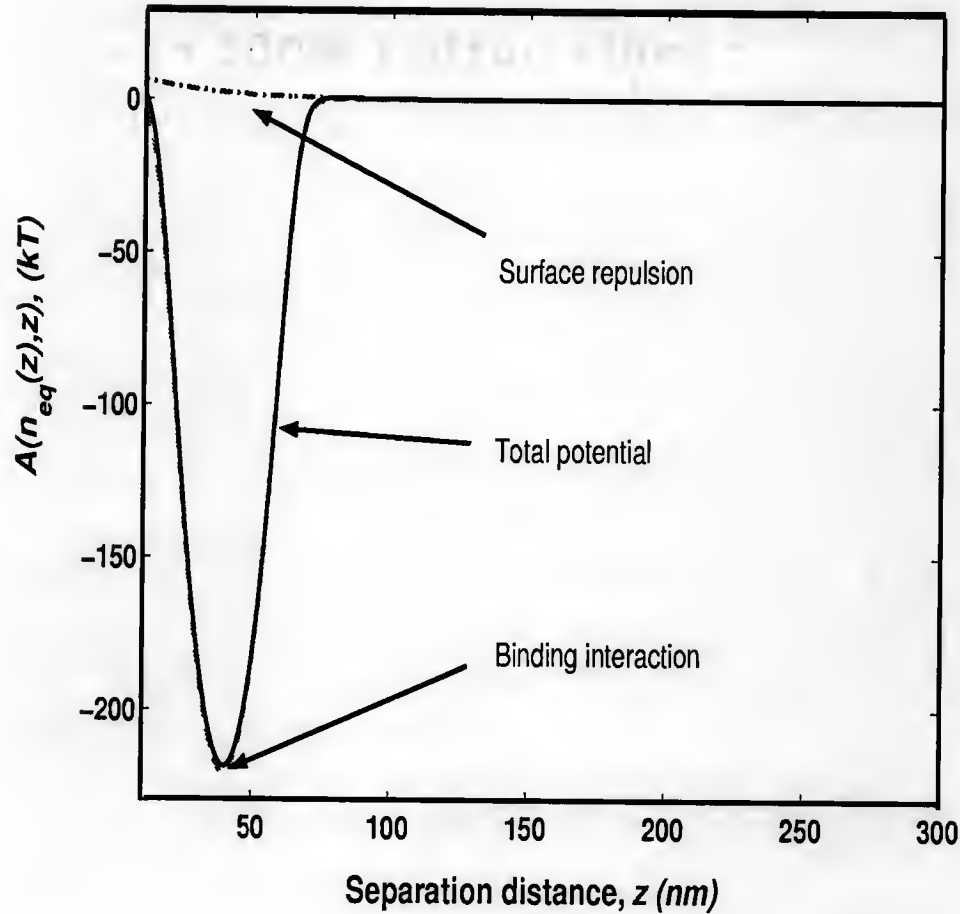


Figure 4.6: The total interaction energy at equilibrium, along with the decomposed surface repulsive potential and attractive binding interaction, is plotted as a function of separation distance for a *S. aureus* cell with “stalk” length of 40 nm.

to happen, namely, longer z_0 tends to lower the energy barrier at saddle and thus promote attachment, as already demonstrated in Figure 3.8 in Chapter 3 and also in Figure 4.8 below. Therefore, we may conclude that the analytical MFPT method can not be utilized here to compute k_+ . However, the dynamic model developed in Chapter 3 still applies to the current case, and numerical simulations with their basis on the model are performed below to calculate again the effect of z_0 on k_+ .

The MatLab codes used to calculate the time to attachment (or the deposition rate constant) for *S. aureus* to a surface through clumping factor-fibrinogen

Table 4.2: The effect of stalk length on attachment of *S. aureus* to fibrinogen-coated surface. The calculations were done by the analytical MFPT method and the parameter values are listed in Table 4.1.

z_0	nm	5	10	15	20	30
ΔA	$k_B T$	1.9	1.5	1.3	1.0	0.7
k_+	$\mu\text{m}/\text{min}$	2.34×10^{-4}	2.46×10^{-4}	2.45×10^{-4}	2.28×10^{-4}	1.74×10^{-4}
z_0	nm	40	50	60	70	100
ΔA	$k_B T$	0.5	0.3	0.2	0.15	0.05
k_+	$\mu\text{m}/\text{min}$	1.20×10^{-4}	7.20×10^{-5}	4.19×10^{-5}	2.30×10^{-5}	3.23×10^{-6}

binding interactions are similar to those in Appendix, but with key parameter values listed in Table 4.1. From the above description, for the attachment of *S. aureus* to fibrinogen-coated surface based on the energy landscape as illustrated in Figure 4.6, particle diffusion determines attachment rate until the particle approaches near the surface where strong attractions due to clumping factor-fibrinogen binding interaction dominate and cause the particle to attach. Figure 4.7 illustrates the dependence of the mean first-passage time, $T_p(z)$, as a function of separation distance for a *S. aureus* bacterium with “stalk” length of 40 nm. One can see that $T_p(z)$ decreases monotonously with the distance as the bacterium moves towards the surface, which is consistent to the diffusive transport mechanism before the bacterium reaches the saddle point.

The deposition rate constant, k_+ , is plotted as a function of “stalk” length in Figure 4.8, where k_+ is extracted from Eq. (2.3) in Chapter 2 using parallel plate flow chamber assay to measure the attachment kinetics of *S. aureus* with genetically engineered “stalk” of varied length under a simple shear flow [75]. From the graph, one sees that a larger “stalk” length will allow the bacterial cell to effectively extend over the energy barrier at saddle and then to adhere to the surface. The underlying physical interpretation of this observation is that longer “stalk” length tends to lower the energy barrier at saddle, and at the same time shifts the positions of primary

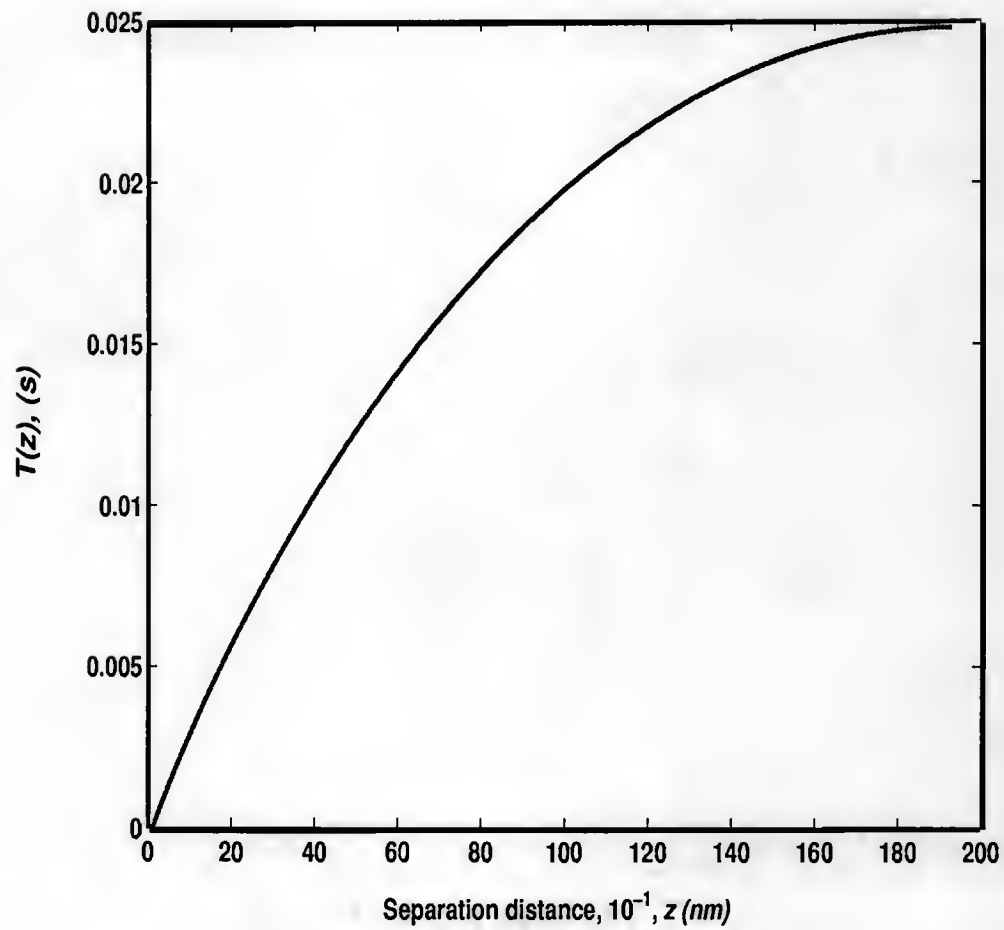


Figure 4.7: The mean first-passage time, $T_p(z)$, is plotted as a function of separation distance for a *S. aureus* bacterium with stalk length of about 40 nm from numerical simulations.

energy wells away from the surface to promote attachment, as demonstrated in Figure 3.9. The predicted results for the mean first-passage time from numerical simulations are shown in Figure 4.9. One can see from the plot that as “stalk” length, z_0 , increases, T first decreases linearly with z_0 then approaches to zero ³. Likewise, k_+ first increases linearly with z_0 and then also reaches to a plateau as “stalk” length increases.

³Something is not correct here. Since there is no obvious energy barrier on the energy landscape, and also binding interaction between clumping factor and fibrinogen is very fast, attachment of *S. aureus* to fibrinogen-coated surface is really diffusion-limited. Therefore, the mean first-passage time method calculated should approach the asymptote determined by particle diffusion, rather than approach to zero. Further investigation of this point will be addressed in a letter to this thesis.

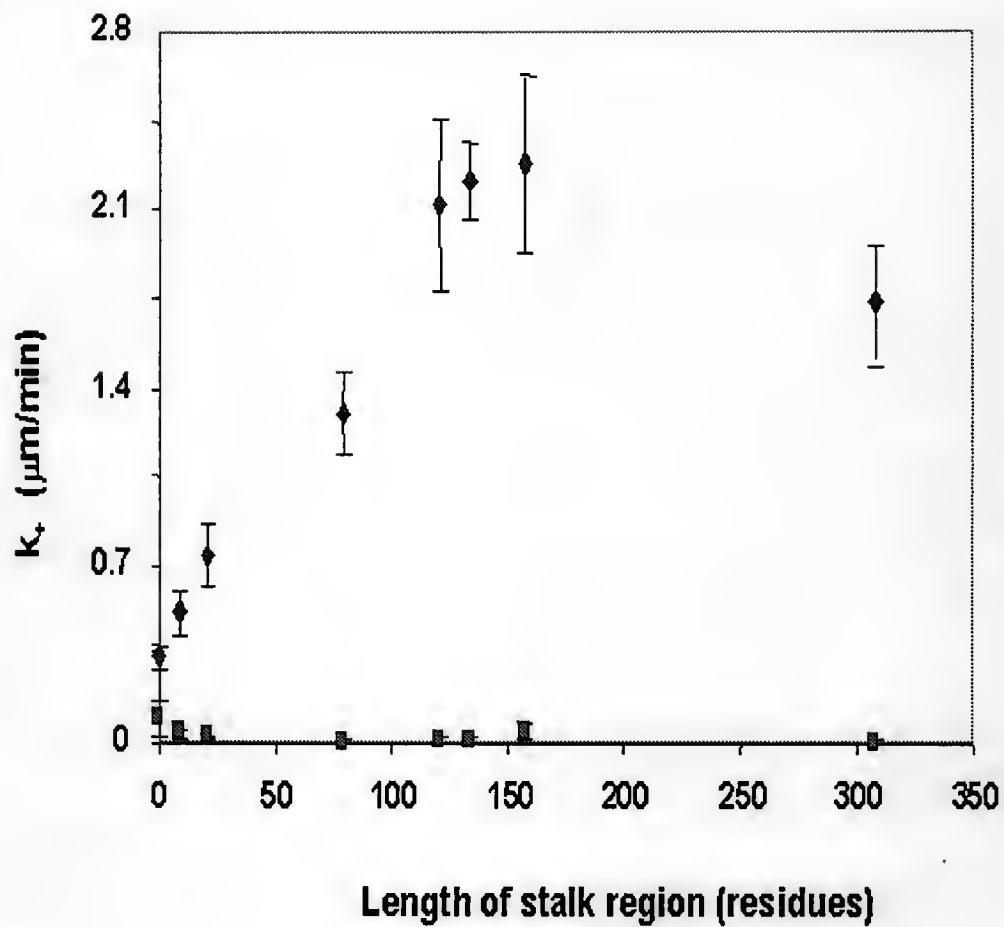


Figure 4.8: The deposition rate constant, k_+ , is plotted versus stalk length for the attachment of *S. aureus* to fibrinogen-coated surface in a flow field measured by PPFC (parallel plate flow chamber) assay. Diamonds: bacterial cells with varied stalk length; Squares: bacterial cells with deleted stalk. Source: [75]

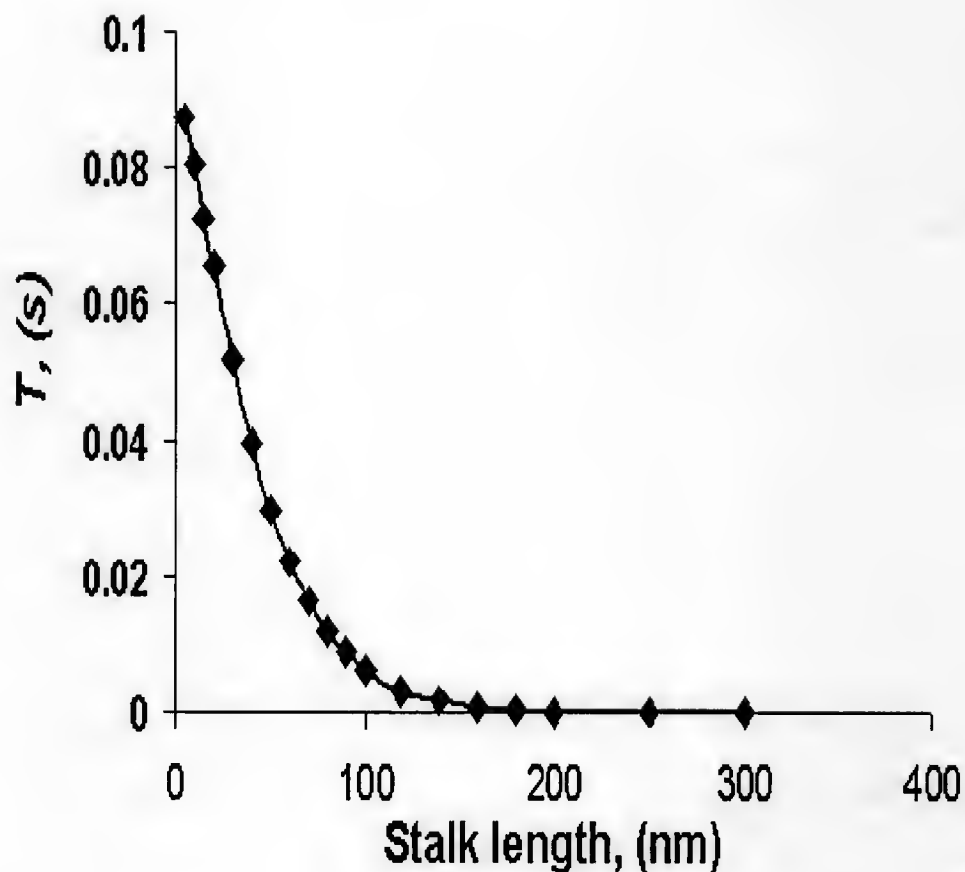


Figure 4.9: The deposition rate constant, k_+ , is plotted versus stalk length for the attachment of *S. aureus* to fibrinogen-coated surface. The calculations are done using mean first-passage time method as described in Chapter 3. The parameters used in the calculations are listed in Table 4.1.

CHAPTER 5 EFFECT OF PARTICLE CURVATURE ON ATTACHMENT

For real cells, a roughly flat contact zone might be formed upon close approach to other cells or substrata as a result of the hydrodynamic pressure that would build up in the contact region as well as the deformability of cell membranes. Thus, an assumption of a uniform contact zone might not deviate too much from the actual situations for the early stage of cellular adhesion. In many other adhesion cases, however, the surface of biological particles is not flat and also is somewhat rigid, less deformable. Therefore, accurate predictions on deposition rate constants of such particles to surfaces necessitate a more accurate account for the effects of particle curvature on attachment. Here, following the analysis in Chapter 3, a derivation of mean first-passage time method to obtain particle attachment rate constant that considers curvature effects of the particle is described.

5.1 Effect of Curvature on Particle-Surface Interaction Energy

The spherical and rigid biological particle under consideration is illustrated in Figure 5.1. The separation distance between the particle surface and the substrate is given by $z + R(1 - \cos \theta)$, where θ is the angle from the nearest point on the particle surface to the substrate, and R is the radius of the particle. Similarly as in Chapter 3, for the purpose of simplicity, the bonds formed between the particle and the surface are also treated to behave like ideal springs, thus, the bond energy, $\epsilon(z, \theta)$, with a quadratic dependence on the separation distance, is given by

$$\begin{aligned}\epsilon(z, \theta) &= \epsilon_0 + \frac{\gamma_b}{2} [z + R(1 - \cos \theta) - z_0]^2, \quad 0 \leq \theta \leq \frac{\pi}{2} \\ &= \infty, \quad \text{otherwise}\end{aligned}\quad (5.1)$$

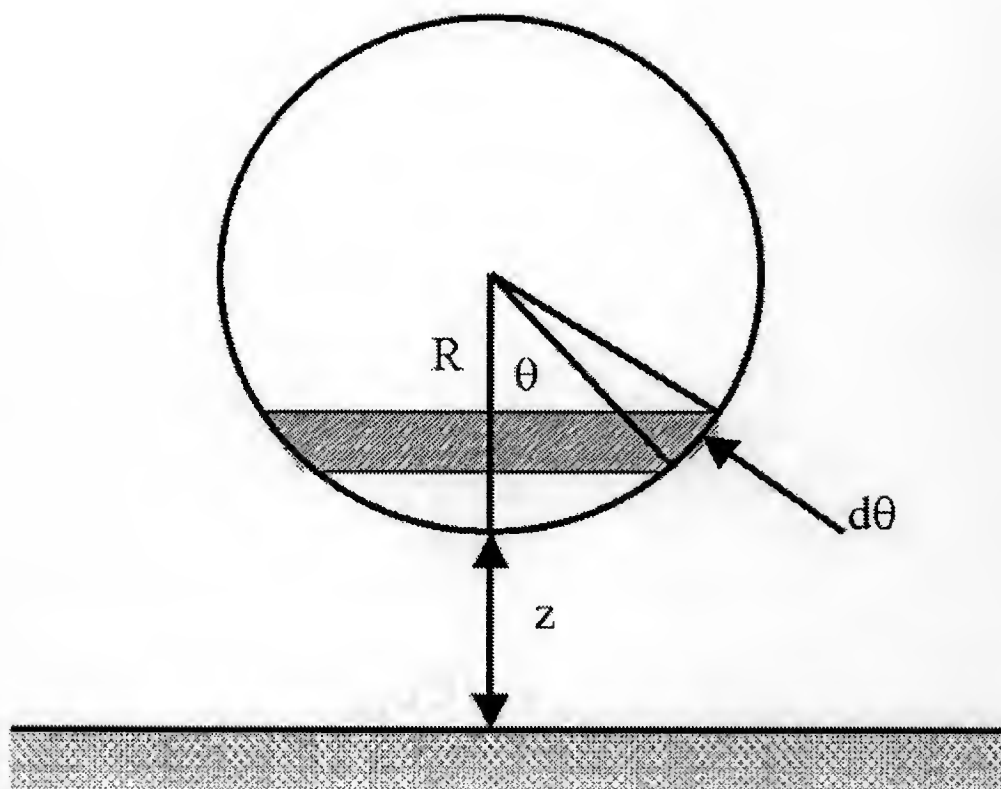


Figure 5.1: A schematic for attachment of a spherical particle to a surface, where the positions of binding molecules over the particle surface are described by angle θ .

where ϵ_0 is the unstrained bond energy and z_0 is the unstrained bond length. Here, we have assumed that the bonds cannot be formed when $\theta > \frac{\pi}{2}$, that is, the bonds are more rigid and less flexible such that they are not able to bend themselves along the curved particle surface. For any individual binding molecule, it will be in either bound or free state with binding energy of either $\epsilon(z, \theta)$ or 0, respectively. Let the partition function of a free molecule be 1, and that of a single bound macromolecule be Z_b , which is given by [80, 81]

$$Z_b(\theta) = e^{-\epsilon(z, \theta)/k_B T}. \quad (5.2)$$

If the binding molecules over the particle surface are assumed to be independent, indistinguishable and immobile, the total canonical partition function, Z , for the particle is [80, 81]

$$Z = \prod_0^{\pi/2} \frac{N_\theta!}{(N_\theta - n_\theta)! n_\theta!} Z_b(\theta)^{n_\theta}, \quad (5.3)$$

where N_θ , equal to $2\pi R^2 \rho \sin \theta d\theta$, is the number of the binding molecules on the particle surface at an incremental $d\theta$ zone at angle θ , n_θ is the number of the bonds formed at this same region (shown as shaded area in Figure 5.1), and ρ is the surface density of the binding macromolecules (Note: the distribution of these binding molecules over the particle surface could be uniform or angle dependent). Hence, the total Helmholtz free energy that includes non-specific and specific binding interactions is then given by

$$A(\bar{n}_\theta, z) = \phi(z) - k_B T \ln Z \quad (5.4)$$

$$= \phi(z) + \int_0^{\pi/2} \left[n_\theta \epsilon(z, \theta) - k_B T \ln \frac{N_\theta!}{(N_\theta - n_\theta)!} \right] d\theta, \quad (5.5)$$

where $\phi(z)$ represents all the non-specific interactions such as electrostatic, van de Waals and steric interactions, \bar{n}_θ is a vector with varying θ , and Eq. (5.5) is obtained using Eq. (5.3). Next, applying the Sterling's approximations for large N_θ and n_θ ¹,

¹In order to use Sterling's approximation, N_θ and n_θ here should be relatively large. If we approximate $\ln(n!) \approx n \ln(n) - n$, then when $n \geq 5$, it turns out to be a roughly accurate estimate.

the above equation becomes

$$A(\bar{n}_\theta, z) = \phi(z) + \int_0^{\pi/2} \left[n_\theta \epsilon(z, \theta) + (N_\theta - n_\theta) k_B T \ln \frac{N_\theta - n_\theta}{N_\theta} + n_\theta k_B T \ln \frac{n_\theta}{N_\theta} \right] d\theta. \quad (5.6)$$

5.2 Effect of Curvature on Dynamic Process

The binding macromolecules at different positions on the particle surface react independently with the complementary binding sites on the substrate. It is reasonable to assume Markovian processes for all variables n_θ and z , thus, the equation for the conservation of probability densities is

$$\partial_t p(\bar{n}_\theta, z, t) = -\partial_z J_z - \int_0^{\pi/2} [J_{n_\theta+1 \rightarrow n_\theta} - J_{n_\theta \rightarrow n_\theta-1}] d\theta, \quad (5.7)$$

where $p(\bar{n}_\theta, z, t)$ is the joint probability density of particle with bond number distribution as \bar{n}_θ at separation distance z at time t . The treatment used here is that every new n_θ (that is, the bonds formed at a differing angle θ) is added onto the probability balance equation as a new dimension. Likewise, J_z , the probability flux J at the z direction, is given by

$$J_z = -\frac{D(z)}{k_B T} \frac{\partial A(\bar{n}_\theta, z)}{\partial z} p(\bar{n}_\theta, z, t) - D(z) \partial_z p(\bar{n}_\theta, z, t), \quad (5.8)$$

and $J_{n_\theta \rightarrow n_\theta-1}$, the probability flux in n_θ dimension, is then given by

$$J_{n_\theta \rightarrow n_\theta-1} = -k_r(z, \theta) n_\theta p(n_\theta, z, t) + k_f(z, \theta) [N_\theta - (n_\theta - 1)] p(n_\theta - 1, z, t), \quad (5.9)$$

where the angle-dependent (*i.e.*, distance dependent) $k_r(z, \theta)$ and $k_f(z, \theta)$ are the bond dissociation and formation rate constants, respectively. We can see that Eq. (5.7) is difficult to be solved analytically. So, next we shall simplify it through the use of van Kampen's system size expansion, and then use MFPT method to obtain analytical approximations for the resultant equation.

5.2.1 van Kampen's System Size Expansion

As described earlier, each individual binding macromolecule on the particle surface is in either bound or free states with binding energy of $\epsilon(z, \theta)$ or 0, respectively, and so, the probability of finding a binding molecule being in bound state is $\frac{e^{-\epsilon(z, \theta)/k_B T}}{1 + e^{-\epsilon(z, \theta)/k_B T}}$. The average number of bonds formed (namely, the bond number at equilibrium) at angle θ region is

$$n_{eq}(z, \theta) = N_\theta \frac{e^{-\epsilon(z, \theta)/k_B T}}{1 + e^{-\epsilon(z, \theta)/k_B T}}, \quad (5.10)$$

and the corresponding affinity at the same region is then given by

$$K_{eq}(z, \theta) = \frac{n_{eq}(z, \theta)}{N_\theta - n_{eq}(z, \theta)} = e^{-\epsilon(z, \theta)/k_B T}. \quad (5.11)$$

Similarly, by defining

$$n_\theta = n_{eq}(z_s, \theta) + N_\theta^{1/2} \xi_\theta, \quad (5.12)$$

where z_s stands for the separation distance for particle being at the saddle point ², and using van Kampen's system size expansion [60] for Eq. (5.7) in the limit of all large N_θ 's, one gets

$$\begin{aligned} \partial_t p(\bar{\xi}_\theta, z, t) &= -\partial_z J_z \\ &+ \int_0^{\pi/2} \frac{\partial}{\partial \xi_\theta} k_r(z, \theta) \left\{ N_\theta^{1/2} \frac{K_{eq}(z_s, \theta) - K_{eq}(z, \theta)}{1 + K_{eq}(z_s, \theta)} + [1 + K_{eq}(z, \theta)] \xi_\theta \right\} p(\xi_\theta, z, t) d\theta \\ &+ \int_0^{\pi/2} \frac{1}{2} k_r(z, \theta) \frac{K_{eq}(z_s, \theta) + K_{eq}(z, \theta)}{1 + K_{eq}(z_s, \theta)} \frac{\partial^2}{\partial \xi_\theta^2} p(\xi_\theta, z, t) d\theta. \end{aligned} \quad (5.13)$$

²How to define and find such a saddle point is very important. From mathematical point of view, a saddle point is a critical point at which the gradient is zero and the discriminant is less than zero. Here, we use the free energy, Eq. (5.6) or Eq. (5.14) as a target function to define the saddle point. The requirement that the gradient of free energy function at saddle point is zero leads to that the particle is in chemical equilibrium. For a spherical particle under current study, simultaneous reaching to chemical equilibrium for all the binding molecules at different curved regions over the particle surface is not trivial, though theoretically possible, because the kinetic binding and dissociation processes for molecules located at more distal regions on the particle surface might be too slow to allow for such an equilibrium to be realized. More comments on this aspect are entailed in the following Discussions and Suggestions Section.

Replacement of n_θ with ξ_θ for the free energy in Eq. (5.6) leads to

$$\begin{aligned} A(\bar{\xi}_\theta, z) &= \phi(z) + \int_0^{\pi/2} \left[n_{eq}(z_s, \theta) + N_\theta^{1/2} \xi_\theta \right] \epsilon(z, \theta) d\theta \\ &+ \int_0^{\pi/2} \left[N_\theta - n_{eq}(z_s, \theta) - N_\theta^{1/2} \xi_\theta \right] k_B T \ln \left[\frac{N_\theta - n_{eq}(z_s, \theta) - N_\theta^{1/2} \xi_\theta}{N_\theta} \right] d\theta \\ &+ \int_0^{\pi/2} \left[n_{eq}(z_s, \theta) + N_\theta^{1/2} \xi_\theta \right] k_B T \ln \left[\frac{n_{eq}(z_s, \theta) + N_\theta^{1/2} \xi_\theta}{N_\theta} \right] d\theta. \end{aligned} \quad (5.14)$$

Yet again, the drift terms in $\bar{\xi}_\theta$ dimensions cannot be derived from the potential $A(\bar{\xi}_\theta, z)$ but rather from another potential, denoted as $B(\bar{\xi}_\theta, z)$, which is expressible as the line integral of drift over diffusion terms in $\bar{\xi}_\theta$ dimensions:

$$\begin{aligned} B(\bar{\xi}_\theta, z) &= \int_0^{\pi/2} \left\{ 2N_\theta^{1/2} k_B T \frac{K_{eq}(z_s, \theta) - K_{eq}(z, \theta)}{K_{eq}(z_s, \theta) + K_{eq}(z, \theta)} \xi_\theta \right. \\ &\quad \left. + k_B T \frac{[1 + K_{eq}(z_s, \theta)][1 + K_{eq}(z, \theta)]}{K_{eq}(z_s, \theta) + K_{eq}(z, \theta)} \xi_\theta^2 \right\} d\theta \\ &+ C(z), \end{aligned} \quad (5.15)$$

where $C(z)$ depends upon the separation distance z only. In view of Eqs. (5.8), (5.14) and (5.15), the above equation becomes

$$\begin{aligned} \partial_t p(\bar{\xi}_\theta, z, t) &= \frac{\partial}{\partial z} \left[\frac{D(z)}{k_B T} \frac{\partial A(\bar{\xi}_\theta, z)}{\partial z} p(\bar{\xi}_\theta, z, t) + D(z) \frac{\partial}{\partial z} p(\bar{\xi}_\theta, z, t) \right] \\ &+ \int_0^{\pi/2} \frac{\partial}{\partial \xi_\theta} \left[\frac{\eta(z, \theta)}{k_B T} \frac{\partial B(\bar{\xi}_\theta, z)}{\partial \xi_\theta} p(\xi_\theta, z, t) + \eta(z, \theta) \frac{\partial}{\partial \xi_\theta} p(\xi_\theta, z, t) \right] d\theta, \end{aligned} \quad (5.16)$$

where the effective diffusivity in $\bar{\xi}_\theta$ dimensions is:

$$\eta(z, \theta) = \frac{1}{2} k_r(z, \theta) \frac{K_{eq}(z_s, \theta) + K_{eq}(z, \theta)}{1 + K_{eq}(z_s, \theta)}. \quad (5.17)$$

5.2.2 Mean First-Passage Time Method

Now using the parameters defined in Eqs. (3.40) and (3.41), Eq. (5.16) can be made dimensionless as follows

$$\partial_\tau p(\bar{\xi}_\theta, y, \tau) = \frac{\partial}{\partial y} \left[\chi(y) \frac{\partial \alpha(\bar{\xi}_\theta, y)}{\partial y} p(\bar{\xi}_\theta, y, t) + \varepsilon \chi(y) \frac{\partial}{\partial y} p(\bar{\xi}_\theta, y, t) \right] \quad (5.18)$$

$$+ \int_0^{\pi/2} \frac{\partial}{\partial \xi_\theta} \left[\gamma_\theta \zeta(y, \theta) \frac{\partial \beta(\bar{\xi}_\theta, y)}{\partial \xi_\theta} p(\xi_\theta, y, t) + \varepsilon \gamma_\theta \zeta(y, \theta) \frac{\partial}{\partial \xi_\theta} p(\xi_\theta, y, t) \right] d\theta,$$

with

$$\alpha(\bar{\xi}_\theta, y) = \frac{A(\bar{\xi}_\theta, z)}{\Delta A}, \quad (5.19)$$

$$\beta(\bar{\xi}_\theta, y) = \frac{B(\bar{\xi}_\theta, z)}{\Delta A} \quad (5.20)$$

$$\chi(y) = \frac{D(z)}{D(z_s)}, \quad (5.21)$$

$$\zeta(y, \theta) = \frac{\eta(z, \theta)}{\eta(z_s, \theta)}, \quad (5.22)$$

$$\gamma_\theta = l^2 \frac{\eta(z_s, \theta)}{D(z_s)}, \quad (5.23)$$

and

$$\tau = \frac{t D(z_s) \Delta A}{l^2 k_B T}. \quad (5.24)$$

At low-noise high-energy-barrier limit, the extension of the mean first-passage time formalism from two-dimensional to multi-dimensional Fokker-Planck equation is readily realizable. Here, the detailed derivations for multi-dimensional case are not reiterated (please refer to the derivations for 2-D case in Chapter 3 for more information), only the final results for the dimensionless mean first-passage time, τ_p , and the deposition rate constant of the particle from fluid suspensions are shown below

$$\tau_p = \frac{\pi}{\lambda_+} \left[\frac{|\det \alpha_{ij}^S|}{\det \alpha_{ij}^A} \right]^{1/2} e^{(\alpha_S - \alpha_A)/\varepsilon}, \quad (5.25)$$

and

$$k_+ = \frac{D(z_s) \Delta A \lambda_+}{2\pi l^2 k_B T} |\det \alpha_{ij}^S|^{-1/2} e^{-(\alpha_S - \alpha_A)/\varepsilon}, \quad (5.26)$$

where λ_+ is the positive eigenvalue of drift matrix (it is not a 2×2 matrix any more, instead $(m_\theta + 1) \times (m_\theta + 1)$, where m_θ is the number of sub-populations which are grouped based on angle θ) at the saddle point

$$\left(\begin{array}{ccccc} -\frac{\partial^2 \alpha(\bar{\xi}_\theta, y)}{\partial y^2} \Big|_{\bar{\xi}_{\theta S}, y_S} & -\frac{\partial^2 \alpha(\bar{\xi}_\theta, y)}{\partial \xi_{\theta 1} \partial y} \Big|_{\bar{\xi}_{\theta i}, y_S} & -\frac{\partial^2 \alpha(\bar{\xi}_\theta, y)}{\partial \xi_{\theta 2} \partial y} \Big|_{\bar{\xi}_{\theta i}, y_S} & \dots & -\frac{\partial^2 \alpha(\bar{\xi}_\theta, y)}{\partial \xi_{\theta \pi/2} \partial y} \Big|_{\bar{\xi}_{\theta i}, y_S} \\ -\gamma_{\theta 1} \frac{\partial^2 \alpha(\bar{\xi}_\theta, y)}{\partial y \partial \xi_{\theta 1}} \Big|_{\bar{\xi}_{\theta i}, y_S} & -\gamma_{\theta 1} \frac{\partial^2 \alpha(\bar{\xi}_\theta, y)}{\partial \xi_{\theta 1}^2} \Big|_{\bar{\xi}_{\theta i}, y_S} & 0 & \dots & 0 \\ -\gamma_{\theta 2} \frac{\partial^2 \alpha(\bar{\xi}_\theta, y)}{\partial y \partial \xi_{\theta 2}} \Big|_{\bar{\xi}_{\theta i}, y_S} & 0 & -\gamma_{\theta 2} \frac{\partial^2 \alpha(\bar{\xi}_\theta, y)}{\partial \xi_{\theta 2}^2} \Big|_{\bar{\xi}_{\theta i}, y_S} & \dots & 0 \\ \vdots & \vdots & \vdots & \ddots & \vdots \\ -\gamma_{\theta \pi/2} \frac{\partial^2 \alpha(\bar{\xi}_\theta, y)}{\partial y \partial \xi_{\theta \pi/2}} \Big|_{\bar{\xi}_{\theta i}, y_S} & 0 & \dots & 0 & -\gamma_{\theta \pi/2} \frac{\partial^2 \alpha(\bar{\xi}_\theta, y)}{\partial \xi_{\theta \pi/2}^2} \Big|_{\bar{\xi}_{\theta i}, y_S} \end{array} \right)$$

$$\times \begin{pmatrix} y \\ \xi_{\theta 1} \\ \xi_{\theta 2} \\ \vdots \\ \xi_{\theta \pi/2} \end{pmatrix} = \lambda_{\pm} \begin{pmatrix} y \\ \xi_{\theta 1} \\ \xi_{\theta 2} \\ \vdots \\ \xi_{\theta \pi/2} \end{pmatrix},$$

(5.27)

and all the other quantities can be obtained from the quadratic expansions of the free energy, Eq. (5.19), at the saddle point. For clarity, α_{ij}^S , the Hessian matrix of the free energy at the saddle point where $\bar{\xi}_i = 0$, is given below

$$\alpha_{ij}^S = \left(\begin{array}{ccccc} \frac{\partial^2 \alpha(\bar{\xi}_\theta, y)}{\partial y^2} \Big|_{\bar{\xi}_{\theta S}, y_S} & \frac{\partial^2 \alpha(\bar{\xi}_\theta, y)}{\partial \xi_{\theta 1} \partial y} \Big|_{\bar{\xi}_{\theta i}, y_S} & \frac{\partial^2 \alpha(\bar{\xi}_\theta, y)}{\partial \xi_{\theta 2} \partial y} \Big|_{\bar{\xi}_{\theta i}, y_S} & \dots & \frac{\partial^2 \alpha(\bar{\xi}_\theta, y)}{\partial \xi_{\theta \pi/2} \partial y} \Big|_{\bar{\xi}_{\theta i}, y_S} \\ \frac{\partial^2 \alpha(\bar{\xi}_\theta, y)}{\partial y \partial \xi_{\theta 1}} \Big|_{\bar{\xi}_{\theta i}, y_S} & \frac{\partial^2 \alpha(\bar{\xi}_\theta, y)}{\partial \xi_{\theta 1}^2} \Big|_{\bar{\xi}_{\theta i}, y_S} & 0 & \dots & 0 \\ \frac{\partial^2 \alpha(\bar{\xi}_\theta, y)}{\partial y \partial \xi_{\theta 2}} \Big|_{\bar{\xi}_{\theta i}, y_S} & 0 & \frac{\partial^2 \alpha(\bar{\xi}_\theta, y)}{\partial \xi_{\theta 2}^2} \Big|_{\bar{\xi}_{\theta i}, y_S} & \dots & 0 \\ \vdots & \vdots & \vdots & \ddots & \vdots \\ \frac{\partial^2 \alpha(\bar{\xi}_\theta, y)}{\partial y \partial \xi_{\theta \pi/2}} \Big|_{\bar{\xi}_{\theta i}, y_S} & 0 & \dots & 0 & \frac{\partial^2 \alpha(\bar{\xi}_\theta, y)}{\partial \xi_{\theta \pi/2}^2} \Big|_{\bar{\xi}_{\theta i}, y_S} \end{array} \right), \quad (5.28)$$

with

$$\frac{\partial^2 \alpha(\bar{\xi}_\theta, y)}{\partial y^2} \Big|_{\bar{\xi}_{\theta S}, y_S} = \phi''(y) + \epsilon''(y, \theta) \int_0^{\pi/2} n_{eq}(y_s, \theta) d\theta, \quad (5.29)$$

$$\frac{\partial^2 \alpha(\bar{\xi}_\theta, y)}{\partial y \partial \xi_{\theta i}} \Big|_{\bar{\xi}_{\theta j \neq i}, y_S} = N_{\theta i}^{1/2} \epsilon'(y, \theta i), \quad (5.30)$$

and

$$\frac{\partial^2 \alpha(\bar{\xi}_{\theta i}, y)}{\partial \xi_{\theta i}^2} \Big|_{\bar{\xi}_{\theta j \neq i}, y_S} = k_B T \frac{[1 + K_{eq}(y_s, \theta i)]^2}{K_{eq}(y_s, \theta i)}. \quad (5.31)$$

5.2.3 Discussions and Suggestions

To illustrate the use of the mean first-passage time method described in the preceding sections to obtain particle deposition rate constant to a surface based on the multi-dimensional Fokker-Planck dynamics, we start with the simplest case of having only 2 groups of binding molecules on the particle surface, as shown in Figure 5.2. All the binding molecules in these two groups are identical, except that molecules in Group 1 are located at distance z whiles those in Group 2 at distance $z + h$ (here for simplicity, the angle increments for these shaded areas are neglected). The main parameters used in the calculations and the results obtained for case studies are listed in Table 5.1. The corresponding minimal energy pathways as a function of distance are plotted in Figure 5.3.

In Table 5.1 and Figure 5.3, Cases II and III each consist of two groups of binding molecules on the particle surface, whiles Case I has only one group, which is essentially same as that studied in Chapter 3. One can see that although the presence of this second group of binding molecules can influence greatly the position and depth of the primary energy minimum, it tends to lower slightly the energy barrier at the saddle point, which would increase the probability of particle attachment through

³The position for saddle point;

⁴The equilibrium energy at saddle;

⁵The deposition rate constant of particles to a surface.

Table 5.1: Main parameter values and calculation results

Symbol	Unit	Case I	Case II	Case III
N_1	–	50	50	50
N_2	–	0	40	40
h	nm	–	40	20
z_s ³	nm	109.54	109.5	109.9
a_s ⁴	$k_B T$	9.97	9.97	9.93
k_+ ⁵	nm s^{-1}	1.16×10^{-4}	9.17×10^{-7}	7.05×10^{-6}

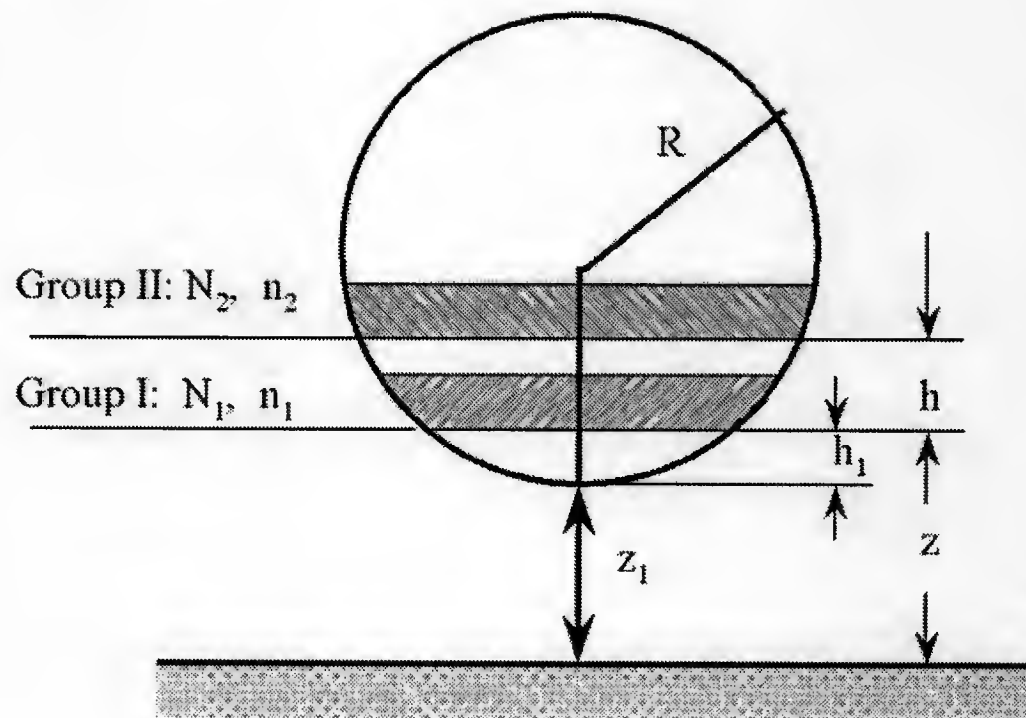


Figure 5.2: An illustration of the attachment of a spherical particle having binding molecules that could be grouped into two sub face, where the positions of binding molecules over the particle surface are described by angle θ .

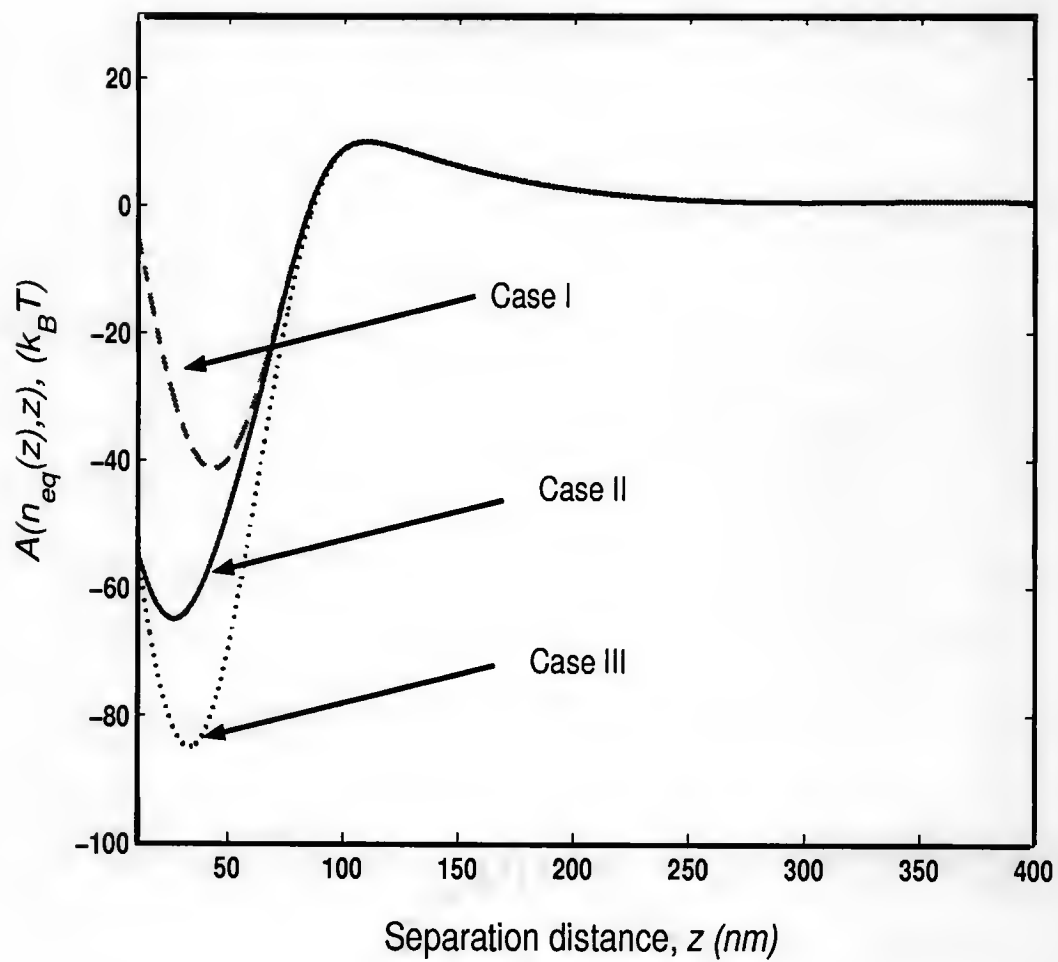


Figure 5.3: The minimal energy pathways for three case studies. The parameters used in the calculations are listed in Table 5.1.

formation of bonds by the binding molecules in Group II. However, one sees that k_+ obtained in either Case II or III is much smaller than that in Case I, which are quite contrary to what expected to happen, *i.e.*, the presence of the second group of binding molecules would enhance overall particle attachment. Apparently, something goes wrong in our MFPT approach. So, we go back to check where the problem is. As of now, the problem that has been identified is how we define the saddle position. From mathematical perspective, a saddle point is a type of critical points at which the gradient of the targeted function (here, the free energy in Eq. (5.6) or Eq. (5.14)) is zero and the discriminant of the function (*i.e.*, the determinant of the Hessian matrix of free energy, as shown in Eq. (5.28) is less than zero. One can see from Eqs. (5.28) and (5.31)), whenever a new group of binding molecules is added onto the particle surface, an additional term defined in Eq. (5.31)) will be included into the diagonal of Hessian Matrix in Eq. (5.28)). Unfortunately, this term becomes extraordinarily big because the equilibrium constant K_{eq} for more distal groups of binding molecules on the particle surface becomes so small, essentially approaches zero. In turn, that makes it impossible for the requirement that the determinant of free energy Hessian matrix must be less than zero to be satisfied. Therefore, bizarre results have been observed from our model calculations. This problem can be explained from binding kinetics as well. The requirement that the gradient of the free energy at the saddle point is zero leads to that the particle is in chemical equilibrium. For a particle with multiple groups of binding molecules over the particle surface (especially when these groups are distributed in the direction normal to the substrate, for instance, the spherical particle under study here), simultaneous reaching to chemical equilibrium for all binding molecules at different regions is not trivial, though theoretically feasible, because the kinetic binding and dissociation processes for molecules located at more distant regions from the substrate might be too slow to allow for such an equilibrium to be attained. If the bonds formed between the particle surface and the substrate

are treated as springs, the forward binding rate constant $k_f(z)$ drops exponentially with square of separation distance z , as shown in Eq. (3.85)) in Chapter 3. So, the molecules in Group I will have higher probability to bind to the substrate than all the other groups. The more further the molecules are away from the substrate, the lower the probability of bond formation will be. Thus, the requirement of all the binding molecules in these groups being at equilibrium at the same time for defining the saddle position results in a much slower overall kinetic process due to the inherent binding kinetics. This can elucidate why k_+ obtained from Cases II and III are almost 2 orders less than that from Case I in Table 5.1. It seems that the binding molecules nearest to the substrate surface play a dominant role in the contribution to the overall particle attachment. And the binding molecules in more distant positions would involve and assist in attachment, but may not necessarily be in equilibrium.

So, the question now is how to define properly the position for the saddle point?

Before attempting to answer this question, let's us first explore the possibility of some other approaches to address the problem of particle attachment with multiple groups of binding molecules over the particle surface. Since each group of these binding molecules react directly with the complementary binding cites and are independent of all the other groups, one approach is to treat these groups separately, like the way in Chapter 3. Every time when a single group of binding molecules are chosen, all the remaining groups are treated like non-existent. So, the exact method described in Chapter 3 can be used here. The final deposition rate constant k_+ (or mean first-passage time τ_p) for the whole particle could be a combination of individual values for k_+ or τ_p obtained from each single group. From this method, one can see that each individual group has different saddle point and different equilibrium energy at the saddle point. In reality, however, since the molecules in Group I are positioned always nearer to the substrate than those in Groups II III, these molecules

could always come into play to react with the substrate surface. Therefore, simple isolation of subsequent groups from their preceding groups is not very plausible.

Unfortunately as of now, finding a proper way to define the appropriate saddle transition point still remains an obstacle that prevents the attachment mechanism of particles with multiple groups of binding molecules to a surface from being elucidated. However, the potential approach to address the attachment from curved particle surface has been proposed and the problems encountered in application of such an approach were also well described, which will provide a good starting point for subsequent investigations.

5.2.4 Extension to Other Irregular Surfaces

Once the problem stated in the preceding section can be solved, the analysis described above can be readily applied to any other rough surfaces, provided that the sub-populations of the binding macromolecules are properly grouped. For example, one can always group them according to the actual distance of these binding molecules from the substrate.

CHAPTER 6 EXPERIMENTAL VALIDATIONS USING OPTICAL TRAPPING TECHNIQUE

In this chapter, an experimental method to validate our dynamic model in Chapter 3 is depicted. A three-dimensional optical trapping combined with evanescent wave scattering technique was developed and utilized to measure colloidal force-distance profiles for micron or submicron sized silica spheres to glass substrates several years back [82]. As of now, the measured force distance profiles in low electrolyte solutions are in good agreement with DLVO theory for a range of particle sizes and materials. This technique has then been modified slightly such that the direct measurement of surface forces between viable bacteria and substrata becomes possible. Colloidal as well as specific binding interactions between a single *Staphylococcus aureus* bacterium and various substrates (e.g., bare glass, β -casein coated, fibrinogen coated) were examined using this technique in Ref. [74]. Here, the same technique is employed to first measure surface forces between a biological particle, namely, streptavidin-coated bead to different surfaces including PEG-biotin surfaces, then a methodology for direct testing of our dynamic model is described.

6.1 Materials and Methods

The current experimental biomimetic system is illustrated in Figure 6.1 and it is slightly different from the applicable experimental system used in the dynamic model described in Chapter 3 (see Figure 3.1). The latter one is for the attachment of a biological particle to a surface with macromolecular linkers on the particle surface, while for the former one, the PEG-linkers that serves as spacers to mimic the real macromolecular bonds when formed, are on the substrate surface. However, the

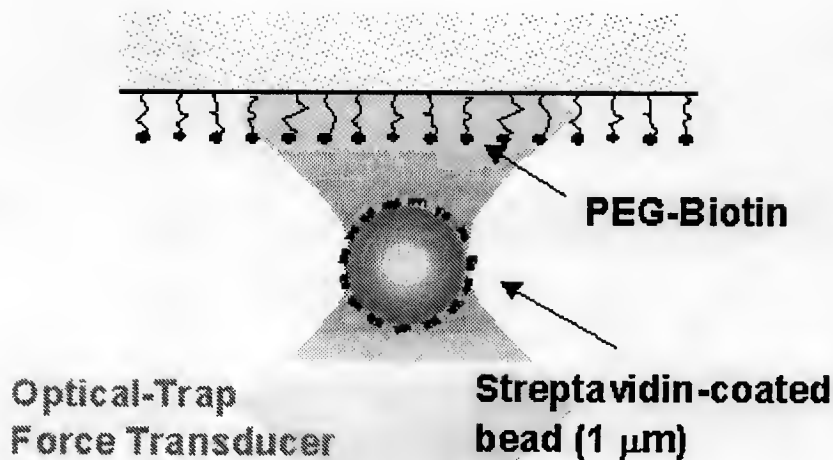


Figure 6.1: A schematic for the biomimetic system used in experiments. A streptavidin-coated bead of micron size is optically trapped and stepped towards PEG-Biotin surface. During this process, forces between the bead and the surface are measured at each position.

fundamental analyses underlying these two systems are expected to be same, though resulting surface or hydrodynamic forces that a particle experiences near such PEG-linker surfaces might be somewhat different.

The mica surfaces covered with biotinylated PEG (polyethylene glycol) linkers were obtained from Novascan (Novascan Technologies, Inc., Ames, IA). NaCl (Fisher Scientific, Pittsburgh, PA) solutions of varied concentrations were prepared using Barnstead ultra-filtered ($18.2 \text{ M}\Omega \text{ cm}$ resistivity) water. The streptavidin-coated carboxylated beads ($1 \mu\text{m} \pm 0.022 \mu\text{m}$) were purchased from Polysciences (Polysciences, Inc., Warrington, PA) and suspended in the NaCl solutions at low particle densities (about 10^5 particles/mL). A similar density of 10 or $15 \mu\text{m}$ diameter polystyrene microspheres (Polysciences, Inc.) were also prepared to serve as gap spacers between desired substrate surfaces and cover slips. All these solutions were prepared on the day of experiment to reduce contaminations. The sample solutions were each sonicated for about 20 minutes to break up particle aggregates, if any.

A small drop of the streptavidin-coated beads suspension fluid was placed in the substrate surface in which we are interested in (usually, microscope glass slides or PEG-biotin coated surfaces), and a cover slip (untreated glass surface or physisorbed polymer, like casein, surfaces) was placed over the drop and gently pressed downward until the spacer beads were in contact with both surfaces. Excess solution was removed using bibulous paper and all the edges around cover slip was then sealed with insoluble vacuum grease to prevent liquid from evaporating during the course of experiment.

6.2 Experimental Setup

A schematic diagram of the experimental setup for three-dimensional optical trap and evanescent wave light scattering is shown in Figure 6.2. A Nikon TE300 inverted microscope (Nikon Corporation, Japan) houses a single-beam gradient optical trap (Cell Robotics Laser Tweezers 100, Cell Robotics International, Albuquerque, NM) in the epifluorescence port. The optical trap uses a 100-mW diode laser beam (wavelength, 832 nm) and is formed by a Nikon 100 \times objective (plan fluor, 1.3 NA) that focuses the beam to a diffraction-limited spot within the fluid chamber. The chamber containing sample fluid prepared as above is mounted to a computer-controlled three-axis motorized stage (Ludl Electronic Products, Hawthorne, NY) that serves to control the position of single particles within the fluid chamber. The underlying cover slip of the sample chamber is optically coupled to the objective lens with index matching oil (Cargille Laboratories, Cedar Grove, NJ).

The evanescent wave is generated by directing a 17-mW He-Ne laser beam (wavelength, 632.8 nm) through a 45 °C dove prism (Melles Griot, Irvine, CA) that its lower surface is optically coupled to the substrate surface of the fluid sample chamber with index matching oil. The incident angle of the He-Ne laser beam is precisely adjusted by a rotation stage. Images for individual particle are captured by a charge-coupled device (CCD) camera and viewed on a dedicated monitor. The

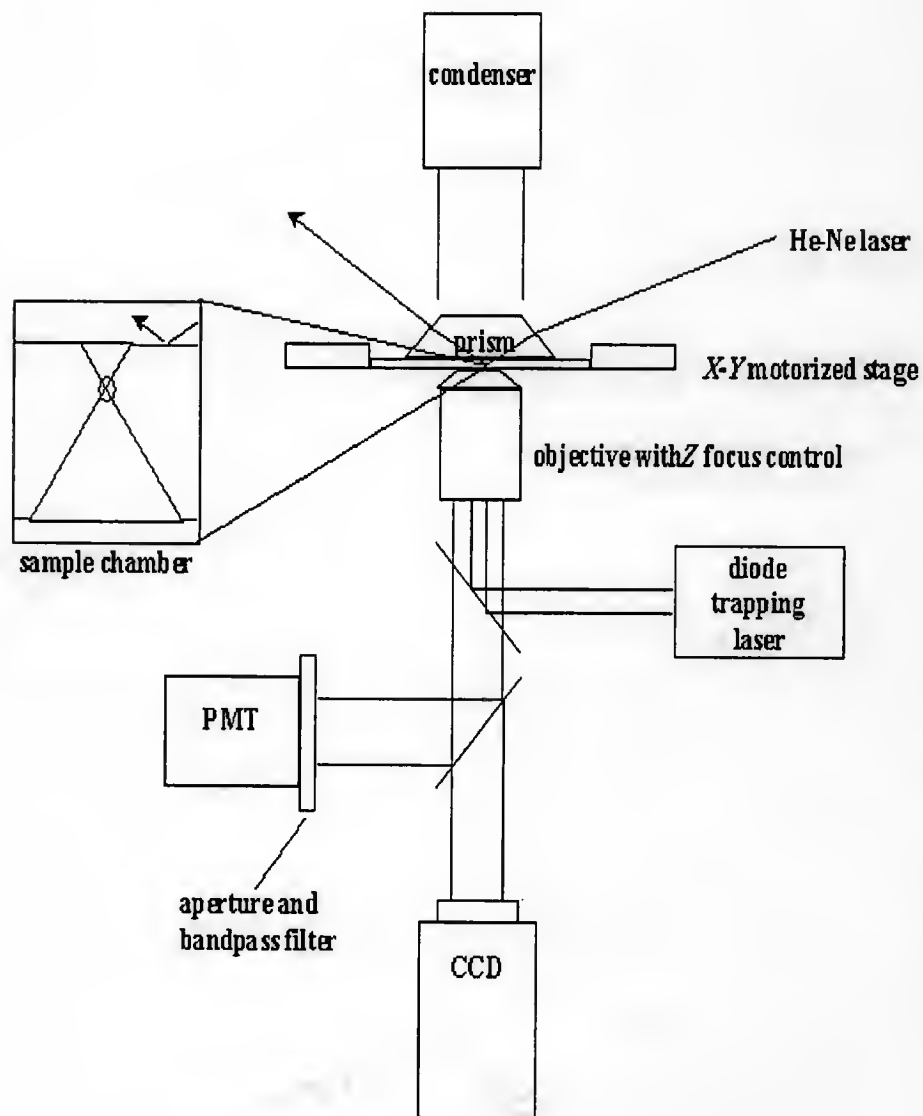


Figure 6.2: A schematic of the experimental setup [82].

scattered light by a trapped single particle near the glass slide or other substrate surface is collected by the objective lens and detected by a side-on photomultiplier tube (PMT) (Oriel Instruments, Stratford, CT). The PMT is fitted with an adjustable iris and a band-pass filter to measure the scattered light from a trapped and scattering single particle. The PMT signal is then sent to a current preamplifier where it is time averaged by an RC filter (with a time constant of 150 μ s) and then digitally sampled by a data acquisition board (National Instruments Corporation, Austin, TX). The time series intensity data are recorded to a PC file for later analysis.

With the sample chamber in place, the motorized stage (in x and y directions) is moved manually by a joystick to trap and step a streptavidin-coated bead close to the desired substrate surface so that the scattered intensity could be observed on the monitor and maximized visually by slightly adjusting the lateral position of the He-Ne laser beam. The bead is then moved away from the surface to a position where only background levels of light intensity are measurable. The trapped bead particle is stepped toward the microscope surface in adjustable increments (usually, 20 nm, could be varied by a written LabView program) during the run. The LabView program (National Instruments Corporation, Austin, TX) is used to sample PMT measured intensities at each scanning step toward the microscope surface. At each step during the scan, the program acquires 65,536 (also adjustable) intensity samples at a rate of 20 kHz (can be varied as well) and records the results to a data file. This process is repeated until the bead reaches the substrate surface as close as possible.

6.3 Data Analysis and Measurement

Two main components of this technique are: (i) a 3-D optical trap, and (ii) an evanescent wave. The optical trap acts as a force transducer that can manipulate micron or submicron sized particles with resolution of pica-Newton (pN). The relative separation distance between the particle and the surface is determined by measuring the light intensity scattered by the particle within the evanescent wave region as

it moves towards the desired substrate surface. Then the absolute particle-surface separation distance is deduced from the measured dynamic (viscous) force-distance profiles, which will be compared to the theoretical predictions by Brenner [57].

6.3.1 Evanescent Wave Light Scattering

When light is incident from an optically dense medium through a plane interface to an optically less dense medium, internal reflection occurs. Snell's law relates the angles of incidence and refraction. At a critical angle of incidence, the refracted ray generated is parallel to the interface, a phenomenon known as evanescent wave since there is no real flow of energy perpendicular to the surface. The intensity of the resulting evanescent wave decays exponentially with the normal distance from the interface. Within the evanescent wave field, a spherical particle with a refractive index dissimilar to that of the surrounding medium will scatter light with intensity also varying exponentially with distance. The scattered intensity for a spherical particle in an evanescent wave is given by

$$I(z) = I_0 \exp(-\beta z), \quad (6.1)$$

where I_0 is the scattered intensity at an arbitrary reference origin, $z = 0$; β is the decay constant or inverse penetration depth, given by

$$\beta = \frac{4\pi}{\lambda_0} [n_1^2 \sin^2 \theta_i - n_2^2]^{1/2}, \quad (6.2)$$

where λ_0 is the wavelength of light in vacuum, θ_i is the incident angle, and n_1 and n_2 are the refractive indices of the plane surface and the surrounding medium, respectively.

6.3.2 Brownian Motions of a Particle in a Potential Well

Our experimental design aims at measuring the average time taken for a biological particle escaping from a potential energy well region (or, in other words, the particle has to climb over a repulsive energy barrier) to become attached to a surface

through attractive receptor-ligand binding interactions. In the experiments, the potential well is composed of an imposed trapping potential, which is moving towards or away from the surface, and any surface potentials, which are more significant when close to the surface. Thus, the range of particle motions before attachment is limited by this potential well. The probability density of a Brownian particle being in a potential well, represented by $\phi(z)$, can be described by a Fokker-Planck equation

$$\partial_t p(z, t) = \frac{\partial}{\partial z} \left[\frac{D(z)}{k_B T} \phi'(z) p(z, t) + D(z) \partial_z p(z, t) \right], \quad (6.3)$$

which essentially is a special case of Eq. (3.9) where the specific binding interactions are absent. $\phi(z)$ here is the sum of trapping potential (and any other potentials induced by surface-independent body forces, if significant) and the potential generated by colloidal forces. As discussed in Chapter 3, one of the key assumptions underlying this equation is that low Reynolds number viscous force is proportional to particle velocity.

The stationary probability distribution here is given by

$$p_s(z) = \frac{\exp[-\phi(z)/k_B T]}{\int_{-\infty}^{\infty} \exp[-\phi(z')/k_B T] dz'}. \quad (6.4)$$

Since $p_s'(z) = -p_s(z) \phi'(z) / k_B T$, $\phi(z)$ and $p_s(z)$ share extrema with respect to z , an important property that will be used in the force measurements to find the most probable particle position within the potential well. For the case where $\phi(z)$ is approximately of parabolic shape around a position center, z_p , $p_s(z)$ has a Gaussian distribution with mean position, $\langle z \rangle = z_p$, and the variance, $\sigma_z^2 = k_B T / \phi''(z)$. Moreover, if the position-dependent diffusion coefficient $D(z)$ is approximately linear around z_p over the range of thermal fluctuations, the autocorrelation function of the particle position, $G_z(\tau)$, defined as

$$G_z(\tau) \equiv \langle [z(t + \tau) - \langle z \rangle] [z(t) - \langle z \rangle] \rangle, \quad (6.5)$$

can be approximated by

$$G_z(\tau) = \sigma_z^2 \exp(-D |\tau| / \sigma_z^2), \quad (6.6)$$

where D is the particle diffusivity at z_p . Since scattered intensities are measured instead of particle positions, autocorrelation function of intensity is related to $G_z(\tau)$ through the exponential intensity-position relationship in Eq. (6.1) as

$$G_I(\tau) \equiv \langle [I(t + \tau) - \langle I \rangle][I(t) - \langle I \rangle] \rangle / \langle I \rangle^2 \quad (6.7)$$

$$= \exp [\beta^2 G_z(\tau)] - 1, \quad (6.8)$$

where $\langle I \rangle$ is the mean intensity.

However, the actual measured intensity contains contributions from background noise and instrumentation noise, which should be corrected for accurate analysis. The background noise is subtracted from the measured signal using the mean background intensity obtained over a range of particle positions far away from the surface. The relaxation time of the fluctuations for the instrumental noise is much smaller than that of the desired intensity. Thus an RC filter ($\tau_f = 150 \mu\text{s}$) is able to remove a substantial amount of such noise. After these treatments, the resultant autocorrelation function is

$$G_f(\tau) = G_I(\tau) + \varepsilon^2 \beta^2 \sigma_z^2 e^{\beta^2 G_z(\tau)} G_z(\tau) [1 + \beta^2 G_z(\tau)] + \eta e^{-|\tau|/\tau_f}, \quad (6.9)$$

where $\varepsilon \equiv \tau_f D / \sigma_z^2$ is the ratio of RC filter time constant to relaxation time of particle fluctuations, D/σ_z^2 ; and the parameter, η , reflects the signal variance due to the instrumentation noise.

6.3.3 Calibration of Optical Trap

For axial displacements up to about a particle diameter, restoring force on the particle due to the optical trap can be described by a linear relationship

$$F_{trap}(z) = -\gamma_z(z - z_0), \quad (6.10)$$

where γ_z is the axial trap stiffness and z_0 is the position of the trap center. If no other forces are present, then $\phi(z)$ includes only the trapping potential, which is equal to

$\frac{1}{2}\gamma_z(z - z_0)^2$, thus, the stationary probability density in Eq. (6.4) is a Gaussian distribution with the mean, $\langle z \rangle = z_0$, and the variance,

$$\sigma_z^2 = \frac{k_B T}{\gamma_z}. \quad (6.11)$$

The calibration is performed by analyzing the time series intensity data at several trap positions where surface forces are negligible. At each calibration position, the measured autocorrelation functions are fitted with nonlinear least-square regressions in Eq. (6.9) using σ_z^2 , D , η as fitted parameters. The trap stiffness can be calculated using Eq. (6.11) from the average of σ_z^2 , with each sample weighted by its inverse of squared standard error. The estimate of σ_z^2 and the measured mean intensity $\langle I \rangle$ over the calibration range are used to calibrate I_0 . From the exponential intensity-distance relationship in Eq. (6.1), I is lognormally distributed with mean, $\langle I \rangle$, given by

$$\langle I \rangle = I_0 e^{-\beta z_0 + \beta^2 \sigma_z^2 / 2}. \quad (6.12)$$

Thus, I_0 can be estimated by the geometric average of $\langle I \rangle e^{\beta z_0 - \beta^2 \sigma_z^2 / 2}$ for these calibrations positions.

6.3.4 Measurement of Equilibrium and Viscous Forces

In the calibration region, surface forces are negligible due to the relatively large separation distance, in other words, only the trapping force is important there. However, as the particle approaches the surface, surface forces become significant and contribute more to the total force acting on the particle. These forces balance at the position z_p where the total potential energy is minimized and the stationary probability density of the fluctuating trapped particle is maximized, so z_p can be calculated by finding the peak in the histogram of the measured intensity at each trap position and also using

$$z_p = -\beta^{-1} \ln (I_p / I_0). \quad (6.13)$$

From the force balance equation, the surface forces are given by

$$F(z_p) = -F_{trap}(z_p) = \gamma_z (z_p - z_0). \quad (6.14)$$

To determine the dynamic viscous forces as functions of separation distances, Eq. (6.9) again is used to fit the measured autocorrelation function at each trap position. From the fitted parameter D , the drag coefficient is calculated by applying the Stokes-Einstein equation, $\delta = k_B T / D$. This requires that the potential energy well is approximately harmonic over the range of fluctuations. Knowing the drag coefficient profile, the arbitrary relative positions can be corrected to the absolute separation distance by fitting $\delta(z) = 6\pi R \eta \lambda(z)$ to the measured drag coefficient profile, where $\lambda(z)$ is the correction factor solved by Brenner for a sphere particle descending normally toward a solid surface [57].

6.3.5 Experimental Measurements and Discussions

The main goal of this chapter is to develop an experimental method for a direct test of our theoretical model described in Chapter 3. In order to accomplish this goal, many basic experiments using simple systems have to be conducted prior to using the desired biological systems. So below, we shall present all the measurement results for streptavidin-coated beads to various substrate surfaces in relatively low electrolyte solutions (<10 mM). The problems and difficulties encountered during these experiments are elucidated and some suggestions for ways out are also given; in so doing, we hope that it would be helpful for subsequent investigations of similar problems.

The force measurement data for streptavidin-coated beads to bare glass surfaces are shown here first. At low electrolyte concentrations, the repulsive electric double layer interactions acting between the negatively charged streptavidin-coated bead (-51 mV [83, 84], not measured) and glass surfaces would be significant. This repulsive potential barrier would prevent the beads from attaching to the glass surface through the beads' thermal motions only. Also, performing such force measurements

also serves the purpose of evaluating this technique for measuring surface forces at pica-Newton range between synthesized biological particles to surfaces.

First, we shall illustrate how to calibrate the optical trap and how to determine the equilibrium and viscous forces from a set of measured experimental data for a streptavidin-coated bead to a bare glass surface, as shown in Figures 6.3 – 6.4. Figure 6.3(a) describes the mean intensity $\langle I \rangle$ from an optically trapped bead in 1 mM NaCl solution as it was stepped in 20-nm increments towards a glass surface. Figure 6.3(b) shows the mean variance σ_I^2 , corresponding to the same trap positions as in Figure 6.3(a). One can see that as the trapped bead particle is stepped towards the surface, it begins to scatter light with intensity increasing exponentially until surface forces deflect the particle away from the trap center, at which position the variance reaches a peak value and afterwards starts to decline. The histogram and autocorrelation function of particle positions at two trap positions (one is at pretty far away from the surface where essentially no surface forces exist and the other one is close to the surface where surface forces are important) are shown in Figures 6.4(a) and (b), respectively. At each trap position, the equilibrium force and viscous drag coefficient are determined from the time-series of the intensity data to find the intensity mode, I_p , and also from the fitting the autocorrelation functions using Eq. (6.9) to estimate the variance, σ_z^2 and the diffusivity, D . And then the trap stiffness γ_z is determined from σ_z^2 using Eq. (6.11), and then the trap stiffness is used to get the equilibrium forces from Eq. (6.10). The viscous drag coefficient is obtained from the estimated diffusion coefficients at all trap positions using the Stokes-Einstein relationship.

The equilibrium force-distance profile data for streptavidin-coated beads to a bare glass surface (*i.e.*, in the absence of specific binding interactions) at 1.5 mM NaCl solution is plotted in Figure 6.5. And the viscous drag coefficient data as a function of particle-surface separation distances is shown in Figure 6.6. The absolute

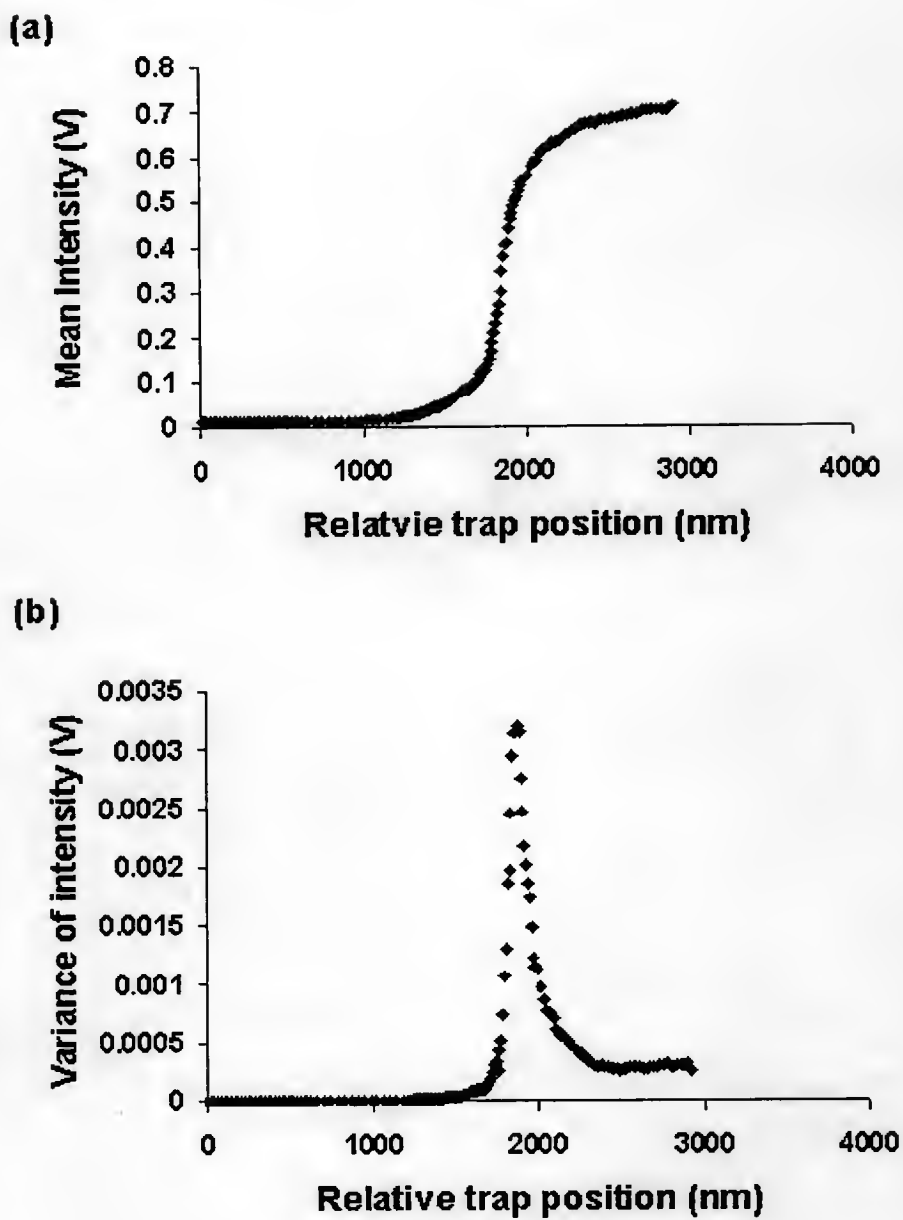


Figure 6.3: Example data for mean and variance of scattered intensity vs trap position. (a) The mean scattered intensity and (b) variance in scattered intensity are plotted vs axial trap position for a $1\mu\text{m}$ streptavidin-coated bead is stepped toward a bare glass surface in 1.5 mM NaCl solution.

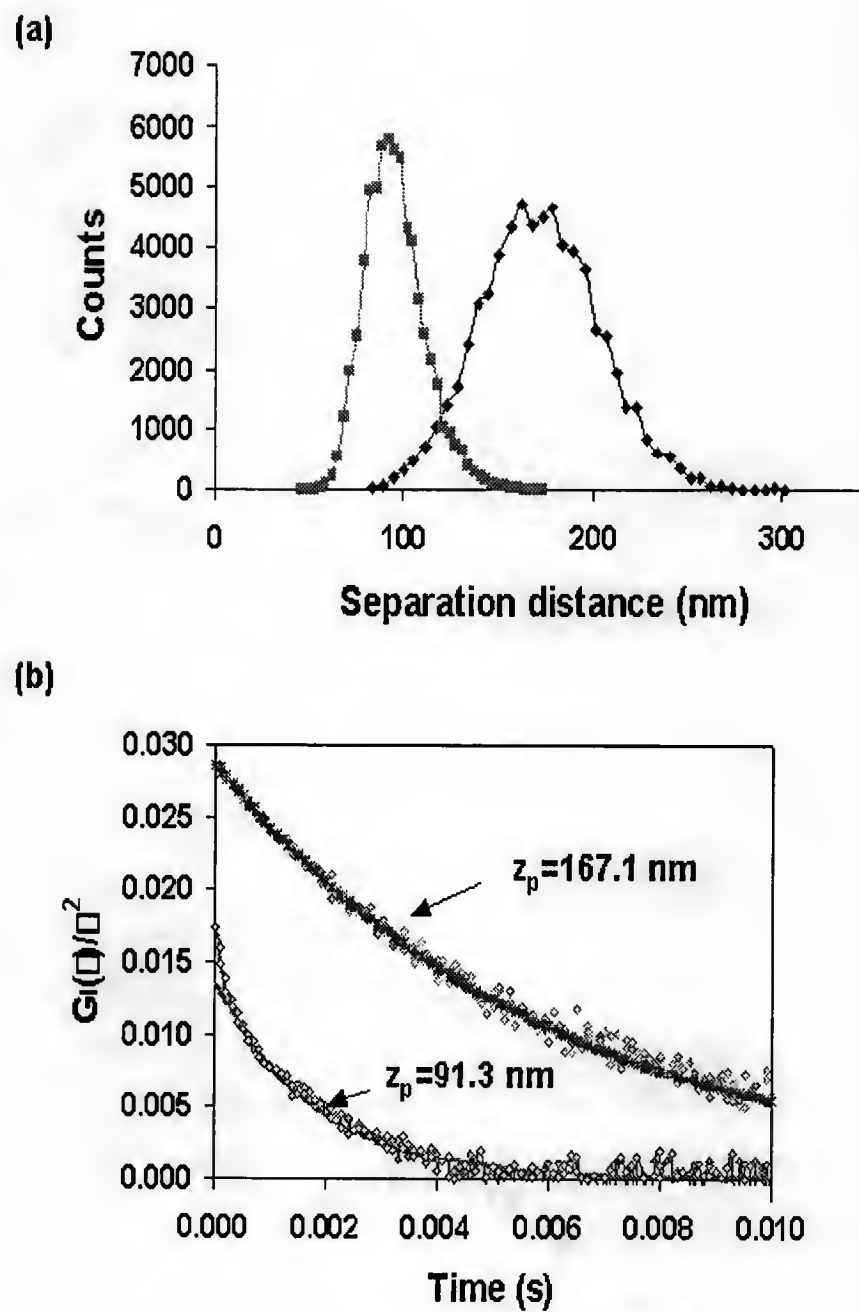


Figure 6.4: Measured histogram in (a) and autocorrelation function of particle positions in (b) at two trap positions for a $1\mu\text{m}$ streptavidin-coated bead in 1.5 mM NaCl solution.

separation distance in this plot is determined by fitting the theoretical hindered drag to the data points where the scattered intensity is small (*i.e.*, at positions relatively away from the surface). From the plot, one sees that the measured drag coefficients for particles agree very well with the theoretical predictions by Brenner [57] at larger separation distances, while deviate from Brenner's predictions at closer distances, partly due to the interactions between the two charged surfaces.

- Sample Chamber Preparation

Here we should mention that so as to measure the interaction forces between a biological particle to a bare glass surface, it suffices to use regular microscope glass slides (sizes of $75 \times 25 \times 3$ mm) (Fisher, Pittsburgh, PA) and glass cover slips (squares of 22 mm, also from Fisher). However, the PEG-Biotin mica surfaces purchased from Novascan are of 1×3 cm, so, we need to make cover slips of proper sizes for such surfaces out of either mica or glass. It is not easy to cut the glass cover slips into right size for use because of their brittleness. So we choose to cut mica surfaces. Extra care is needed here for preparation of sample chambers with PEG-Biotin surfaces. First, an extra drop of sample solutions is suggested to put onto the PEG-Biotin surfaces to prevent all the fluids from being removed from the sample chamber when using bibulous paper to withdraw the excess fluids from sample chamber gap prior to the sealing step, since the capillary forces from the bibulous paper is considerably large compared to that of liquid gap of very small size. Secondly, bare mica surfaces cannot be used to serve as cover slips. It was observed many times that no free streptavidin-coated bead particles could be found when either one of two surfaces is bare/untreated mica. Particles quickly formed doublets and then some time later they would attach to the mica surface. Mica are negatively-charged, hydrophilic surfaces, so are the streptavidin-coated bead surfaces. An electrostatic repulsive barrier would be expected between these two surfaces at close approach. However, the experiments exhibit apparently contradictive results indicating that some other attractive

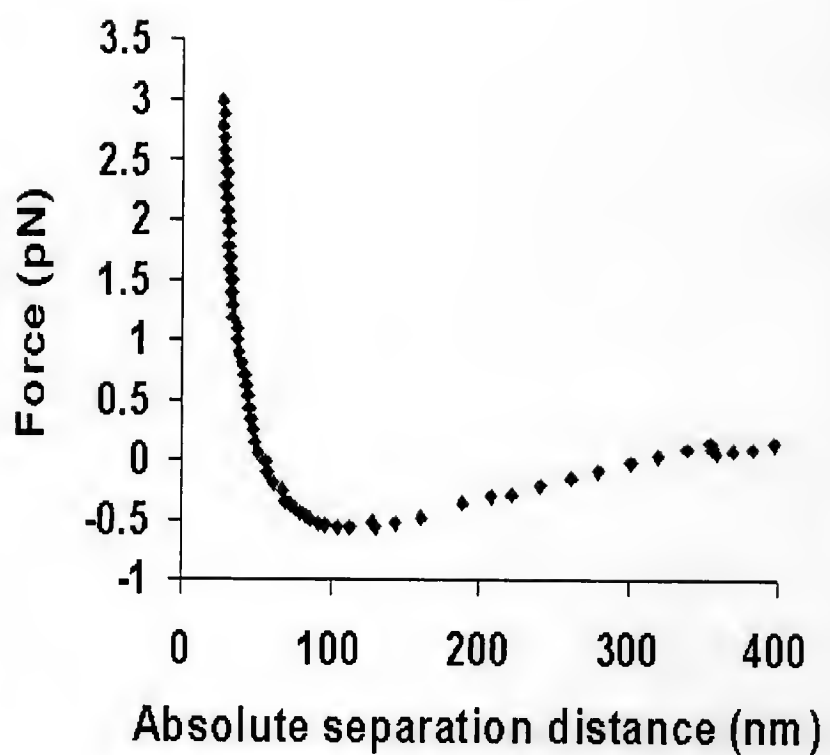


Figure 6.5: Measured equilibrium force distance profiles for a $1\mu\text{m}$ streptavidin-coated bead to bare glass surfaces in 1.5 mM NaCl solution.

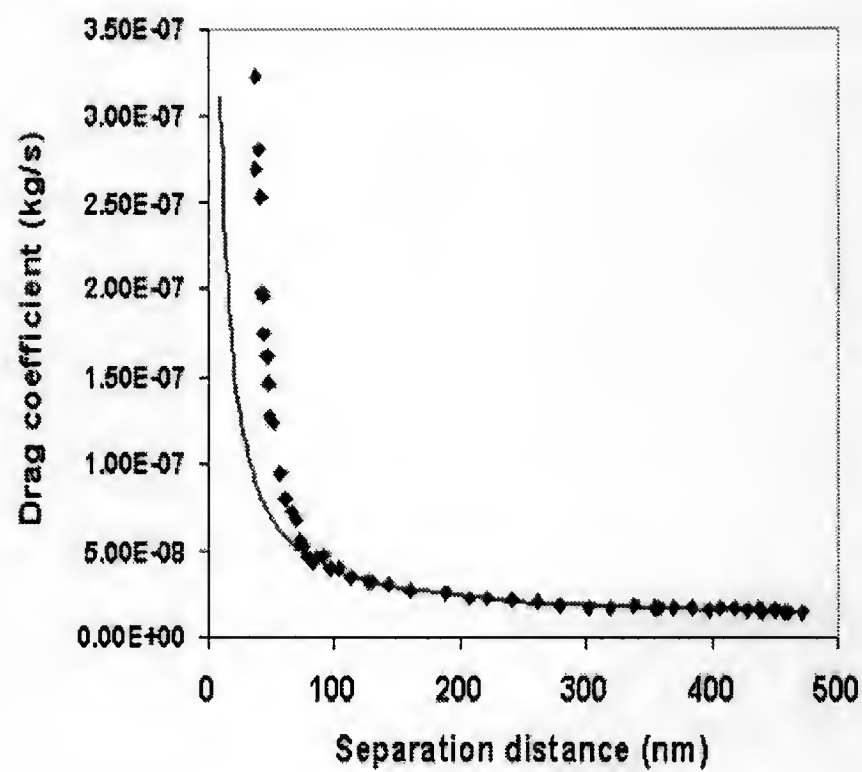


Figure 6.6: Drag coefficients are plotted as a function of separation distance. Dotted data are from experimental measurement and solid line is a fit from Brenner's theoretical prediction.

interactions might exist and can overcome the repulsive forces for bead particles to attach. The explanation for this observation is unclear yet. The interaction forces responsible for doublet formation and subsequent attachment to the bare mica surface have not been identified or characterized. This phenomenon is also observed when measuring the interaction forces between *S. aureus* bacteria and bare mica surfaces by other group members.

So, next we would like to construct a steric barrier by coating a polymer layer (such as PEG, casein, β -casein, etc.) to mica surface to prevent attachment from occurring. The protocol for physi-sorption of a casein layer on mica surface is briefly described below (for more detailed information, please see Refs. [74] and [75]). Casein (or other proteins) was suspended in Dubelco's phosphate-buffered saline (PBS) (Invitrogen Life Technologies, Rockville, MA) with 0.1 mg MgCl₂ and 0.1 mg CaCl₂ added and 0.1 μ m filtered. Casein (Sigma Pharmaceuticals, St. Louis, MO) was suspended in PBS solution at a concentration of 6.7 mg/mL or higher (due to the lower solubility of casein in PBS). The mica surfaces were coated with casein proteins by submerging them in the casein solution for two hours while these surfaces were swirled on a rotating platform (Roto Mixer) in a slide holder. These slides were stored in PBS solution and then rinsed quickly before use. The coated surfaces should not be left in the air for longer time, otherwise, proteins on the surface would desorb.

- Proposed Method for Measuring Time to Attachment

Suppose the fluid sample chamber was prepared successfully as described above such that free individual particles can be easily observed and trapped, and also there won't have problems to get these single particles to scatter light (the reason to emphasize this point is that the coated mica surfaces are very thin and will bend easily when subjected to external forces). In addition, all these experimental

steps should be conducted as quickly as possible to reduce potential attachment of streptavidin-coated beads to PEG-Biotin surface due to Brownian motions as a result of the attractive specific binding interactions between streptavidin and biotin.

The proposed idea to measure the mean time required for the trapped particle to escape from the applied trapping potential well, overcome the repulsive energy barrier caused mainly by electric double layer and steric interactions, and then attach to the surface because of the attractive binding interactions is described in brief here. The optical trap in the current set-up is relatively weak, therefore, once a particle is attached to the surface, the restoring trapping force is not able to pull the particle away from the surface. Also, it is difficult to estimate at exactly when a trapped particle would attach to the surface as it is stepped towards the surface since it undergoes constant Brownian motions within the trap. Thus, we suggest here to use different particles to carry out the experimental measurements as a coarse estimate. Every time an individual particle is trapped and moved towards the surface at certain distance away from the surface, the time taken for its attachment will be recorded. To get a reasonable average for the measured time, the same experiments will be repeated for about 10 times or more (if more free particles are available). The time needed for stepping the particle to the vicinity of the surface (in the best case, same trap position should be reached for every single measurement) is subtracted from the total time measured, which is achieved by analyzing the distance the particle has travelled and the motor velocity. Unfortunately, due to the time constraints here, I am not able to perform such experiments by myself, but hope that the subsequent investigators can get some help from my work.

CHAPTER 7 CONCLUSIONS AND RECOMMENDATIONS FOR FUTURE WORK

Conclusions

The main goal of this work has been to have a fundamental understanding of the attachment mechanisms of biological particles to a surface when mediated by both conventional colloidal forces and macromolecular binding interactions. Better understanding of such attachment mechanisms eventually can assist in many useful practical applications, for example, the design of infection-resistant biomaterials or the development of high-specificity filters capable of removing specific organisms according to their distinctive surface properties. In this work, a dynamic model has been developed to study the attachment of a rigid biological particle to a surface mediated by surface-bound adhesive macromolecules. The mean first-passage time approach has been used to compute analytically the mean transition time from the secondary energy minimum as well as the deposition rate constant from the model where neither particle diffusion nor binding are rate limiting and to evaluate the dependency of the attachment rate based on the molecular and physical properties of the binding macromolecules from the energy landscape determined by colloidal and bridging interactions.

The challenge in the study of the particle attachment in the presence of bridging macromolecules resides in the proper account for the non-equilibrium bridging forces when bond formation and dissociation occur on a time-scale comparable to the time-scale of particle diffusion near a surface. The present work addresses the above problem by approximating the discontinuity of bonds formed in the interface as a continuous fluctuating variable in the limit of large binding molecules using van Kampen

system size expansion, and then examining how long the particle takes to move from the free state to the bound state for the perturbation of lower noise. For relatively weak noise and sufficiently sharply peaked energy barrier, the pseudo-stationary probability distribution for the particle can be assumed and only the dynamic properties of the particle at the saddle point and/or at the secondary energy minimum need to be examined for obtaining the attachment rate of the particle to the surface. By examining the dynamic deterministic of the particle at the saddle, the approach predicts the rate analytically for the case where neither binding nor particle diffusion are necessarily rate-limiting factors. The results predicted from the model show that the height of the energy barrier at the saddle point, rather than the depth of the primary energy minimum, governs the transition rate of the particle to the bound state. The deposition rate constant is strongly dependent on binding parameters such as surface density, length, stiffness and kinetic rate constants of the bonds formed between the particle and the surface. The results from MFPT method are in good agreement with those from numerical solutions, but are much easier and faster to be obtained than the latter.

The dynamical model developed has been applied in the adhesion of bacterium *Staphylococcus aureus* to fibrinogen-coated surfaces by employing the actual parameter values either experimentally measured or estimated from existing reasonable models for the binding molecules studied here, namely, clumping factor-fibrinogen binding pair. In addition, an experimental methodology for a direct testing of the model is also described using three-dimensional optical trapping along with evanescent wave light scattering techniques through measurement of the attachment dynamics of streptavidin-coated beads to biotinylated PEG (polyethylene glycol) surfaces.

Recommendations for Future Work

The use of the MFPT approach in studying the attachment mechanisms of biological particles to various surfaces from the developed dynamical model is new and

already shows its advantages from this work over numerical methods commonly used in many studies. Complexity and limitations for its applicability exist, however, and some future work regarding to its further improvements as well as other explorations are recommended below.

- Studying Detachment Mechanisms

Although the approach was used here for particle attachment, it can be easily applied to spontaneous particle detachment by determining the sojourn time of the particle near the primary energy minimum, instead of the secondary minimum, provided that the energy at the secondary energy minimum is sufficiently lower than that at the saddle point. However, complexities of the bound state that would affect the depth of the energy minimum (such as particle deformation) need to be considered.

- Examining the Effect of Particle Curvature on Attachment

In Chapter 5, we have attempted to examine the effects of the curvature of a particle (for example, a spherical particle) on the attachment mechanisms. It has been done through the extension of the MFPT formulism from a two-dimensional to a multi-dimensional Fokker-Planck dynamics. Although such extension can be easily formulated and carried out by grouping the binding molecules on the curved particle surface into several different populations and then by treating each population as an independent stochastic variable to be added into existing Fokker-Planck equation, a major problem (namely, how to define appropriately the saddle point from a free energy function which involves in multiple independent variables) is encountered and remains unsolved as of now. Personally, I do not think that it is a problem inherent in this curvature problem itself and thus worth of further investigation.

The methodology of grouping binding molecules on particle into different populations is very useful and applicable to many other similar problems, for example,

the heterogeneity in binding behaviors of molecules arising from irregular shape of particle surface, multiple types of binding molecules existent on particle, and the like.

- Continuation on Direct Testing of the Model Using Optical Trapping Techniques

An experimental method has been described in Chapter 6 for a direct testing of the model predictions from the mean first-passage time approach using three-dimensional optical trapping together with evanescent wave light scattering techniques through the measurement of attachment dynamics for a streptavidin-coated particle to PEG-biotin surfaces. As one can see from that chapter, one of the major problems results from the preparation of sample chamber which consists of fluid solutions containing streptavidin-covered beads confined between the PEG-biotin surface and a proper chosen cover slip. Another major problem of using PEG-biotin surfaces in current experimental set-up has been found to be the relatively higher background intensity scattered by PEG molecules. Further investigations on this are suggested.

APPENDIX MATLAB CODES

This Appendix contains several programs written in MatLab to compute the mean first-passage time of a spherical particle escaping from a potential well to pass through a saddle transition point and then become attached.

```

***** This program computes mean first-passage time of a spherical
*** particle escaping from a potential well through saddle point to
*** attachment

global phi0 B H kT G epsilon0 z0 gamma N R zp PSTIF

phi0=90;                                % coefficient for repulsive potential, kT
B=0.02;                                  % inverse of the charged layer length,
nm^-1;                                    % H=0.2;                                % Hamaker constant

zp=200;                                   % trap position, nm
PSTIF=8.e-4;                             % trap stiffness, kT.nm2 (sigma=35 nm)

R=1000;                                  % particle radius, nm
kT=1.38e-23*298;                         % thermal energy in J=N.m
%G=4/3*pi*(R*1e-9)^3*1900/kT*1e-9;      % gravitation coefficient, kT/nm

epsilon0=-1;                             % unstrained bond energy, kT
z0=40;                                   % unstrained bond length, nm
gamma=0.002;                             % bond stiffness, kT/nm2

N=50;                                    % total available binding molecules
L=2000;                                 % boundary layer length, nm

kf0=200;                                % forward binding rate constant, s^-1
LTRAN=0.5;                               % bond transition state length, nm

eta=0.00085;                            % viscosity of water, kg/ (m.s)

dz=0.1;                                  % discretized z step size, nm
dxi=0.1;                                % discretized xi step size

z=dz:dz:(L-dz);
xi=-7.0:dxi:7.;

%%% Contour of the energy as functions of z and xi
A=zeros(length(xi),length(z));

phi=phi0*exp(-B*z)+0.5*PSTIF*(z-zp).^2;  %G*z %H*R./(6*z); % repulsion
epsilon=epsilon0+0.5*gamma*(z-z0).^2;        % bond energy
keq=exp(-epsilon)+eps;                      % keq(z)

for i=1:length(xi)
    A(i,:)=phi-N*log(1+keq)+(xi(i)^2)*((1+keq).^2./keq);
end

figure(1)
contour(z,xi,A,[-100:10:100])
axis([10 300 -7 7])

hold on

neq=N*exp(-epsilon)./(1+exp(-epsilon));

```

```

plot(z,sqrt(N)-neq/sqrt(N))
plot(z,-sqrt(N)+neq/sqrt(N))
plot(z,neq/sqrt(N))
plot(z,-neq/sqrt(N))
axis([10 300 -7 7])

hold on

[t,zx]=ode23('sepa',[0 0.5],[400 0.145493]');
plot(zx(:,1),zx(:,2))

[t,zx]=ode23('sepa',[0 0.5],[400 -0.145493]');
plot(zx(:,1),zx(:,2))

[t,zx]=ode23('sepa',[0 0.5],[112.6 -0.05]');
plot(zx(:,1),zx(:,2))

[t,zx]=ode23('sepa',[0 0.5],[112.6 0.05']);
plot(zx(:,1),zx(:,2))

hold off

%%% The minimum potential energy pathway (xi=0)
Axio=zeros(1,length(z));
Axio=phi-N*log(1+keq);
Axii=0.5*PSTIF*(z-zp).^2;
Axii=-N*log(1+keq);
Axio=phi0*exp(-B*z);
Axio=phi0*exp(-B*z)-N*log(1+keq);

figure(2)
%plot(z,Axio,'m-',z,Axii,'b:',z,Axii,'g-.',z,Axio,'k-.')
plot(z,Axio,'b-')
axis([10 400 -60 30])
%title('Figure 3')
xlabel('separation distance, \itz (nm)')
%ylabel('VitA(n_e_q(z),z), (kT)')
ylabel('Interaction energy, \it(kT)')
gtext('saddle transition')
gtext('unattached')
gtext('attached')

figure(5)
plot(z,Axio,'b-.',z,Axio,'r-')
axis([10 400 -60 30])
%title('Figure 3')
xlabel('separation distance, \itz (nm)')
%ylabel('VitA(n_e_q(z),z), (kT)')
ylabel('Interaction energy, \it(kT)')
gtext('saddle transition')
gtext('unattached')
gtext('attached')

hold on

%%% The gradient of Axio
%Axiof=zeros(1,length(z));

```

```

%AxiOf=-B*phi0*exp(-B*z)+G+H*R./ (6*z.^2)+N*gamma*exp(-epsilon).*(z-
z0)./(1+keq);

%plot(z,AxiOf)

%%% Call function 'af1' to calculate position and energy of saddle
point
%%% Be ware to change variable range if varying binding parameters
zsad=fmin('afs', 50, 140);
asad=-afs(zsad);

%%% Call function 'af' to calculate position and energy at the
secondary minimum
%%% Be ware to change the position range if varying binding parameters
zmin=fmin('afm',140, 550);
amin=afm(zmin);

deltaL=zmin-zsad;                                % length scale
deltaA=asad-amin;                                % energy barrier height

%%% scaled position variable y=z/deltaL
ys=zsad/deltaL;
ym=zmin/deltaL;

%%% non-specific interaction energy at saddle and minimum
phiys=phi0*exp(-B*zsad)+0.5*PSTIF*(zsad-zp)^2;    %G*zsad  %-
H*R./ (6*zsad);
phiym=phi0*exp(-B*zmin)+0.5*PSTIF*(zmin-zp)^2;    %G*zmin  %-
H*R./ (6*zmin);

%%% equilibrium constant at saddle and minimum
keqys=exp(-epsilon0-0.5*gamma*(zsad-z0)^2);
keqym=exp(-epsilon0-0.5*gamma*(zmin-z0)^2);

%%% secondary derivatives of phi at saddle and minimum
phidpys=phi0*(B*deltaL)^2*exp(-B*zsad)+PSTIF*deltaL^2;  %-
H*R./ (3*deltaL*(ys^3));
phidpym=phi0*(B*deltaL)^2*exp(-B*zmin)+PSTIF*deltaL^2;  %-
H*R./ (3*deltaL*(ym^3));

%%% first derivatives of Keq at saddle and minimim
keqpys=keqys*(-gamma*(ys*deltaL-z0)*deltaL);
keqpym=keqym*(-gamma*(ym*deltaL-z0)*deltaL);

%%% second derivatives of Keq at saddle and minimum
keqdpys=keqpys*(-gamma*(ys*deltaL-z0)*deltaL)-keqys*gamma*deltaL^2;
keqdpym=keqpym*(-gamma*(ym*deltaL-z0)*deltaL)-keqym*gamma*deltaL^2;

%%% dimensionless energy barrier
da=(phiys-phiym)/deltaA-N/deltaA*log((1+keqys)/(1+keqym));

%%% second particle derivatives of alpha vs xi at saddle and minimum
dpas=2/deltaA*(1+keqys)^2/keqys;
%dpam=2/deltaA*(1+keqym)^2/keqym;

%%% determinant of Hessian matrix of alpha at saddle and minimum

```

```

detas=dpas*(phidpys/deltaA-
N/deltaA*keqdpys/(1+keqys)+N/deltaA*(keqrys/(1+keqys))^2);
detam=phidpym/deltaA-
N/deltaA*keqdpym/(1+keqym)+N/deltaA*(keqpym/(1+keqym))^2;
%detam=detam1*sqrt(pi)*sqrt(keqym)/(1+keqym)*erf(sqrt(N*keqym));

%%%% forward binding rates
%logkf0=3.0:0.5:11.0;

%%%% bond dissociation rates
%krs=exp(logkf0)*exp(epsilon0)*exp(LTRAN*(zsad-z0)*gamma);
krs=kf0*exp(epsilon0)*exp(LTRAN*(zsad-z0)*gamma);

%%%% diffusion co. at saddle (call function 'lambda')
ds=kT/6/pi/(R*1e-9)/lambda(50,zsad)/eta*1e18;

%%%% effective diffusion co. in xi-direction
sgamma=deltaL^2/ds.*krs*keqys/2/(1+keqys);
lplus2=sgamma.*dpas;

%%%% dimensionless mean first-passage time
rest=pi.*(abs(detas)/detam)^0.5*exp(da*deltaA);

tauy=pi./sgamma*(abs(detas)/detam)^0.5*exp(da*deltaA)/dpas;

%%%% dimensionless mean first-passage time
tau=pi/deltaA./(krs*keqys/2/(1+keqys))*(abs(detas)/detam)^0.5*exp(da*deltaA)/dpas;

%figure(3)
%plot(logkf0,log(tau))

%figure(4)
%plot(log(sgamma),log(1/2./tauy))

lplus=phidpys/deltaA-
N/deltaA*keqdpys/(1+keqys)+N/deltaA*(keqrys/(1+keqys))^2;
tauyd=pi*(abs(detas)/detam)^0.5*exp(da*deltaA)/abs(lplus);

%tauydb=pi*(abs(detas)/detam)^0.5*exp(da*deltaA)./abs(sgamma*dpas+lplus);
%tauydb=pi*(abs(detas)/detam)^0.5*exp(da*deltaA)./abs(sgamma*dpas+lplus);

%%%%%%%%%%%%%
%%%%%%%%%%%%%

```

```
%%%%% This function will be used to calculate the primary energy minimum
function y=afm(z)

global phi0 B KT G epsilon0 z0 gamma N R zp PSTIF

phi=phi0*exp(-B*z)+0.5*PSTIF*(z-zp).^2;  %G*z  %-H*R./(6*z);
epsilon=epsilon0+0.5*gamma*(z-z0).^2;
keq=exp(-epsilon);

y=phi-N*log(1+keq);

%%%%% This function will be used to calculate the saddle point

function y=afs(z)

global phi0 B KT G epsilon0 z0 gamma N R zp PSTIF

phi=phi0*exp(-B*z)+0.5*PSTIF*(z-zp).^2;  %G*z  %-H*R./(6*z);
epsilon=epsilon0+0.5*gamma*(z-z0).^2;
keq=exp(-epsilon);

y=-phi+N*log(1+keq);
```

```

%%%%% Calculate diffusion coefficient from Brenner's prediction

function y=Dz(n,z)

R=1000;
eta=0.00085;
kT=298*1.38e-23;

%alpha=log((R+z)/R-sqrt((R+z)/R)^2-1));
alpha=acosh((R+z)/R);

sum=0.;
for i=1:n
    sum=sum+i*(i+1)/(2*i-
1)/(2*i+3)*(((2*sinh((2*i+1)*alpha)+(2*i+1)*sinh(2*alpha))...
./ (4*(sinh((i+0.5)*alpha)).^2-(2*i+1)^2*(sinh(alpha)).^2))-1);
end

y1=4/3*sinh(alpha).*sum;

y=kT/6/pi/(R*1e-9)./y1/eta*1e18;

%%%%% Calculate drag coefficient correction factor from Brenner's theory

function y=lamda(n,z)

R=1000;

%alpha=log((R+z)/R-sqrt((R+z)/R)^2-1));
alpha=acosh((R+z)/R);

sum=0.;
for i=1:n
    sum=sum+i*(i+1)/(2*i-
1)/(2*i+3)*(((2*sinh((2*i+1)*alpha)+(2*i+1)*sinh(2*alpha))...
./ (4*(sinh((i+0.5)*alpha)).^2-(2*i+1)^2*(sinh(alpha)).^2))-1);
end

y=4/3*sinh(alpha).*sum;

```

```

***** This program computes the mean first-passage time of a spherical
*** particle escaping from a potential well to the saddle point
*** using numerical methods

global phi0 B kT epsilon0 z0 gamma N R zp PSTIF kf0

phi0=90;                                % coefficient for repulsive potential, kT
B=0.02;                                  % inverse charged layer length, nm^-1
R=1000;                                  % particle radius, nm
kT=1.38e-23*298;                         % thermal energy, J=N.m
%G=4/3*pi*(R*1e-9)^3*1900/kT*1e-9;      % gravitation coefficient, kT/nm

epsilon0=-1;                             % unstrained bond energy, kT
z0=40;                                   % unstrained bond length, nm
gamma=0.002;                             % bond stiffness, kT/nm^2
N=50;                                    % total available binding molecules

zp=200;                                  % trap position, nm
PSTIF=8.e-4;                            % trap stiffness, kT/nm^2

kf0=1000;                                % forward binding rate constant, s^-1
L=2000;                                  % bond transition state length, nm
LTRAN=0.5;                               % viscosity of water, kg/(m.s)

*** Call function 'afs' to calculate position & energy of saddle point
*** Be ware to change variable range if varying binding parameters
zsad=fmin('afs', 50, 150);
asad=-afs(zsad);

*** Call function 'afm' to calculate position and energy at the
*** secondary minimum
*** Be ware to change the position range if varying binding parameters
zmin=fmin('afm',150,2000);
amin=afm(zmin);

deltaL=zmin-zsad;                         % length scale
deltaA=asad-amin;                         % energy barrier height

*** The following program uses finite difference method to solve the
*** mean time needed for the particle to move from each mesh point to
*** reach the separatrix
*** Using direct matrix method
*** Using the central difference for dT/dz

Ns=5;                                     % number of bonds at separatrix
dz=4;

dy=dz/deltaL;

dsepa=100;                                % dsepa is the position at separatrix
M= (L-dsepa) / dz+1;

```

```

for i=0:Ns
    for j=1:M
        dady(i+1,j)=phi0/deltaA*(-B*deltaL)*exp(-B*(dsepa+dz*(j-1)))...
            +PSTIF*(dsepa+dz*(j-1)-zp)/deltaA*deltaL...
            +i*gamma.* (dsepa+dz*(j-1)-z0)*deltaL/deltaA;
    end
end

b2=zeros(M*(Ns+1),1);
A2=zeros(M*(Ns+1),M*(Ns+1));

T=zeros(M*(Ns+1),1);

epsi=1/deltaA;
st=deltaL^2/deltaA/Dz(50,zsad);

for n2=1:(Ns-1)    % Coefficient matrix for interior points
    for m=2:M-1

        i=n2*M+m;

        if m<30
            A2(i,i)=-4*Dz(50,(m-1)*dz+dsepa)/Dz(50,zsad)*epsi...
                -st*2*dy^2*kfz((m-1)*dz+dsepa).* (N-n2)...
                -st*2*dy^2*krz((m-1)*dz+dsepa).*n2;
        else
            A2(i,i)=-4*Dz(50,(m-1)*dz+dsepa)/Dz(50,zsad)*epsi...
                -st*2*dy^2*krz((m-1)*dz+dsepa).*n2;
        end

        A2(i,i+1)=-dy*Dz(50,(m-1)*dz+dsepa)/Dz(50,zsad).*dady(n2+1,m)...
            +2*epsi*Dz(50,(m-1)*dz+dsepa)/Dz(50,zsad);

        A2(i,i-1)=dy*Dz(50,(m-1)*dz+dsepa)/Dz(50,zsad).*dady(n2+1,m)...
            +2*epsi*Dz(50,(m-1)*dz+dsepa)/Dz(50,zsad);

        if m<30
            A2(i,i+M)=st*2*dy^2*kfz((m-1)*dz+dsepa).* (N-n2);
        end

        A2(i,i-M)=st*2*dy^2*krz((m-1)*dz+dsepa).*n2;

    end
end

for n2=1:(Ns-1)    % right-hand side information for interior points
    for m=2:M-1

        i=n2*M+m;
        b2(i,1)=-2*dy^2;

    end
end

for i=2:M-1    % reflecting barrier at n=0, excluding two boundary
    points

```

```

if i<30
  A2(i,i)=-4*Dz(50,(i-1)*dz+dsepa)/Dz(50,zsad)*epsi...
  -st*2*dy^2*kfz((i-1)*dz+dsepa).*N;
else
  A2(i,i)=-4*Dz(50,(i-1)*dz+dsepa)/Dz(50,zsad)*epsi;
end

A2(i,i+1)=-dy*Dz(50,(i-1)*dz+dsepa)/Dz(50,zsad).*dady(1,i)...
+2*epsi*Dz(50,(i-1)*dz+dsepa)/Dz(50,zsad);

A2(i,i-1)=dy*Dz(50,(i-1)*dz+dsepa)/Dz(50,zsad).*dady(1,i)...
+2*epsi*Dz(50,(i-1)*dz+dsepa)/Dz(50,zsad);

if i<30
  A2(i,i+M)=st*2*dy^2*kfz((i-1)*dz+dsepa).*N;
end

b2(i,1)=-2*dy^2;

end

for n2=1:Ns-1  % reflecting barrier at m=L excluding two boundary
points
  i=n2*M+M;
  A2(i,i)=-4*Dz(50,(M-1)*dz+dsepa)/Dz(50,zsad)*epsi...
  -st*2*dy^2*krz((M-1)*dz+dsepa).*n2;
  A2(i,i-1)=4*Dz(50,(M-1)*dz+dsepa)/Dz(50,zsad)*epsi;
  A2(i,i-M)=st*2*dy^2*krz((M-1)*dz+dsepa).*n2;
  b2(i,1)=-2*dy^2;
end

for n2=0:Ns
  i=n2*M+1;
  A2(i,i)=1E3;
  b2(i,1)=0;
end

for i=Ns*M+2:Ns*M+M
  A2(i,i)=1E3;
  b2(i,1)=0;
end

A2(M,M)=-4*Dz(50,(M-1)*dz+dsepa)/Dz(50,zsad)*epsi;
A2(M,M-1)=4*Dz(50,(M-1)*dz+dsepa)/Dz(50,zsad)*epsi;
b2(M,1)=-2*dy^2;

% T=inv(A2)*b2;
S=sparse(A2);

```

```

T=S\b2;

sn=deltaA*Dz(50,zsad)/deltaL^2;

Ts=T/sn;

%%%%%%%%%%%%%%%
%%%%% calculate forward binding & reverse rate constants

function y=kfz(z)

global kT epsilon0 z0 gamma kf0

%kT=1.38e-23*298;      % thermal energy in J=N.m

%epsilon0=-2;           % unstrained bond energy, kT
%z0=40;                 % unstrained bond length, nm
%gamma=2.e-3;           % bond stiffness, kT/nm2

%kf0=200;               % forward binding rate constant, s-1
LTRAN=0.5;              % bond transition state length, nm

y=kf0*exp(LTRAN*gamma*(z-z0))*exp(-0.5*gamma*(z-z0).^2);

%%%%%%%%%%%%%%%
%%%%% calculate reverse binding & forward rate constants

function y=krz(z)

global kT epsilon0 z0 gamma kf0

%kT=1.38e-23*298;      % thermal energy in J=N.m

%epsilon0=-2;           % unstrained bond energy, kT
%z0=40;                 % unstrained bond length, nm
%gamma=2.e-3;           % bond stiffness, kT/nm2

%kf0=200;               % forward binding rate constant, s-1
LTRAN=0.5;              % bond transition state length, nm

y=hf0*exp(epsilon0)*exp(LTRAN*gamma*(z-z0));

```

```

%%%%% This function serves to calculate the separatrix by simulating to
%%% which energy well a particle starting from [n,z] will fall into

function zdot=bindsepa(t,z)

phi0=90;                      % coefficient for repulsive potential, kT
B=0.02;                        % inverse charged layer length, nm^-1
%H=0.2;                         % Hamaker constant
R=1000;                         % particle radius, nm
kT=1.38e-23*298;               % thermal energy, J=N.m
%G=4/3*pi*(R*1e-9)^3*1900/kT*1e-9;    % gravitation coefficient, kT/nm

epsilon0=-1;                    % unstrained bond energy, kT
z0=40;                          % unstrained bond length, nm
gamma=0.002;                    % bond stiffness, kT/nm^2
N=50;                           % total available binding molecules

zp=200;                         % trap center, nm
PSTIF=8e-4;                     % trap stiffness, kT/nm^2

L=2000;                         % boundary layer length, nm
kf0=1000;                        % forward binding rate constant, s^-1
LTRAN=0.5;                       % bond transition state length, nm
eta=0.00085;                     % viscosity of water, kg/(m.s)

zdot=zeros(2,1);

dadz=phi0*(-B*z(1))+PSTIF*(z(1)-zp)+gamma*z(2).* (z(1)-z0);
%+H*R/6./z(1).^2

ds=kT/6/pi/(R*1e-9)./lambda(50,z(1))/eta*1e18;

zdot(1)=-dadz*ds;

krz=kf0*exp(epsilon0)*exp(LTRAN*gamma*(z(1)-z0));
kfv=kf0*exp(LTRAN*gamma*(z(1)-z0))*exp(-0.5*gamma*(z(1)-z0).^2);

zdot(2)=kfv*(N-z(2))-krz*z(2);

%%%%%

```

```

%%%%% This program to compute contour plot and also separatrix which
%%%%% will call for function 'bindsepa'

%global phi0 B H R kT G epsilon0 z0 gamma N eta

phi0=90;           % coefficient for repulsive potential, kT
B=0.02;            % inverse charged layer length, nm^-1
%H=0.2;            % Hamaker constant

R=1000;            % particle radius, nm
kT=1.38e-23*298;  % thermal energy, N.m
%G=4/3*pi*(R*1e-9)^3*1900/kT*1e-9;    % gravitation coefficient, nm^-1

epsilon0=-1;        % unstrained bond energy, kT
z0=40;              % unstrained bond length, nm
gamma=2.e-3;        % bond stiffness, kT/nm^2

zp=200;             % trap center, nm
PSTIF=8e-4;         % trap stiffness, kT/nm^2

N=50;               % total available binding molecules
L=2000;              % boundary layer length, nm

eta=0.00085;

kf0=1000;           % forward binding rate constant, s-1
LTRAN=0.5;           % bond transition state length, nm

dz=0.5;             % discretized z step size, nm
dn=0.1;

z=dz:dz: (L-dz);
n=dn:dn: (N-dn);

A=zeros(length(n),length(z));

phizi=phi0*exp(-B*z)+0.5*PSTIF*(z-zp).^2;      %G*z      %H*R./(6*z);
epsilon=epsilon0+0.5*gamma*(z-z0).^2;

for i=1:length(n)
    A(i,:)=phizi+n(i)*epsilon+(N-n(i))/N+n(i)*log(n(i)/N);
end

%[fz,fn]=gradient(A,5,1);

figure(1)
contour(z,n,A,[-100:10:200])
axis([10 400 0 50])
title('Figure 1')
xlabel('Separation distance, \itz (nm)')
ylabel('Number of bonds, \itn')

%gtext('saddle')
%gtext('primary minimum')
%gtext('secondary minimum')

```

```

hold on

zee=1:1:1000;
q=1:.1:(N-1);

%plot(z0+((log((N-q)./q)-epsilon0)*2/gamma).^0.5,q,'-');

hold on

%plot(zee,(-phi0*(-B)*exp(-B*zee)-PSTIF*(zee-zp))./(gamma*(zee-z0)), '-')

%H*R./ (6*zee.^2)

%quiver(z,n,fz,fn)

%[t,z]=ode23('bindsepa',[0 0.2],[400 4]);
%plot(z(:,1),z(:,2))

%[t,z]=ode23('bindsepa',[0 0.2],[400 25]);
%plot(z(:,1),z(:,2))

%[t,z]=ode23('bindsepa',[0 0.2],[15 3]);
%plot(z(:,1),z(:,2))

[t,z]=ode23('bindsepa',[0 0.04],[2000 5]);
plot(z(:,1),z(:,2))

[t,z]=ode23('bindsepa',[0 0.04],[90 0.1]);
plot(z(:,1),z(:,2))

gtext('separatrix')
hold off

%%%%%%%%%%%%%

```

REFERENCES

- [1] Singer, J. S. (1992). Intercellular Communication and Cell-Cell Adhesion. *Science*, **255**, 1671-1677.
- [2] Dickinson, R. B., and Cooper, S. L. (1995). Analysis of Shear-Dependent Bacterial Adhesion Kinetics to Biomaterial Surfaces. *AICHE J.*, **41(9)**, 2160-2174.
- [3] Sharma, S. K., Mahendroo, P. P. (1980). Affinity Chromatography of Cells and Cell Membranes. *J. Chromatogr.*, **184**, 471-499.
- [4] Derjaguin, B. V. and Landau, L. D. (1941). Theory of the Stability of Strongly Charged Lyophobic Sols and of the Adhesion of Strongly Charged Particles in Solutions of Electrolytes, *Acta Phys. Chim. USSR*, **14**, 733-762.
- [5] Verway, E. J. W. and Overbeek, J. T. G. (1948). *Theory of Stability of Lyophobic Colloids*. Elsevier, Amsterdam.
- [6] van Oss, C. J. (1991). Interaction Forces Between Biological and other Polar Entities in Water: How Many Different Primary Forces are There? *J. Disper. Sci. Technol.*, **12(2)**, 201-219.
- [7] van Oss, C. J. (1995). Hydrophobicity of Biosurfaces—Origin, Quantitative Determination and Interaction Energies. *Colloids Surf. B*, **5**, 91-110.
- [8] Marshall, K. C., Stout, R., and Mitchell, R. (1971). Mechanism of the Initial Events in the Sorption of Marine Bacteria to Surfaces. *J. Gen. Microbiol.*, **68**, 317-348.
- [9] Costerton, J. W., Lewandowski, Z., Caldwell, D. E., Korber, D. R., and Lappin-Scott, H. M. (1995). Microbial Biofilms. *Ann. Rev. Microbiol.*, **49**, 711-745.
- [10] Ofek, I., and Doyle, R. J. (1994). *Bacterial Adhesion to Cells and Tissues*. Chapman Hall Inc., New York.
- [11] Hermansson, M. (1999). The DLVO Theory in Microbial Adhesion. *Colloids and Surfaces B: Biointerfaces*, **14**, 105-119.
- [12] Hartford, O., Francois, P., Vaudaux, P., and Foster, T. J. (1997). The Dipeptide Repeat Region of the Fibrinogen-binding Protein (Clumping Factor) is Required for Functional Expression of the Fibrinogen-binding Domain on the Staphylococcus aureus Cell Surface. *Mol. Microbiol.*, **25(6)**, 1065-1076.
- [13] Mascari, L. and Ross, J. M. (2001). Hydrodynamic Shear and Collagen Receptor Density Determine the Adhesion Capacity of *S. aureus* to Collagen. *Ann. Biomed. Eng.*, **29(11)**, 956-962.

- [14] Ruckenstein E. and Prieve, D. C. (1973). Rate of Deposition of Brownian Particles Under Action of London and Double-Layer Forces. *J. Chem. Soc. Farad. T 2*, **69** (10), 1522-1536.
- [15] Israelachvili, J. N. (1992). *Intermolecular and Surface Forces*. Academic Press, London.
- [16] Bongrand, P. and Bell, G. I. (1984). Cell-cell adhesion: Parameters and Possible Mechanisms. In *Cell Surface Dynamics: Concepts and Models*. Perelson, A. S., DeLisi, C., and Wiegel, F. W., editors. Marcel Dekker, Inc., New York.
- [17] van Oss, C. J. (2000). Nature of Specific Ligand-Receptor Bonds, in particular the Antigen-Antibody Bond. *J. Immunoassay*, **21**(2&3), 109-142.
- [18] Dickinson, R. B. (2002). Surface Behavior of Bacteria. In: Hubbard, A. (Ed.), *Encyclopedia of Surface and Colloid Sci.* Marcel Dekker, Inc., New York. pp. 4972-4981.
- [19] Jucker, B. A., Zehnder, A. J. B., and Harms, H. (1998). Quantification of Polymer Interactions in Bacterial Adhesion. *Environ. Sci. Technol.*, **32**, 2909-2915.
- [20] Bell, G. I. (1978). Models for the Specific Adhesion of Cells to Cells. *Science*, **200**, 618-627.
- [21] Lauffenburger, D. A., and Linderman, J. J. (1993). *Receptors: Models for Binding, Trafficking, and Signaling*. Oxford University Press, New York.
- [22] Dustin, M. L., Ferguson, L. M., Chan, P. Y., Springer, T. A., and Golan, D. E. (1996). Visualization of CD2 Interaction with LFA-3 and Determination of the Two-Dimensional Dissociation Constant for Adhesion Receptors in a Contact Area. *J. Cell Biol.*, **132**(3), 465-474.
- [23] Piper, J. W., Swerlick, R. A., and Zhu, C. (1998). Determining Force Dependence of Two-Dimensional Receptor-Ligand Binding Affinity by Centrifugation. *Biophys. J.*, **74**, 492-513.
- [24] Chesla, S. E., Selvaraj, P., and Zhu C. (1998). Measuring Two-Dimensional Receptor-Ligand Binding Kinetics by Micropipette. *Biophys. J.*, **75**, 1553-1572.
- [25] Bell, G. I., Dembo, M., and Bongrand, P. (1984). Cell Adhesion: Competition Between Nonspecific Repulsion and Specific Bonding. *Biophys. J.*, **45**: 1051-1064.
- [26] Dembo, M., Torney, D. C., Saxman, K. and Hammer, D. (1988). The Reaction-limited Kinetics of Membrane-to-surface Adhesion and Detachment. *Proc. R. Soc. London. B: Biol. Sci.*, **234**, 55-83.
- [27] Evans, E., and Ritchie, K. (1997). Dynamic Strength of Molecular Adhesion Bonds, *Biophys. J.*, **72**, 1541-1555.
- [28] Kramers, H. A. (1940). Brownian Motion in a Field of Force and the Diffusion Model of Chemical Reactions. *Physica (Utrecht)*, **7**, 284-304.
- [29] Alon, R., Hammer, D. A., and Springer, T. A. (1995). Lifetime of the P-selectin-carbohydrate Bond and its Response to Tensile Force in Hydrodynamic Flow. *Nature*, **374**, 539-542.

- [30] Kaplanski, G., Farnarier, C., Tissot, O., Pierres, A., Benoliel, A. M., Alessi, M. C., Kaplanski, S., and Bongrad, P. (1993). Granulocyte-endothelium Initial Adhesion. Analysis of Transient Binding Events Mediated by E-selectin in a Laminar Shear Flow. *Biophys. J.*, **64**, 1922-1933.
- [31] McQuarrie, D. A. (1963). Kinetics of small systems. I. *J. Chem. Phys.*, **38**, 433-436.
- [32] Cozens-Roberts, C., Lanffenburger, D. A., and Quinn, J. A. (1990). Receptor-Mediated Cell Attachment and Detachment Kinetics. I. Probabilistic Model and Analysis. *Biophys. J.*, **58**, 841-856.
- [33] Cozens-Roberts, C., Quinn, J. A., and Lanffenburger, D. A. (1990). Receptor-Mediated Adhesion Phenomena: Model Studies with the Radial-Flow Detachment Assay. *Biophys. J.*, **58**, 107-125.
- [34] Dembo, M. and Bell G. I. (1987). The Thermodynamics of Cell Adhesion. *Curr. Topics in Membranes and Transport*, **29**, 71-89.
- [35] Torney, D. C., Dembo, M. and Bell, G. I. (1986). The Thermodynamics of Cell Adhesion II. *Biophys. J.*, **49**, 501-507.
- [36] Hammer, D. A. and Lauffenburger, D. A. (1987). A Dynamical Model for Receptor-Mediated Cell Adhesion to Surfaces. *Biophys. J.*, **52**, 475-487.
- [37] Cozens-Roberts, C., Quinn, J. A., and Lanffenburger, D. A. (1990). Receptor-Mediated Cell Attachment and Detachment Kinetics. II. *Biophys. J.*, **58**, 841-856.
- [38] Dickinson, R. B. (1997). A Dynamic Model for the Attachment of a Brownian Particle Mediated by Discrete Macromolecular Bonds. *J. Colloid Interface Sci.*, **190**, 142-151.
- [39] Ma, H. L. and Dickinson, R. B. (2004). Kinetic Analysis of the Attachment of a Biological Particle to a Surface by Macromolecular Binding. *J. Theor. Biol.*, **226**, 237-250.
- [40] Ramalanjaona, G., Kempczinski, R. F., Rosenman, J. E., Douville, C., and Silberstein, E. B. (1986). The Effect of Fibronectin Coating on Endothelial Cell Kinetics in Polytetrafluoroethylene Grafts. *J. Vasc. Surg.*, **3**, 264-272.
- [41] Rosenman, J. E., G., Kempczinski, Pearce, W. H., and Silberstein, E. B. (1985). Kinetics of Endothelial Seeding. *J. Vasc. Surg.*, **2**, 778-784.
- [42] Evans, E., Ritchie, K., and Merkel, R. (1995). Sensitive Force Technique to Probe Molecular Adhesion and Structural Linkages at Biological Interfaces. *Biophys. J.*, **68**, 2580-2587.
- [43] Sjollema, J., Vandermei, H. C., Uyen, H. M., and Busscher, H. J. (1990). Direct Observations of Cooperative Effects in Oral Streptococcal Adhesion to Glass by Analysis of the Spatial Arrangement of Adhering Bacteria. *FEMS Microbiol. Lett.*, **69**, 263-269.
- [44] Evans, E. A. (1985). Detailed Mechanisms of Membrane-membrane Adhesion and Separation: I. Continuum of Molecular Cross-bridges. *Biophys. J.*, **48**, 175-183.

- [45] Evans, E. A. (1985). Detailed Mechanisms of Membrane-membrane Adhesion and Separation: II. Discrete Kinetically Trapped Molecular Cross-Bridges. *Biophys. J.*, **48**, 185-192.
- [46] Evans, E. A. (1988). Mechanics of Cell Deformation and Cell-Surface Adhesion. In Bongrand, P. (Ed.), *Physical Basis of Cell-Cell Adhesion*. CRC Press, Boca Raton. pp 91-123.
- [47] Kuo, S. C. and Lauffenburger, D. A. (1993). Relationship Between Receptor/Ligand Binding Affinity and Adhesion Strength. *Biophys. J.*, **65**, 2191-2200.
- [48] Rief, M., Gautel, M., Osterhelt, F., Fernandez, J. M., and Gaub, H. E. (1997). Reversible Unfolding of Individual Titin Immunoglobulin Domains by AFM. *Science*, **276**, 1109-1112.
- [49] Marshall, B. T., Long, M., Piper, J. W., Yago, T., McEver, R. P., and Zhu C. (2003). Direct Observation of Catch Bonds Involving Cell-adhesion Molecules. *Nature*, **423**, 190-193.
- [50] Simson, D. A., Ziemann, F., Strigl, M., and Merkel, R., (1998). Micropipet-based Picoforce Transducer: Indepth Analysis and Experimental Verification. *Biophys. J.*, **74**, 2080-2088.
- [51] Ashkin, A., Schutze, K., Dziedzic, J. M., Euteneuer, U., and Schliwa, M. (1990). Force Generation of Organelle Transport Measured in vivo by an Infrared Laser Trap. *Nature*, **348**, 346-348.
- [52] Evans, E., and Ritchie, K. (1997). Dynamic Strength of Molecular Adhesion Bonds. *Biophys. J.*, **72**, 1541-1555.
- [53] Evans, E. (1998). Energy Landscapes of Biomolecular Adhesion and Receptor Anchoring at Interfaces Explored with Dynamic Force Spectroscopy. *Faraday Discuss. Chem. Soc.*, **111**, 1-16.
- [54] Merkel, R., Nassoy, P., Leung, A., Ritchie, K., and Evans, E. (1999). Energy Landscapes of Receptor Ligand Bonds Exposed with Dynamic Force Spectroscopy. *Nature*, **397**, 50-53.
- [55] de Gennes, P. G. (1979). *Scaling Concepts in Polymer Physics*. Cornell University Press, Ithaca, New York.
- [56] Napper, D. H. (1977). Steric Stabilization. *J. Colloid Interface Sci.*, **58**, 390-407.
- [57] Brenner, H. (1961). The Slow Motion of a Sphere Through a Viscous Fluid Towards a Plane Surface. *Chem. Eng. Sci.*, **16**, 242-251.
- [58] Gardiner, C. W. (1983). *Handbook of Stochastic Methods for Physics, Chemistry and the Natural Sciences*. Springer-Verlag, Berlin.
- [59] Press, W. H., Teukolsky, S. A., Vetterling, W. T. and Flannery, B. P. (1992). *Numerical Recipes in Fortran: The Art of Scientific Computing*. 2nd Edition. Cambridge University Press, Cambridge.
- [60] van Kampen, N. G. (1981). *Stochastic Processes in Physics and Chemistry*. Elsevier-Holland, Oxford.

- [61] Stratonovich, R. L. (1963). *Topics in the Theory of Random Noise*. Gordon and Breach, New York.
- [62] Graham, R. (1973). *Quantum Statistics in Optics and Solid-State Physics*. Springer Tracts in Modern Physics, Vol. 66. Springer-Verlag, Berlin.
- [63] Talkner, P. (1987). Mean First Passage Time and the Lifetime of a Metastable State. *Z. Phys. B. Con. Mat.*, **68**, 201-207.
- [64] Matkowsky, B. J. and Schuss, Z. (1977). The Exit Problem for Randomly Perturbed Dynamic Systems. *SIAM J. Appl. Math.*, **33**, 365-382.
- [65] Matkowsky, B. J. and Schuss, Z. (1983). On the Lifetime of a Metastable State at Low Noise. *Phys. Lett. A*, **95**, 213-215.
- [66] Talkner, P. and Ryter, D. (1982). Lifetime of a Metastable State at Low Noise. *Phys. Lett. A*, **88**, 162-164.
- [67] Hänggi, P., Talkner, P. and Borkovec, M. (1990). Reaction-Rate Theory: Fifty Years after Kramers. *Rev. Mod. Phys.*, **62**(2), 251-341.
- [68] Langer, J. S. (1969). Statistical Theory of the Decay of Metastable States. *Ann. Phys.*, **54**, 258-273.
- [69] Müller R., Talkner, P. and Reimann, P. (1997). Rates and Mean First Passage Times. *Physica A*, **247**, 338-356.
- [70] McDevitt, D., Francois, P., Vaudaux, P., and Foster, T. J. (1994). Molecular Characterization of the Clumping Factor (Fibrinogen Receptor) of *Staphylococcus aureus*. *Mol. Microbiol.*, **11**(2), 237-248.
- [71] McDevitt, D., and Foster, T. J. (1995). Variation in the Size of the Repeat Region of the Fibrinogen Receptor (Clumping Factor) of *Staphylococcus aureus* Strains. *Microbiol.*, **141**, 937-943.
- [72] McDevitt, D., Nanavaty, T., House-Pompeo, K., Bell, E., Turner, N., McIntire, L., Foster, T. J., and Hook, M. (1997). Characterization of the Interaction Between the *Staphylococcus aureus* Clumping Factor (ClfA) and Fibrinogen. *Eur. J. Biochem.*, **247**, 416-424.
- [73] Ruta, A. R. (1998). *Quantitative Study of Mechanisms of Bacterial Adhesion to Surfaces*. University of Florida, PhD Dissertation.
- [74] Klein, J. D. (2002). *Direct Force Measurements of Specific and Non-specific Interactions Between a Single Bacterium and Substrate*. University of Florida, PhD Dissertation.
- [75] Brown, J. L. (2000). *Study of the Specific Adhesion of *Staphylococcus aureus* to Protein-coated Surfaces*. University of Florida, Master Thesis.
- [76] Hawiger, J., Timmons, S., Strong, D. D., Cottrell, B. A., Riley, M. and Doolittle, R. F. (1982). Identification of a Region of Human Fibrinogen Interacting with Staphylococcal Clumping Factor. *Biochem.*, **21**, 1407-1413.
- [77] McDevitt, D., Francois, P., Vaudaux, P., and Foster, T. J. (1995). Identification of the Ligand-binding Domain of the Surface-located Fibrinogen Receptor (Clumping Factor) of *Staphylococcus aureus*. *Mol. Microbiol.*, **16**, 895-907.

- [78] Shoup, D. and Szabo, A. (1982). Role of Diffusion in Ligand Binding to Macromolecular and Cell-Bound Receptors. *Biophys. J.*, **40**, 33-39.
- [79] Doi, M. and Edwards, S. F. (1986). *The Theory of Polymer Dynamics*. Clarendon Press, Oxford.
- [80] Wannier, G. H. (1987). *Statistical Physics*. Dover Publications, Inc., New York.
- [81] McQuarrie, D. A. (1975). *Statistical Mechanics*. Harper Row, New York.
- [82] Clapp, A. R., and Dickinson, R. B. (2001). Direct Measurement of Static and Dynamic Forces between a Colloidal Particle and a Flat Surface Using a Single-Beam Gradient Optical Trap and Evanescent Wave Light Scattering. *Langmuir*, **17**, 2182-2191.
- [83] Wong, J. Y., Kuhl, T. L., Israelachvili, J. N., Mullah, N., and Zalipsky, S. (1997). Direct Measurement of a Tethered Ligand-Receptor Interaction Potential. *Science*, **275**, 820-822.
- [84] Leckband, D. E., Schmitt, F. -J., Israelachvili, J. N., and Knoll, W. (1994). Direct Force Measurements of Specific and Nonspecific Protein Interactions. *Biochemistry-US*, **33(15)**, 4611-4624.

BIOGRAPHICAL SKETCH

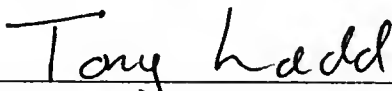
Huilian was born on July 8th, 1971, at Huixian, Henan Province, China. She completed her high school education in 1989 and then enrolled in Tsinghua University, Beijing, for her undergraduate study in the chemical engineering department. In 1994, she obtained her bachelor's degree from Tsinghua, majoring in polymer materials science. From 1994 to 1998, she worked in Concord Oil and Petrochemicals Holdings (China) Ltd., as an engineer, specializing in petroleum refining technologies. In August 1998, Huilian enrolled in the graduate program of the Department of Chemical Engineering at the University of Florida for her doctoral study, and she also completed her master's degree in December 2000.

I certify that I have read this study and that in my opinion it conforms to acceptable standards of scholarly presentation and is fully adequate, in scope and quality, as a dissertation for the degree of Doctor of Philosophy.



Richard B. Dickinson, Chairman
Associate Professor of Chemical Engineering

I certify that I have read this study and that in my opinion it conforms to acceptable standards of scholarly presentation and is fully adequate, in scope and quality, as a dissertation for the degree of Doctor of Philosophy.



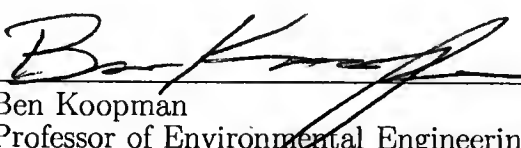
Anthony J. C. Ladd
Professor of Chemical Engineering

I certify that I have read this study and that in my opinion it conforms to acceptable standards of scholarly presentation and is fully adequate, in scope and quality, as a dissertation for the degree of Doctor of Philosophy.



Oscar D. Crisalle
Associate Professor of Chemical Engineering

I certify that I have read this study and that in my opinion it conforms to acceptable standards of scholarly presentation and is fully adequate, in scope and quality, as a dissertation for the degree of Doctor of Philosophy.



Ben Koopman
Professor of Environmental Engineering Sciences

This dissertation was submitted to the Graduate Faculty of the College of Engineering and to the Graduate School and was accepted as partial fulfillment of the requirements for the degree of Doctor of Philosophy.

August 2004

P. P. Khargonekar

P. P. Khargonekar
Dean, College of Engineering

Kenneth J. Gerhardt
Interim Dean, Graduate School

LD
1780
2004

M1115

UNIVERSITY OF FLORIDA



3 1262 08554 2644